Novel Hardware for Temperature-Jump DNP

EDWARD AXELL BREEDS, MSci

Thesis submitted to the
University of Nottingham
for the degree of
Doctor of Philosophy

March 2018

Abstract

Although NMR is a versatile technique, the low values associated with nuclear spin polarization provide inherently weak signals. A novel system to perform temperature-jump dynamic nuclear polarization (DNP) has been designed and developed at the University of Nottingham, with the aim to enhance this signal and improve the sensitivity of the NMR experiment.

This system utilizes a bespoke helium flow cryostat, located within the bore of a superconducting magnet, to achieve temperatures down to 1.75 K for high levels of polarization to build up on an electron spin population. This high level of polarization can then be transferred to a nuclear species of interest using microwave irradiation, while remaining at low temperature, allowing the weak signals associated with NMR to become enhanced.[1] Following ample nuclear polarization build-up, a powerful mid-IR laser is used to rapidly bring the sample to ∼300 K, ensuring the spectra benefit from the line narrowing associated with liquid-state NMR. An Er:YAG laser with a wavelength of 2.94 µm has been chosen for this as it couples energy directly into the vibrational modes of hydroxyl groups present within the sample.

The rapid heating mechanism underpins the success of this experiment twofold. Firstly, performing the temperature-jump in a shorter time period preserves a greater signal enhancement. This needs to be done carefully as too much heating will obliterate the sample, destroying the signal. Secondly, a temperature-jump without dilution of the sample, as occurs in dissolution DNP, allows sample recycling to take place. This opens the technique up for otherwise unavailable applications, such as multidimensional correlation spectroscopy with repetitive excitations.[2] Development of the cryo-system, heating mechanism and NMR probe, alongside preliminary experiments and calculations, suggest that this technique should greatly improve the sensitivity of the liquid state NMR experiment.

[1] A. Abragam and M. Goldman "Principles of Dynamic Nuclear Polarisation" *Rep. Prog. Phys.* **41** (1978)
[2] J. H. Ardenkjær-Larsen et al. "Increase in Signal-to-Noise Ratio of > 10,000 Times in Liquid-State NMR" *PNAS* **100** (18), (2003)

Acknowledgements

A hardware project can be a challenging undertaking, and I would like to acknowledge the following for their role in this project.

To begin, my supervisor Walter Köckenberger provided the opportunity to undertake this project, funded by the EPSRC and iMR-CDT, and continued to offer guidance throughout, whilst still nurturing independence. I would like to thank Ioan Notingher, Jonathan Cole and Kevin Pike for their ideas and support, and for lending their expertise into the optical path, cryostat and microwave aspects of the project, respectively. In particular Jonathan helped greatly with the design of the cryostat, drawing up the professional plans for the manufacturers. I am grateful to Thomas Keating Ltd. for facilitating my PhD placement and giving me a view of the industrial working environment. Particularly Richard Wylde and Kevin Pike who made sure I was welcomed to the company, involving me as fully as possible in many exciting projects. Additionally, the efforts of Georg Sebek, Trevor Walker, Michael Clack and Alan Collyer throughout the project are greatly appreciated, along with all those I worked with at that great company.

I am extremely grateful to Alan Dorkes and Sankeerth Hebbar for their patience, hard work and hands-on guidance throughout the project, and the rest of the K-team, without whom I almost certainly would not be writing this document today. Peter, Greg, Sank, Jim, Alexander, Ben, Dan, James, Adam, Jamie, Alexey and Antonio have all played, at some point and somehow, an important role in this project. I would also like to thank all of my colleagues at the SPMIC for making the work environment such a pleasant and interesting one, especially those I have had the pleasure of sharing an office with. I wish everyone I have worked alongside the very best for the future.

Finally, I would like to thank my wonderful family and friends who have supported me through everything. In particular my Mum for her encouraging words, Cleaver for his high fives, Andy for his beautiful eyes, Ben again for his beautiful ears, Rob for his reality checks and Em for her continued support, to mention a select few. There are too many wonderful people to list here, but I am truly greatful to each and every one of them.

Contents

Chapter 1

Introduction

1.1 Temperature-Jump Dynamic Nuclear Polarization

Nuclear magnetic resonance (NMR) is a powerful tool employed across various fields of physics, chemistry, biology and medicine. By carefully applying a couple of magnetic fields to precisely interact with the inherent magetic spins present within a sample (see section 2.1.1) the technique is capable of non-invasively providing information about the local molecular environments and fundamental physical properties of a specimen. Although the information that these experiments provide is invaluable, and a number of extremely successful and commonplace methods rely on the phenomenon, NMR has an inherently low sensitivity due to the small interaction between most nuclear spin species and an applied magnetic field. This has traditionally limited NMR to systems with high spin density (such as nuclear magnetic resonance imaging (MRI) of the human body) or experiments which take many averages over a long period of time.

Dynamic nuclear polarization (DNP) is a method of overcoming the low sensitivity of the NMR experiment by manipulating the spin vector of the electron, which has a far greater interaction with the applied magnetic field, and subsequently tranferring any polarization enhancement onto the nuclear spin population via the hyperfine interaction using microwaves (see section 2.1.2). An additional boost in sensitivity can be obtained by taking the spin system down to cryogenic temperatures, where the lower thermal energy allows a higher equilibrium spin polarization to be achieved. This has led to a number of experiments performing cryogenic DNP prior to a swift temperature rise (rapid-ΔT DNP), allowing for the collection of signal enhanced liquid-state NMR. While many of these experiments employ a hot solvent to bring about the rapid temperature rise, diluting the sample and denying any further experimentation, temperature-jump dynamic nuclear polarization (TJ-DNP) aims to perform the rapid temperature rise without sample dilution or destruction. This then opens the method up to a wider range of applications, such as multidimensional spectroscopy.

This thesis will begin with a brief history of NMR, noting key advances and innovations for the experimental method, and will lead into modern, state of the art DNP experiments and the various ways in which research groups around the globe are increasing NMR sensitivity. Although the fundamental theory required to understand the NMR experiment will be detailed later, in section 2.1, this will provide the context required for the specifics of the TJ-DNP experiment at Nottingham to be introduced, alongside important applications, and showcase how the project extends upon previous work. Following on from this, the chapter will end with an outline of the thesis to come.

1.2 History of Nuclear Magnetic Resonance

1.2.1 Early Magnetic Resonance

In the early 20th Century the field of physics began to use the idea of quantum theory to solve a number of problems unexplainable using classical mechanics. One such problem was that of the discrete absorption and emission spectra of atoms. Although quantum theory could address this there was still an issue of unaccountable line splitting in high resolution spectra which needed further explanation.[1] Atomic beam experiments were used to establish the existence of the electron spin and associated electon magnetic moment, with sensitive beam deflection experiments allowing Stern and Gerlach to further identify the electron magnetic moment.[2] In their famous work, now called the Stern-Gerlach experiment, a beam of collimated silver atoms discretely split in the presence of an external electromagnetic field, an observation indicating a quantized angular momentum associated with the valance electron of the silver atom. Stern was later awarded a Nobel prize for physics for this work.[3]

The nuclear magnetic resonance experiment itself was born at Columbia University during the 1930s, through the work of Rabi.[4–6] A pioneering experiment involved a beam of LiCl which was passed through a strong, constant magnetic field. The addition of a smaller oscillating field, perpendicular to the first, showed a dip in beam intensity at a particular frequency, corresponding to the Larmor frequency of the nucleus under test, and the work contributed to the presentation of the Nobel prize in physics to Rabi in 1944.[3]

1.2.2 Advances Through the Years

More sophisticated experiments followed Rabi's molecular beam work, with numerous contributions and advances steering the NMR experiment towards the many uses it has today. In 1946 the NMR absorption of a large piece of parrafin wax was predicted, observed and reported by Purcell, Torey and Pound at Harvard, demonstrating NMR in bulk material.[7] At the same time Felix Bloch was working on a set of equations to describe the time evolution of the nuclear magnetization underpinning the NMR experiment.[8] Both Bloch and Purcell shared the Nobel prize for physics for this continued work into NMR.[3] Following this, Packard and Arnold noticed the temperature dependent nature of chemical shift in an NMR spectrum due to hydrogen bonding in 1951[9] and Herman Carr began work, alongside Purcell, into measuring inherent relaxation parameters of NMR signals to provide insight into a number of different physical parameters of the samples.[10]

In 1953 Overhauser predicted that a small change in electron spin polarization would give rise to a far greater change in nuclear spin polarization,[11] later coined the Overhauser effect. This was met with a great deal of criticism from renowned physicists of the time[12] but was confirmed by Carver and Slichter later that year by observing an enhancement of the nuclear magnetic resonance signal in metallic lithium produced by the electron spin population.[13] This discovery is particularly notable as it may be considered to mark the birth of DNP. The first ^{13}C spectra were collected in 1957 independently by both Lauterbur[14] and Holm,[15] with results that displayed appreciable signal-to-noise despite the low natural abundance of the isotope. Commercially available NMR spectrometers became available in the early 60s through Varian.[1]

In the 1970s Raymond Damadian noticed that the proton NMR signals received from healthy and cancerous tissue differed and designed a system allowing him to investigate this in patients.[16,17] Meanwhile, Lauterbur at the State University of New York produced the first 2D NMR image of a test tube[18] and Richard Ernst proposed Fourier transform techniques for the acquisition of MR images.[19] Damadian completed his imaging system in the late 70s with the help of Goldsmith and Minkoff and the first images of tumors in animals[20] and MRI scans of the human body were achieved,[16] albeit with slow acquisition times. Peter Mansfield was able to develop the theoretical framework of this method and developed echo-planar imaging at the University of Nottingham,[21,22] allowing images to be produced in seconds and forming the basis of rapid MR imaging.

NMR has since become an incredibly important tool in the fields of physics, chemistry and medicine. The dependence on the chemical shift and nuclear magnetic resonance on the local environment of the spins has allowed advanced experiments to be designed so as to investigate their molecular surroundings, providing structural information and physical properties of the system.[23] The technique may commonly be used for chemical analysis of unknown samples, to follow reactions and to track specific molecules during interesting chemical dynamics. Magnetic resonance imaging has also been developed to play an invaluable role in the clinical environment as a diagnostic tool, with the contrast between healthy and diseased tissue providing a non-invasive method to investigate the human body.[24] Advances are constantly being made, reducing the time taken to create an image, improving contrast between tissues of interest and reducing scanning artefacts.[25]

1.3 Modern Experiments

1.3.1 Limits of Conventional NMR

Although NMR is successfully used to realize the techniques highlighted at the end of 1.2.2, this is largely possible because the systems are well suited to the needs of NMR, or because scientists are willing to expend long periods of time studying other, less suitable systems. For example, MRI is only such a capable diagnostic tool because the proton spin density of the human body is sufficiently high.[26] If the system under test were to have a far lower spin density, then far larger periods of time would be required, averaging the signals received, to increase the strength of the useful information in the spectrum in comparison to any randomly generated background noise.[27] One of the key areas of active research in the field of NMR is to boost this inherently low sensitivity, brought about by the weak interaction of the nuclear spin with an applied magnetic field.[28]

1.3.2 Increasing Sensitivity

The sensitivity of an NMR experiment is described using the ratio between the amplitude of the NMR peaks (P_{signal}) to that of the background noise of the system (P_{noise}). This is called the signal-to-noise ratio (SNR), and is defined in equation 1.3.2.1.

$$\text{SNR} = \frac{P_{\text{signal}}}{P_{\text{noise}}} \tag{1.3.2.1}$$

This expression indicates that, in order to increase the SNR, either the random background noise needs to be reduced or the absolute signal intensity of the true NMR signal needs to be increased.

Performing an experiment in liquid-state as opposed to solid state will increase the sensitivity and subsequent resolution of the NMR experiment, as the rapid molecular motion present in a liquid will average dipole-dipole interactions, narrowing the spin resonances. This effect can be achieved in a solid-state sample by performing Magic Angle Spinning (MAS), by which samples are spun about an axis at an angle of $\theta_{\mathrm{m}} \approx 54.74^{\circ}$ to an applied static field at kHz frequencies. This averages the strong chemical shift anisotropies and dipole couplings associated with the solid-state sample and dramatically increases the resolution of the experiment. Repeated measurements will also increase the effective sensitivity of the experiment, as the NMR signal is proportional to the number of repeated acquisitions, n, while the random noise will scale with $\sqrt{n}$. However, this method of increasing the SNR is only useful to a point, as these scaling factors dictate that an experiment with x times the SNR of a previous experiment requires x^2 scans. These long time scale experiments forbid certain dynamic processes to be investigated using NMR. Better coil design and electronic decoupling will decrease the noise picked up by the system, and this will be achieved in the project by producing low thermal noise coils (this is mentioned in section 5.1.3), but the TJ-DNP experiment primarily focusses on enhancement of the true NMR signal.

The strength of the signal induced in the coil, P_{signal}, after an NMR excitation is directly proportional to the equilibrium magnetization, M_0, of the sample (which in this case describes the density of the induced alignment of nuclear spin magnetic moments within the sample).

$$P_{\mathrm{signal}} = \alpha M_0 \tag{1.3.2.2}$$

The proportionality factor present in equation 1.3.2.2, α, is dependent on the coil volume, temperature and filling factor, as well as the quality and resonant frequency of the detection circuit [29] (section 5.1.3). This project will assume the parameters affecting α to be fixed by pre-existing experimental conditions (such as the size of the sample) and the majority of any enhancement to P_{signal} will be obtained using the magnetization term shown in equation 1.3.2.3.

$$M_0 = \frac{1}{2} N_{\text{S}} \gamma_{\text{n}} \hbar P. \tag{1.3.2.3}$$

In this expression, N_{S} is the number of contributing resonant spins, γ_{n} is the gyromagnetic ratio of the nuclear spins under test and P is the polarization, a value describing the degree to which spins are aligned which is fully derived in section 2.1.1, but introduced at face value now for the introduction of DNP.

$$\text{Polarization, } P = \tanh\left(\frac{\hbar \gamma B_0}{2kT}\right) \tag{1.3.2.4}$$

Although N_{S} and γ_{n} terms in equation 1.3.2.3 also remain fixed or small for this project (i.e lower spin density proton or carbon-13 ensembles), it can be noted that a number of other variables in equation 1.3.2.4 may be experimentally manipulated. These are namely the gyromagnetic ratio of the spins upon which polarization is built, γ (which does not have to be equal to γ_{n}), the externally applied magnetic field, B_0, and the spin-system temperature, T. By carefully designing an experiment to take advantage of these variables, spin polarization may be artificially increased above the usual Boltzmann level, resulting in subsequently higher NMR signals.

1.3.3 Hyperpolarization Techniques

A number of research groups around the world are looking at various methods to increase the sensitivity of the NMR experiment by artificially increasing polarization. These often employ application specific techniques to boost the signal where pre-existing experimental conditions forbid other pathways to artificial enhancement. For comparison with the TJ-DNP method proposed in this document, a number of hyperpolarization methods will be briefly introduced in this section. This will be far from an exhaustive list, avoiding optical pumping techniques[30] and methods using chemical exchange (such as CIDNP[31] and PHIP[32,33]) where the mechanisms are restricted to a small group of molecules that require particular starting conditions.

Utilizing the field and temperature dependences in equation 2.1.1.7 can give a substantial increase in polarization, with methods taking samples down to the milliKelvin regime in high magnetic fields known as brute force experiments. Although this method is capable of providing signals ∼1000 times greater than those attainable under standard conditions,[34] they experience extremely long polarization build up times, as nuclear spin relaxation becomes inhibited when molecular motion decreases at low temperature. While some experimentalists envision this long relaxation time providing transportable and pure, clinically applicable samples with high levels of polarization,[35,36] others are working on mediation of spin relaxation effects to drastically reduce polarization build up time.[34,37,38] Cross-polarization techniques, in which spin species are used as polarization intermediaries, and low-field thermal mixing have been shown to decrease this build-up time, using proton reservoirs and high surface area substrates to encourage this.[37,38] Furthermore, it has

recently been shown that doping the sample with certain nanoparticles increases relaxation at such low temperatures, bringing the polarization build up times for ^{13}C experiments from over a year to only a few tens of hours.[34]

Dynamic nuclear polarization is a method of artificially increasing the polarization of a nuclear species above Boltzmann polarization using the electron spin. This method is not restricted in its application or to any particular class of molecules, provided the nuclei of interest are in the vicinity of free electron spins, which can be introduced using a free radical. The far higher Boltzmann polarization of the electron spin (see figure 2.3) can be transferred to the nuclear species of interest using microwave irradiation (section 2.1.2) and an enhanced NMR spectrum can be realized.

1.3.4 Quantifying Enhancement

Transferring the Boltzmann polarization from the electron spin ensemble to the nuclei of interest, with gyromagnetic ratio values of γ_e and γ_n respectively, results in the nuclear spin polarization being dramatically increased and enhances the signal, compared to that without DNP, by a factor ε_{DNP}.[39]

$$\varepsilon_{DNP} = \frac{\gamma_e}{\gamma_n} \tag{1.3.4.1}$$

This suggests that performing this transfer will yield enhancements in the nuclear spin polarization of up to ~660 times. However, as shown in equation 1.3.2.4, this effect can be further enhanced by a number of experimental factors, such as the relative temperatures and magnetic fields at which polarization and NMR acquisition take place. In this

case, the total enhancement $\varepsilon^{\dagger}$ is updated using equation 1.3.4.2, where T_x and B_x represent the temperature or field strength at which either polarization ($x = \text{DNP}$) or NMR acquisition ($x = \text{NMR}$) take place.[40]

$$\varepsilon^{\dagger} = \varepsilon_{\text{DNP}} \left(\frac{T_{\text{NMR}}}{T_{\text{DNP}}} \right) \left(\frac{B_{\text{DNP}}}{B_{\text{NMR}}} \right) \tag{1.3.4.2}$$

These additional factors suggests that a change in temperature from polarization at 1 K to NMR acquisition at 300 K, whilst keeping the field static, introduces a further enhancement of 300. Combining this with the maximum enhancement of ε_{DNP} provides an overall maximum theoretical boost in signal of $\varepsilon^{\dagger} \approx 200{,}000$. A swathe of modern experiments, henceforth called rapid-ΔT DNP experiments, focus on DNP at low temperature followed by a rapid temperature rise and NMR acquisition to benefit from the enhancements available through equation 1.3.4.2. These also benefit from the increase in resolution associated with the liquid-state NMR experiment. It should be noted than an additional method of reporting enhancement is as a percentage of unity polarization. For example, an experiment can report a liquid-state polarization of 20% on ^{13}C which, when compared to polarization under normal conditions (see section 2.1.1), translates to an enhancement of about 250,000. This stated, care must be taken when translating these results to a realistic experimental enhancement, as many of these reports are taken at the point of polarization and are not readily accessable.

Despite dramatic enhancement, a couple of factors contribute negatively to the maximum obtainable enhancement using rapid-ΔT DNP. To begin, although capable of enhancing the absolute NMR signal intensity, these experiments require significant quantities of time to prepare

and condition the sample. This period of time could otherwise be used for signal averaging, suggesting a point at which a shorter experiment with a lower absolute NMR signal intensity would be favourable to a longer one with a slightly higher signal. As an example, if one of these experiments took 2.5 hours to cool, polarize and then heat a sample, the enhancement would have to be greater than that expected if that sensitivity was increased via repeated measurements and signal averaging for the same period of time (an enhancement that would equate to $\sim$100 times). Furthermore, while $\varepsilon_{\mathrm{DNP}}$ can simply be measured by performing an identical experiment with microwave irradiation both turned on and off, enhancement levels of the rapid-ΔT DNP experiment can only sensibly be measured after a significant fraction of $\varepsilon^{\dagger}$ has degraded via relaxation during the rapid heating stage itself and the sample reaches the point of NMR acquisition. This factor is made even more crucial by the fact that relaxation sweeps through a maximum rate during the temperature rise (see section 2.1.1 and figure 2.5). As a result, although a set of experimental conditions may predict that a maximum enhancement $\varepsilon^{\dagger} \approx 200{,}000$ is theoretically possible, this will never be measured in practice.

1.3.5 Rapid-ΔT DNP

Although the two-fold enhancement in signal strength provided by the rapid-ΔT DNP experiment is impressive, performing the rapid temperature rise on its own, let alone whilst satifying all other criteria required for DNP, is challenging. Early experiments were born from an attempt to enhance MRI using Overhauser effects.[41] While these experiments allowed *in vivo* imaging of tumor oxygenation, limitations in field strength and radical dosage led to *ex vivo* work in which the proton spin polariza-

tion of water was enhanced with the aim to create injectable, biologically compatible contrast agents. Although opening the door for many exciting experiments, the enhancements achieved through the Overhauser effect were small. The idea to polarize molecules of interest at low temperature, prior to a rapid rise in temperature, change of phase and the creation of a liquid-state sample at room temperature was conceived just before the turn of the millennium and, after over half a decade of instrumentation work, provided promising results to the NMR community in the form of the dissolution DNP experiment and the report of an enhancement in SNR of greater than 10,000.[42]

Dissolution Experiments

One of the simplest ways to bring a low temperature sample to ambient temperature in a short period of time is to inject a hot solvent into the sample space, a method known as dissolution. This provides a high thermal capacity and well contacting heat source that dissolves the sample in an efficient manner independent of the polarization temperature. Despite the success of the technique to bring about a temperature rise and report consistantly significant enhancements $\varepsilon^{\dagger}$ of the order of 10^4,[43,44] the introduction of the hot solvent dilutes the sample, both reducing the polarization concentration of a dissolution DNP experiment and rendering repeat experiments impossible. This makes dissolution DNP a single-shot experiment. A large number of groups around the world are advancing this experiment, improving hardware[45–47] and developing methods to best utilize the transient signal with multi-coil probes and complex flow paths.[48] The dissolution DNP experiment is also being combined with single-scan 2D correlation spectroscopy[49] in experiments reported to collect enhanced 2D spectra in $\sim$0.1 s.[40]

The highly polarized solution is particulary useful in the field of medicine, allowing detection of molecules that would otherwise be too weak on the NMR spectrum. MRI compatible samples have been synthesized for use *in vivo*,[50,51] and work into the extraction of potentially undesirable radicals has been carried out to ensure samples are clinic safe.[52] Highly polarized molecules may then be used to observe low concentration metabolic reactions and identify diseased tissue through spectroscopy.[53] A particularly powerful example of this is based on the different metabolization of [1-^{13}C] pyruvate by tumors and healthy tissue.[54] This drove development of portable clinical polarizers[55,56] and methods to utilize the hyperpolarized samples *in vivo*.[57] A number of metabolic pathways are now being highlighted using hyperpolarized metabolic precursors[58] and liquid-state polarizations as high as 60% are being reported using polarizers built for clinical applications.[59] Recent in-human trials have been used to investigate prostate cancer using these methods[60] with many other *in vivo* preclinical studies ongoing.[51]

A Temperature Jump Without Dilution

It is also possible, although considerably more challenging, to drive the same rise in temperature from polarization to liquid-state NMR using methods that do not dilute the sample. These temperature increases are employed such that the sample is left in the original state that it was in prior to cooling, and form the basis of a so called temperature-jump DNP (TJ-DNP) experiment. Both this method and dissolution DNP have a lot in common, with experiments relying on low temperature polarization of electron spins and microwave driven spin transfer before the system is brought to ambient temperature for enhanced liquid-state NMR. While research is ongoing to maximise the information gathered

from dilute, single-shot dissolution DNP experiments, TJ-DNP circumvents these issues via preservation of the sample under test, opening the door for repeat experiments *in situ* and more sophisticated NMR techniques.

A number of research groups have begun developing the TJ-DNP method using various heating mechanisms and experimental configurations to achieve an enhanced liquid-state NMR experiment. Initial experiments at MIT exploited advances in gyrotron technology to show that experiments could be performed to obtain reasonable enhancements ($\varepsilon^{\dagger}$ for ^{13}C between 120 for glucose and 400 for urea) and allowed sample recycling.[39] These particular experiments polarized the sample in a magnetic field of 5 T at 90 K, reporting a solid-state enhancement $\varepsilon_{\mathrm{DNP}}$ of $\sim$ 290 on ^{1}H before cross-polarization and a pulse of mid-IR CO_2 laser radiation to bring the sample to ambient temperature. This cross polarization stage was to build up polarization efficiently, avoiding the slower spin diffusion experienced during direct ^{13}C polarization. The timescales associated with these early experiments meant that the experiment could be cycled every 60-90 seconds. This has since been shown to allow signal enhanced ($\varepsilon^{\dagger}$ of $\sim$100) liquid-state multidimensional correlation spectroscopy to be performed.[61] These impressive experiments form the basis of the TJ-DNP experiment at Nottingham. Further experiments have investigated the effect of using microwave radiation and dielectric heating using a switchable microwave source[62,63] that have been reported to enhance the signal associated with ^{13}C by a factor $\varepsilon^{\dagger} \approx 550$. This experiment benefits from the fact that the microwave heating mechanism does not require additional hardware close to the sample, but they build up polarization directly on ^{13}C at 20 K, making them considerably

longer (∼3 hours). This stated, it was noted that future experiments could use ^{1}H mediation for a faster experiment. Alternative modern experiments use hot gas to bring about a considerable temperature rise in small samples[64–66] on the order of 500 ms. This microfluidic volume, although theoretically reducing the obtainable NMR signal compared to an experiment with a larger sample, then allows total recycling times to be extremely short (on the order of a few seconds), with initial enhancements $\varepsilon^{\dagger} \approx 100$ being reported with the capability of *in situ* recycling. This reduction in recycling time can then compensate for the decrease in sensitivity caused by the small sample size.

1.4 Target Applications

TJ-DNP is capable of substantial enhancements in sensitivity in liquid-state NMR of small molecules, providing they can withstand the rapid freezing and thawing processes. The ability to generate enhanced liquid-state NMR with the possibility of *in situ* sample recycling lends itself to a number of experiments, inculding multidimensional correlation spectroscopy[23] (nD COSY) which will be the main aim of the experiment. These experiments explore the magnetization transfer between nuclei of the same type (homonuclear correlation) or between different nuclear species (heteronuclear correlation) to evaluate spin coupling, and thus molecular dimensions and dynamics. While 2D COSY relies on scalar coupling between spins to highlight neighbours bonded to each other,[23] 2D NOESY (nuclear Overhauser effect correlation spectroscopy) uses the intensity of the nuclear Overhauser effect (NOE), which drops off with $1/r^6$ (where r is the distance between spins), to highlight neighbours in close proximity that are not necessarily connected through bonds.[67] This

makes the latter technique particularly useful for determining the structure of large molecules such as proteins. Performing these experiments with greater sensitivity allows multidimensional scans with greater SNR to be realized, increasing spectral resolution, and for this reason they have already been met with interest from the DNP community.

Notable examples of work in which multidimensional spectrocopy has been married with DNP include MAS solid-state DNP studies in which static temperature enhancements $\varepsilon_{\mathrm{DNP}}$ of up to 23 have been reported,[68] allowing concrete elucidation of protein dynamics and structure[69] and high-importance studies into biologically relevant areas such as the causes of Alzheimer's disease.[69] Despite the impressive nature of these studies and the commercial availability of MAS-DNP instruments from 400 MHz to 1 GHz, the technique is suited to solid-state samples and, although liquid-state MAS proton NMR has been performed more recently,[70] the experiment at Nottingham could target liquid-state applications involving other nuclear species. Multidimensional spectroscopy has further been combined with rapid-ΔT DNP without MAS to achieve considerably higher enhancements, involving work at the Weizmann Institute, utilizing utrafast techniques to obtain enhanced spectra (20% on ^{13}C) from transient dissolution DNP samples,[40] and the *in situ* TJ-DNP correlation spectroscopy work of Robert Griffin at MIT.[61] This latter work, with experimentally realized enhancements $\varepsilon^{\dagger}$ reported around 100, will form the starting point for our experiment.

1.5 TJ-DNP at Nottingham

1.5.1 Our Novel Approach

Despite previous examples of TJ-DNP achieving significant liquid-state NMR enhancements and demonstrating the capability for *in situ* recycling and multidimensional correlation spectroscopy,[61] improvements to the experimental method are anticipated to boost enhancements further. The novel experiment at Nottingham will explore a number of these, employing polarization at higher field and lower temperature than previously attempted using TJ-DNP with a novel temperature jump driven by a mid-IR Er:YAG laser. Although dissolution DNP methods have been reported using polarization temperatures down at 1.2 K, these often shuttle the sample between a lower polarization field to a higher NMR acquisition field, decreasing the enhancement by a factor of $\sim$3. The experiment at Nottingham will perform polarization and NMR at the same, high field, using cross effect DNP to overcome issues associated with DNP at these field strengths. The experiment will also benefit from polarization mediation and cross polarization using the proton spin to overcome the lengthy direct polarizaion build up times onto ^{13}C. The experiment will be designed with multidimensional correlation spectroscopy as a primary goal, with the ability to recycle the sample for this purpose. As a result, the heating method employed should be non-destructive. Furthermore any enhancement obtained should be greater on balance than that expected from unenhanced experiments, repeated and averaged over the same period of time. Because of this, the time frame for cooling, polarization, heating and re-cooling should be minimal, but the sample should be kept large enough to benefit from a considerable signal strength in the first place.

It is recognized that our experiment, which will reach temperatures around 1 K, will have a longer cooldown period than previous experiments which reach liquid nitrogen temperature. Despite this factor threatening to reduce the SNR per unit time compared to other experiments, the overall gain in signal will more than compensate for this. For example, literature describes a benchmark experiment in which an enhancement of $\varepsilon^{\dagger}$ $\approx$100 was achieved using a recycling protocol that cycled between $\sim$100 K and $\sim$300 K and took about 1 minute in total.[61] If this experiment were to employ a polarization temperature of $\sim$1 K an additional enhancement factor of 100 could be realized, boosting $\varepsilon^{\dagger}$ to around 10,000. To put this into perspective, the benchmark experiment would need to be averaged for just under 8 hours to benefit from a comparable SNR. This suggests that, provided our novel experiment is capable of a total recycling period on the order of a few hours, a considerable increase in the available enhancement should be realized.

1.5.2 Experimental Procedure

The temperature-jump experiment requires a sample containing both free electron and nuclear spin populations over which the dynamic polarization can occur. This sample is placed in a strong, homogeneous magnetic field at cryogenic temperature, allowing a high level of polarization to build up on the electron spin ensemble. Once polarization has built up to a significant level on the electron population it can be transferred, while at low temperature, to a fraction of the near-by nuclear spin ensemble using tuned microwave irradiation. Because the relaxation of the nuclear spin occurs over a significantly longer period than the electron spin, this process may be repeated using microwave pulses, building up a high level of polarization on the nuclear spin population. After sufficient polarization transfer and nuclear polarization build-up, the microwave pulses are stopped and the sample is brought rapidly to ambient temperature for a liquid-state NMR experiment. This stage needs to be as fast as possible to ensure that only a small fraction of nuclear polarization is lost due to longitudinal relaxation. Provided the rapid heating mechanism does not destroy the sample it can be recycled and brought to low temperature again for further TJ-DNP. This is shown in figure 1.1.

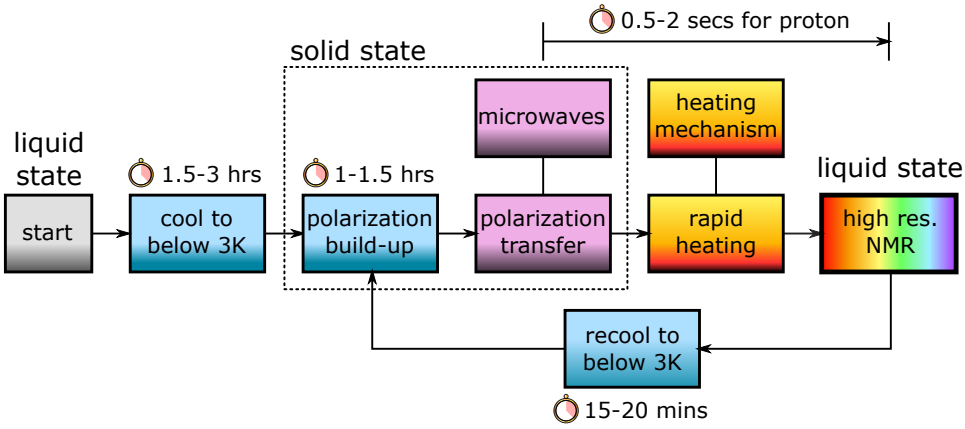

Figure 1.1: The temperature-jump DNP experiment featuring sample recycling with approximate time scales, adapted from previous work. [39]

1.5.3 Key Specifications

Starting with a sample containing nuclei of interest and a paramagnetic species, the requirements for the TJ-DNP experiment at Nottingham can now be listed.

- A static, homogeneous **magnetic field**.
- A **low temperature** environment (below 3 K).
- **Microwave** irradiation.
- **Rapid heating** without sample destruction.
- High-resolution, **liquid-state NMR**.

Other than the hardware required to perform the experiment, there are also a number of desirable criteria that could be realized to boost the success of the project.

- The experiment should be cyclic, allowing recycling of the sample for applications such as multidimensional spectroscopy.
- The time taken for the sample to cool down, both initially and following the rapid temperature rise, should be low so as to maximise enhancement and recycling capability.
- Any cooling should be stopped during the rapid heating stage.
- A method to document the rapid rise in sample temperature should be available, without drastically altering the process.
- Any mechanical vibration should be kept low, as it is destructive to an NMR experiment.
- The hardware should be as modular as possible, allowing it to be easily built upon in the future.

1.6 Thesis Outline

Now that temperature-jump DNP has been introduced and put into a modern context, this thesis will continue to detail progression of the experiment at the University of Nottingham. This will begin by introducing the foundations on which this experiment is built, in Chapter 2, both with regards to the fundamental theory of NMR and DNP and the hardware already available for this particular experiment. The chapters following this will then detail the development of the cooling, heating and NMR stages of the experiment made during the course of this project. This will begin in Chapter 3 with the design of a bespoke cryostat to bring the sample down to 1.75 K, presented alongside the reasoning for the design and development work into creating the low temperature environment. Chapter 4 describes the amount of heat required to bring the frozen sample to ambient temperature and suggests a number of strategies to deliver this energy. Nanoparticle heating and heating using a mid-IR laser are investigated in further detail, alongside practical designs to deliver this heating and initial results. This chapter also details work towards a number of rapid Raman thermometry techniques proposed to accompany and document the rapid temperature rise of the sample. Chapter 5 presents work into the design of a bespoke, modular NMR probe to achieve liquid-state NMR spectra for the TJ-DNP experiment, along with initial results. Finally, Chapter 6 will present an overview of the project, putting developments into the context of the initial project aims and the wider field of DNP. This will include a section highlighting further work and an outlook created by the project.

Chapter 2

Foundations

The work completed at Nottingham requires a starting point, founded both on the fundamental theory of magnetic resonance and the hardware already available to perform the TJ-DNP experiment. This chapter will introduce both the origin of the NMR signal, along with the appropriate physics required to understand how a standard NMR experiment can be enhanced using DNP, and the technologies that already exist in the laboratory around which any bespoke hardware will be developed.

2.1 Introductory Theory

2.1.1 Nuclear Magnetic Resonance

Nuclear and Electron Spin

Fundamental particles are defined using a number of intrinsic physical properties, such as mass, charge, magnetic moment and spin. Spin is a discrete, quantum mechanical property able to take integer or half-integer values, and is represented with an I. This spin has a secondary quantum number, m_I, which describes the z-component of the spin and takes the values $-I$, $-I+1$, ..., $I-1$, I (see figure 2.1).

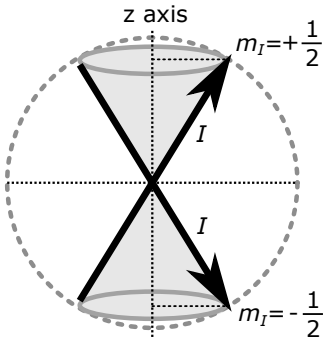

Figure 2.1: The azimuthal projection of the nuclear spin-$\frac{1}{2}$ vector.

Nuclei may possess overall spin, resulting from the spin values of their constituting particles. These composite proton and neutron spins arrange themselves such as to minimise the net spin of the nucleus, with odd numbers of either resulting in a non-zero nuclear spin value. A magnetic dipole moment, $\vec{\mu_I}$, is associated with any nuclei where $I \neq 0$, the strength of which is proportional to the quantum number $\vec{I}$ and a characteristic, isotope-dependent gyromagnetic ratio, γ_I.

$$\vec{\mu_I} = \gamma_I \hbar \vec{I} \tag{2.1.1.1}$$

In this expression $\hbar$ is Planck's constant divided by 2π. Much like the nucleus, the electron possesses intrinsic spin, $S = \frac{1}{2}$. However, unlike nuclei which are considered to be fixed in space, the electron has an associated orbital angular momentum, meaning the overall spin depends on both this and the intrinsic electron spin. The magnetic dipole moment associated with the electron spin angular momentum, $\vec{\mu_S}$, can be written

$$\vec{\mu_S} = -g\frac{\hbar e}{2m_\mathrm{e}}\vec{S} = \gamma_S \hbar \vec{S} \tag{2.1.1.2}$$

and is far greater than that of the nuclear spin.[2] The g-factor, $g \approx 2$, is a dimensionless correction factor for the classical treatment of the spins.

Spin Energy

Protons, electrons and neutrons all possess spin number $\frac{1}{2}$, meaning that there are two possible secondary quantum numbers, $m_S = +\frac{1}{2}, -\frac{1}{2}$, corresponding to a spin-up and a spin-down spin state respectively. Although a great number of nuclei exist with non-zero spins where $I \neq \frac{1}{2}$ these will not be discussed further as they fall outside the initial scope of this project. The magnetic moment associated with the nuclear or electron spin experiences a torque, $\vec{T}$, when placed in an externally applied magnetic field $\vec{B_0}$.

$$\vec{T} = \vec{\mu} \times \vec{B_0} \tag{2.1.1.3}$$

This torque will act to bring the magnetic moment into alignment with the applied magnetic field and cause it to precess about the quantized field axis, as indicated in figure 2.2.

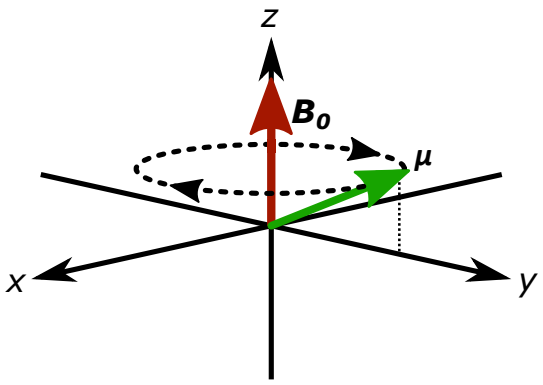

Figure 2.2: A figure to show how placing a magnetic moment $\vec{\mu}$ in an externally applied magnetic field $\vec{B_0}$ results in a torque which causes the moment to precess about the z-axis.

The potential energy of a magnetic dipole in an externally applied magnetic field, $\vec{B_0}$, is given by equation 2.1.1.4.

$$E = -\vec{\mu} \cdot \vec{B_0} \tag{2.1.1.4}$$

Substituting equation 2.1.1.1 into 2.1.1.4, and using $m_S = \pm\frac{1}{2}$, results in two allowed energies for spin-$\frac{1}{2}$ particles.

$$E = \pm\frac{\gamma\hbar B_0}{2} \tag{2.1.1.5}$$

These two energies correspond to a parallel or anti-parallel alignment between the z-projection of the spin and the magnetic field axis. It follows that the energy difference between these two separate states, ΔE, is given by equation 2.1.1.6.

$$\Delta E = \hbar\gamma B_0 \tag{2.1.1.6}$$

In the absence of an externally applied magnetic field ($B_0 = 0$), the energies of the states are equal, meaning they are degenerate and equally populated.

Polarization

This degeneracy is broken in the presence of an externally applied magnetic field, as the energy required to align the spin states anti-parallel is greater than that required to align them parallel, causing a slight disparity between the spin state populations given by Boltzmann statistics. This imbalance manafests an overall magnetization vector for the system, $\vec{M}$. The ratio of spin state populations is given by equation 2.1.1.7.

$$\frac{N_\beta}{N_\alpha} = \exp\left(\frac{-\hbar\gamma B_0}{kT}\right) \tag{2.1.1.7}$$

In this expression, N_β and N_α are the number of spins in the anti-parallel and parallel energy states respectively, k is the Boltzmann constant and T is the temperature of the system.

The signal achieved in a standard NMR experiment arises from the net magnetization caused by this spin state population disparity. The net polarization, P, is calculated as the the ratio of the difference in spin-state populations, $N_\alpha - N_\beta$, to the total spin population, $N = N_\alpha + N_\beta$.

$$P = \frac{N_\alpha - N_\beta}{N_\alpha + N_\beta} = \left(\frac{1 - \exp\left(\frac{-\hbar\gamma B_0}{kT}\right)}{1 + \exp\left(\frac{-\hbar\gamma B_0}{kT}\right)} \right) \tag{2.1.1.8}$$

This expression can be simplified to give equation 2.1.1.9.

$$P = \tanh\left(\frac{\hbar\gamma B_0}{2kT}\right) \tag{2.1.1.9}$$

This may be used to calculate the equilibrium polarization for any spin ensemble experiencing a static field at a particular temperature. For ^{13}C nuclei in a magnetic field of 9.4 T, room temperature polarization can be calculated with $\gamma = 10.708$ MHzT^{-1} (see table 2.1) at around $8{\times}10^{-5}$ %. It is this tiny value that constitutes the main weakness of the NMR experiment. The polarization levels for a number of different spin species at varying temperatures has been plotted in figure 2.3.

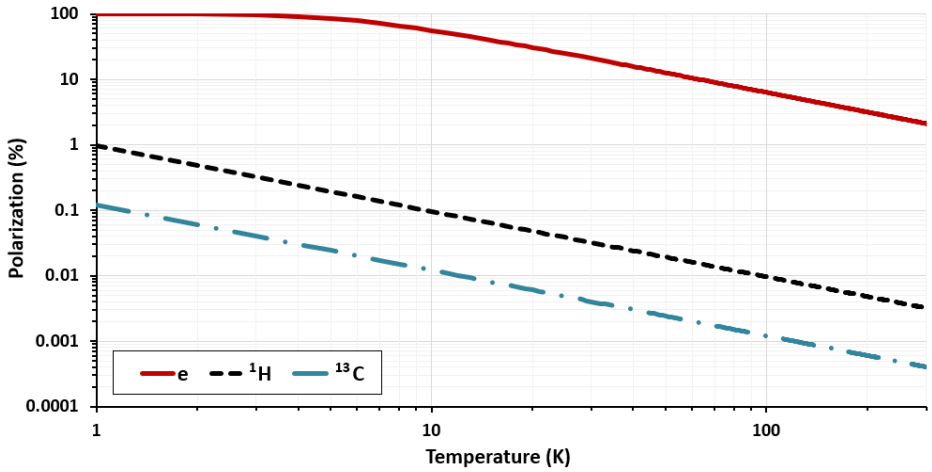

Figure 2.3: A comparison of the Boltzmann polarization calculated using equation 2.1.1.9 for the electron, ^{1}H and ^{13}C spin. $B_0 = 9.4$ T, with electron polarization approaching 100% just below 3 K.

The Larmor Frequency

Magnetic moments precess about the z-axis of an applied B_0 field (thus in the x-y plane) with a frequency proportional to the strength of the field. This precession frequency is called the Larmor frequency, ω_0.

$$\omega_0 = -\gamma B_0 \tag{2.1.1.10}$$

Although magnetic moments aligned with the B_0 field subtend a small angle with the applied field, and thus do not experience large precession, it is possible to manipulate these spin vectors using a second, orthogonal and oscillating field. If this second field, B_1, oscillates at the Larmor frequency of the spins then energy will be added to the system in phase and their vectors will be tipped into the x-y plane where they will continue to precess about the z-axis at ω_0.

Signal Acquisition

A coil may be coupled to the spin system such that the a current will be induced as a result of any transverse magnetization vector precessing in the x-y plane (see figure 2.4).

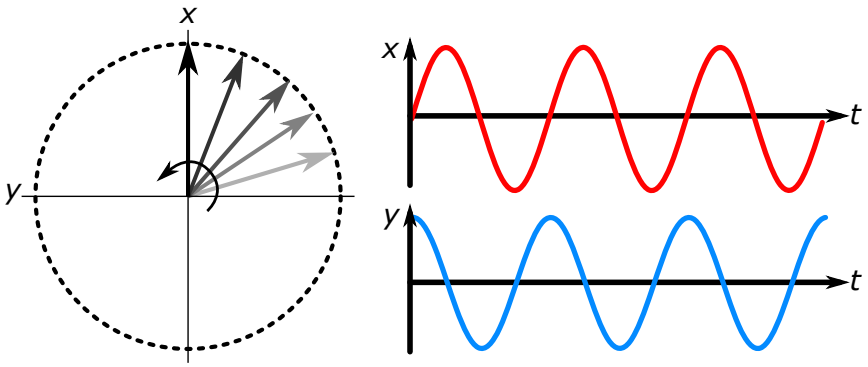

Figure 2.4: The image on the *left* represents the magnetization vector precessing about the z-axis (in the x-y plane), inducing an oscillating current shown on the *right*. It should be noted that this figure does not factor in relaxation back to thermal equilibrium, and the induced signal remains constant.

This signal will exhibit characteristic frequencies of oscillation dependent on the magnetic field experienced by the spins as they precess about the z-axis. Spins experiencing slight deviations in field will precess with an adjusted precession frequency, as can be incurred from equation 2.1.1.10. The overall signal will therefore be a superposition of all spins precessing at the frequencies corresponding to their own local environments. This frequency domain information can be extracted from the oscillating time domain signal using a Fourier transform, which takes an input in the time domain, $s(t)$, and converts it to an output in the frequency domain, $I(\omega)$.

$$I(\omega) = \int_0^\infty s(t)\exp^{-i\omega t}\mathrm{d}t \tag{2.1.1.11}$$

This allows the separate frequency components present in an oscillating signal to then be evaluated, such that the spin system and spin environments may be investigated.

Spin Relaxation

In reality, the magnetization precessing in the x-y plane will decrease as time goes on and the spins return to equilibrium via various relaxation processes. This means that the any oscillating signal induced in the coil will decrease in amplitude with time. This behaviour gives rise to the name of the signal, the free induction decay (FID). The FID is both characteristic of the precession frequencies and relaxation pathways present in the spin system, and can be used to deduce properties related to these processes. A great number of experiments focus on these relaxation parameters, as well as the frequencies of precession, to investigate matter.

Longitudinal relaxation, or T_1 relaxation, comes about as the magnetization vectors precessing in the x-y plane return to thermal equilibrium along the z-axis of the field. The mechanism for this relaxation depends on molecular motion, and is therefore temperature dependent. The correlation time, τ_C, is used to describe the average time taken for a molecule to rotate by one radian,[71] and is slow in solids and fast in ambient liquids. Effective relaxation occurs when the molecular motion is on the order of the spin precession frequency, ω_0. This results in a very strong relaxation, damaging to the NMR signal, as a sample rises from 0 K to 300 K, as shown in figure 2.5.

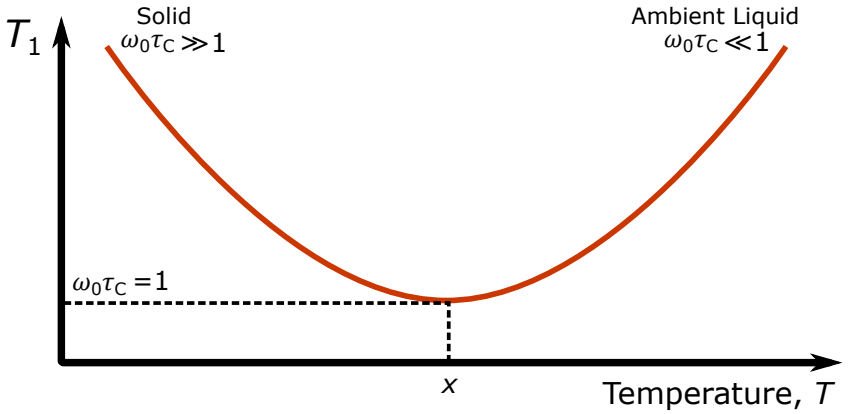

Figure 2.5: A plot of T_1 as a function of temperature, T. Longitudinal relaxation, which is destructive to the enhancement of the DNP experiment, is fastest at the temperature x where $\omega_0\tau_0 = 1$.

Transverse relaxation, or T_2 relaxation, is caused by local magnetic spin environments introducing deviations to individual spin precession frequencies, resulting in a dephasing of the coherent magnetization. In reality, field inhomogeneity and spin mobility mean that, as the magnetization vectors move into areas of varying field strength, this dephasing occurs faster with a time constant T_2^*. This makes this spin-spin relaxation a rapid and irreversible mechanism of relaxation.

2.1.2 Dynamic Nuclear Polarization

Dynamic nuclear polarization is the process of transferring high levels of polarization from an ensemble of electrons to nuclei of a lower gyromagnetic ratio using microwave irradiation. This artificially increases the polarization of the target nuclei and subsequently the sensitivity of an otherwise weaker NMR experiment. Understanding this method of signal enhancement requires an in depth description of the system formed by these interacting ensembles and an idea of the time scales over which these interactions take place, which will be presented in this section.

The Electron, the Nucleus and the Overhauser Effect

Considering a pure and isolated quantum system formed by an electron spin, S, and a nuclear spin, I, both with spin $\frac{1}{2}$, produces four distinct spin states of the form $|m_S m_I\rangle$. These states can be labelled using α_x and β_x to denote a spin-down or spin-up particle respectively, giving the four pure eigenstates $|\beta_S\beta_I\rangle$,$|\alpha_S\beta_I\rangle$,$|\beta_S\alpha_I\rangle$ and $|\alpha_S\alpha_I\rangle$, illustrated in figure 2.6.

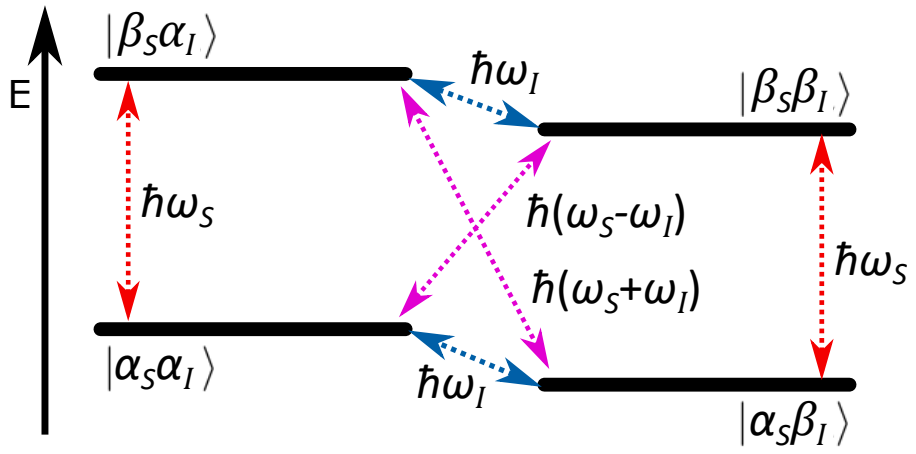

Figure 2.6: An energy diagram of the 4 pure eigenstates associated with a coupled electron-nucleus spin pair. Electron or nuclear spin flips may be performed state to state by irradiation with a suitable energy ($\hbar\omega_I$ for a nuclear spin flip (*blue*) and $\hbar\omega_S$ for an electron (*red*)). The conservation laws of quantum mechanics make the zero spin flip $\hbar(\omega_S+\omega_I)$ and double spin flip $\hbar(\omega_S-\omega_I)$ transitions very unlikely to occur.

Single spin flip transitions are driven by energy matched to the Larmor frequencies of the particles and, as a result, higher energies are associated with spin flips in greater B_0 fields. This energy may be provided by lattice phonons, causing spontaneous relaxation of the states, or external radiation. The selection rules of quantum mechanics constrain transitions between the states to be energy conserving single spin flips, and thus do not allow direct electron-nuclear spin exchange. Polarization transfer from electrons to nuclei is made possible due to cross relaxation, mediated by molecular motion of the spin ensemble in a fluid or mobile electrons in metallic solids (such as lithium in the famous proof-of-principle experiment,[13] mentioned in section 1.2), and has recently been reported in insulating solids using MAS DNP.[72] Polarization via cross relaxation of species in this manner is known as the Overhauser effect.

The Solid Effect

Molecular motion and rotation are more restricted in the solid-state, and the Overhauser effect is not the dominant method of DNP (unless the solid has highly mobile electrons). In this case, dipole-dipole interactions that would otherwise be averaged out by the motion introduce additional mixing terms to the pure spin eigenstates of the system, with the corresponding eigenvectors:

$$\begin{aligned} |\mathrm{a}\rangle &= p|\beta_S\beta_I\rangle - q^*|\beta_S\alpha_I\rangle \\ |\mathrm{b}\rangle &= p|\beta_S\alpha_I\rangle + q|\beta_S\beta_I\rangle \\ |\mathrm{c}\rangle &= p|\alpha_S\beta_I\rangle + q^*|\alpha_S\alpha_I\rangle \\ |\mathrm{d}\rangle &= p|\alpha_S\alpha_I\rangle - q|\alpha_S\beta_I\rangle \end{aligned} \tag{2.1.2.1}$$

where p and q represent the probability of the spin flip taking place, adopting values $p \simeq 1$ and $q \ll 1$ (but still greater than zero).

These perturbations now introduce a non-zero probability of an otherwise forbidden spin flip taking place. Although there is a non-zero probability for these spin flips to occur, single spin flips are still far more likely due to the fact that q is much smaller than p. Using an external energy source tuned to the double quantum transitions (microwave regime) will drive these less likely electron-nuclear spin transitions. This microwave frequency also needs to be higher for systems exposed to higher B_0 fields.

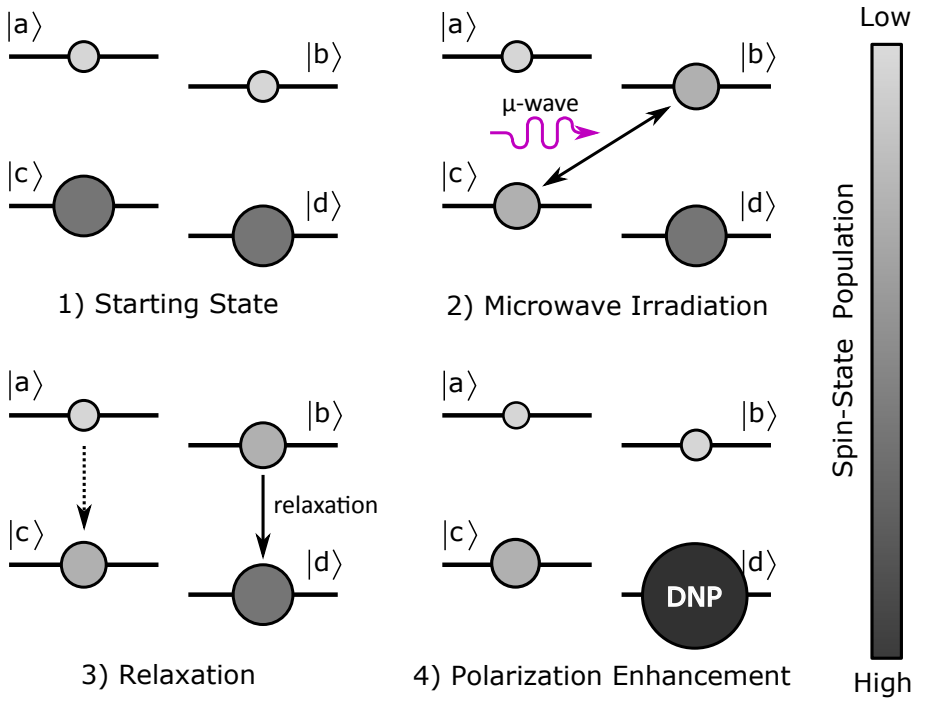

Figure 2.7: A figure to show solid effect DNP between an electron and nuclear spin system in a low temperature solid. To begin the spins are polarized with a Boltzmann distribution (1). Forbidden quantum transitions may then be irradiated with microwaves to equalize the populations between either |a⟩ and |d⟩ or |b⟩ and |c⟩ (2) before the artificially populated high energy states relax (3). This boosts the population of either spin-state |c⟩ or |d⟩, such that an increased NMR population difference is present (4). This process may be repeated using the fact that the electron spin relaxation is far faster than that of the nucleus.

The high Boltzmann polarization of the electron is transferred to the nuclear spin ensemble by double quantum transitions driven by tuned microwave radiation. Since the longitudinal relaxation of the electron

spin is much faster than that of the nuclear spin, $\sim 10^3$ s^{-1} and $\sim 10^{-3}$ s^{-1} respectively,[73] the electron spins return to equilibrium far quicker than the nuclear spins. This allows spin polarization to be pumped from the electrons to the nuclei, generating a highly polarized nuclear ensemble within the sample. This process, shown in figure 2.7, is known as the solid effect[74] and is the primary source of polarization enhancement when microwave irradiation ω_{MW} is applied at the electron-nuclear zero- or double-quantum transition ($\omega_{\mathrm{MW}} = \omega_S \pm \omega_I$). This mechanism relies on a coupled electron and nuclear spin that is isolated from other spins such that their resonance profile is narrow, and on short electron T_1 times, allowing the spins to be recycled and the polarization to build up. It should be noted that the efficiency of the solid effect DNP process scales with ω_I^{-2}, rapidly decreasing with increasing magnetic field.[74,75] In reality it is likely that electrons and nuclei in the sample are coupled to many other spins, resulting in additional DNP pathways.

The Cross Effect and Thermal Mixing

The cross effect relies on electron-electron-nuclear interactions, where the condition for polarization transfer is such that the resonant frequencies of the two electrons must be separated by the Larmor frequency of the nucleus, as shown in equation 2.1.2.2.

$$\omega_I = |\omega_{S1} - \omega_{S2}| \tag{2.1.2.2}$$

This condition may be experimentally realized by introducing free radicals with broad and inhomogeneous electron resonances or by introducing specific biradical molecules with fixed electron separations.[76] Provided this resonance condition is matched, polarization may be built up on the

nuclei of interest at a rate that scales with ω_I^{-1}. This makes the cross effect the dominant DNP mechanism at higher field strengths,[77] and of particular interest to this project where the magnetic field of the spectrometer is 9.4 T. In the case that many electrons and nuclei interact a thermodynamic model is used to describe the polarization transfer. This is then known as thermal mixing, using interacting ensemble baths with defined spin temperatures.[78,79]

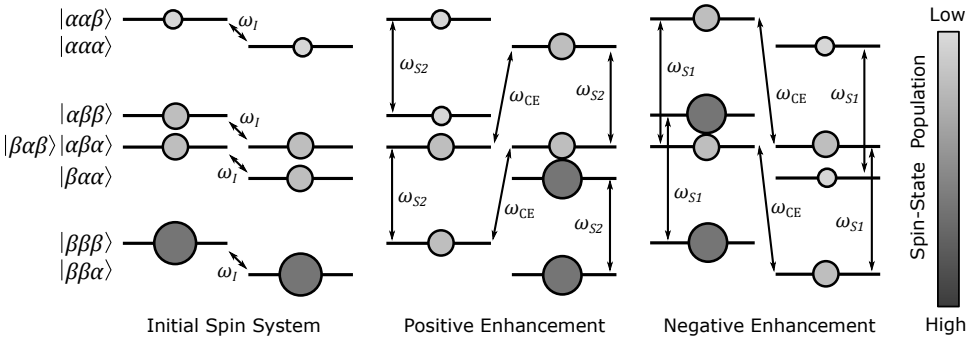

Figure 2.8: An adapted[80] figure to show cross effect DNP in a three spin system. The energies of the levels are in the form $|m_{S1}\ m_{S2}\ m_I\rangle$. The opposite signs of the nuclear spin population differences achievable using this method introduce both positive and negative enhancements.

2.2 Established Technology

The TJ-DNP experiment at Nottingham requires large scale hardware to be designed to fulfill a number of experimental conditions. Where possible, this design will build off of existing technology and use hardware already available. This section will introduce the requirements of the DNP sample, the microwave bridge used for the experiment and the NMR spectrometer around which the TJ-DNP experiment will be built.

2.2.1 Sample

While it is true that a temperature-jump DNP sample requires coupled electron and nuclear spins to be present, the exact requirements for the system are experiment dependent, and the sample needs to be designed with extra considerations in mind. This results in a more complicated sample which matches additional criteria, allowing a highly polarized nuclear spin ensemble to be realized.

Free Radical

It is possible to utilize the free electron of a number of radicals, atoms or groups of atoms with at least one unpaired valance electron, which may be dissolved within a solvent for DNP purposes. A number of stable radicals have been developed for use as polarization targets in DNP[81,82] which tend to use atomic screening to harbour stable paramagnetic centres. The choice of radical depends on the experiment, with each designed to offer a spin system and EPR lineshape that is optimized for a particular DNP mechanism. This lineshape depends on a number of factors, such as the g-factor and orientation dependence of the electron, with the effective resonance being broadened and influenced by local fields.

Narrow, homogeneously broadened lineshapes can be expected from free radicals with high levels of symmetry around the electron, giving more isotropic g-tensors. This symmetry also ensures orientation dependent interactions average out any effects that do arise from any g-anisotropy. Wider, inhomogeneously broadened lineshapes can be obtained using free radicals with lower levels of symmetry, resulting in orientation dependent spin resonance profiles. Examples of two radicals used for DNP with dramatically different g-anisotropy values are shown in figure 2.9.

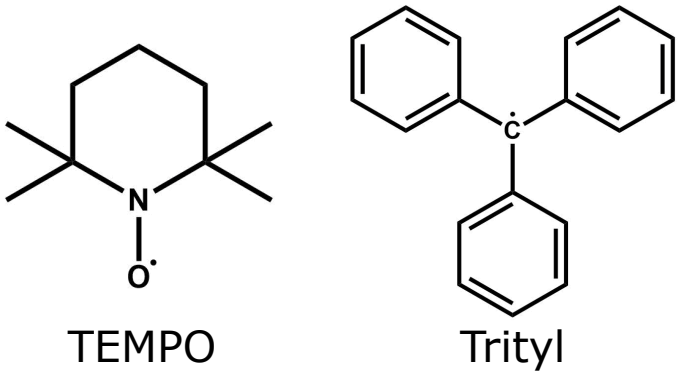

Figure 2.9: The structure of two commonly used stable radicals for DNP. TEMPO, with a high level of g-anisotropy, shows a broad and inhomogeneous EPR lineshape, whereas Trityl exhibits a narrow, symmetric linewidth due to the symmetry of the molecule and isotropic g-tensor of the free electron.

Certain DNP mechanisms dominate under certain conditions, with the solid effect prominent when the EPR linewidth is small compared to the nuclear Larmor frequency, and both the cross effect and thermal mixing prominent when the EPR linewidth is larger. The symmetric structure of Trityl makes it a strong candidate for solid effect DNP,[83] whilst the less-symmetric environment of the nitroxide TEMPO makes it suitable for cross effect and thermal mixing DNP.[84] This method requires broad lineshapes to ensure the $\omega_I = |\omega_{S1} - \omega_{S2}|$ resonance condition is matched, with inhomogeneous profiles reducing cancellation effects caused by both the positive and negative enhancements shown in figure 2.8. The difference in the electron Larmor frequencies can be physically

altered to match the nuclear resonance condition by either changing the concentration of the radicals within the sample or by introducing secondary, strongly-coupled paramagnetic centres. This latter method, performed by synthesizing biradicals (figure 2.10), allows the conditions for DNP to be carefully matched by tailoring the length of the molecule, and thus the electron-electron dipolar coupling.[76,82]

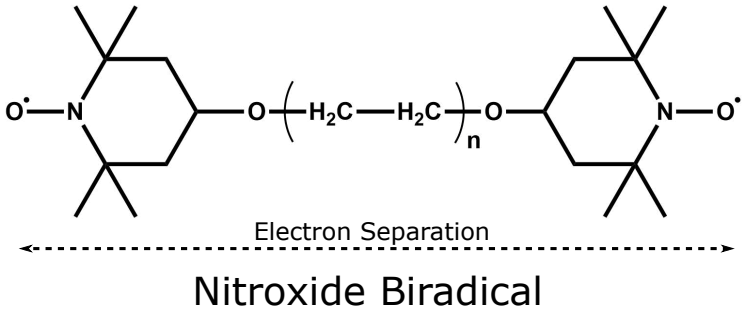

Figure 2.10: The electron distance of the nitroxide biradical can be tailored for specific applications, matching the electron-electron dipolar coupling to the experiment.

The choice of free radical depends upon the experiment and dominant DNP mechanism driving the polarization enhancement, as well as price and availability. It is also possible to use mixtures of the two to optimize the experiment.[85,86] This experiment will aim to use the water soluble biradical TOTAPOL to utilize the cross effect present at the high fields used for this project and to mirror similar TJ-DNP experiments.[39] This biradical is already widely used to study nucleic acids and proteins, and has been shown to give high enhancement at low concentrations.[87]

Nuclei of Interest

The main nuclei of interest for this project is carbon-13 (^{13}C), although the proton (^{1}H) will also be useful during initial testing. As can be seen in table 2.1, the gyromagnetic ratio of the electron is far greater than that of both the proton and carbon-13 resulting in a maximum enhancement in polarization of ∼660 and ∼2600 respectively.

Spin	**Gyromagnetic Ratio** (MHz/T)	**Abundance** (%)	**Relative Sensitivity** (Const. B_0)
e^-	28024.953	n/a	658.203
^1H	42.578	99.985	1.000
^{13}C	10.708	1.070	0.252

Table 2.1: A table of NMR relevant data for the electron, proton and carbon-13.

Although the DNP enhancement associated with ^{13}C is large, it is necessary to factor in the time taken to polarize these nuclei, as this build up time varies across species. For the case of ^{13}C it has been shown that polarization build up from the electron spin population to that of the proton spins, followed by cross polarization to the carbon nuclei builds up polarization far faster than direct polarization transfer,[80] and will be performed in this experiment. Although ^{13}C has a far lower natural abundance, it allows specific labelling of complex molecules, creating a powerful gateway into biologically relevant studies. Samples for these early TJ-DNP experiments will be prepared with high concentrations of small, ^{13}C-labelled molecules, such as ^{13}C-urea, which will be polarized via cross polarization from the ^1H spins also contained in the sample.

Glassing Agent

It is important that the sample forms a glass at low temperatures, rather than a crystalline solid, as crystallization causes various components of the solution to aggregate, decreasing polarization transfer efficiency.[88] Glycerol, a viscous hydrocarbon displaying a number of hydroxyl groups ($C_3H_8O_3$), has been chosen for this particular experiment as its hydroxyl group rich structure is useful during the rapid heating stage chosen for this project (see section 4.4), and also for its bio-protective nature.[89] This latter aspect is useful for the protection

of larger, more biologically relevant samples from the rapid freezing and thawing processes of TJ-DNP. Once past the initial development stage of the experiment a mixture of 60/30/10 (vol%) of d_8-glycerol/D_2O/H_2O can be used, colloqially referred to as "DNP Juice", which has been shown to form an optimal glass for the DNP experiment.[90] It is worth noting that some molecules with paramagnetic centers, such as pyruvate, can themselves be used as glassing agents.[91]

Sample Volume

The sample used for this TJ-DNP experiment will be held within the homogeneous region of the NMR spectrometer using a sapphire sample cup (section 4.4.4). The volume of the sample will be dictated by both the rapid heating mechanism chosen for the experiment and the NMR electronics. In order to more rapidly bring the sample from ∼1 K to 300 K the volume needs to as small as possible, requiring less energy to heat up less mass (equation 4.1.1.1) and allowing faster diffusion of energy throughout. This requirement is also imposed by a lack of space within the spectrometer bore, coupled with the fact that additional hardware also needs to be implimented. However, the NMR signal is proportional to the number of contributing spins within the sample, and so a higher volume of sample would exhibit a higher NMR response. These factors will be balanced by using about a millilitre of sample, so that it is small enough to be heated rapidly, fits comfortably in the available space of the spectrometer bore but also gives a sensible NMR signal. To couple effectively to a laser heating mechanism, the sample will be in the form of a cylinder 4 mm in diameter and 4 mm in height, giving an overall volume of ∼0.2 ml at ambient temperature.

2.2.2 Superconducting NMR Spectrometer

It is possible to achieve high magnetic fields by forming electromagnet sets using superconducting wire. Cooling this wire below a critical temperature allows the material to carry large currents with effectively no resistance, generating intense and stable magnetic fields. Because the material exhibits no resistance, the windings can be charged and, provided they are kept below their critical temperature, keep field once disconnected from the power supply. Because this method allows high, precise magnetic fields to be realized it is a method popular for generating the fields used in NMR, and is often used for spectrometers which keep the windings below critical temperature by submerging them in baths of liquid helium. To stop this helium boiling off rapidly these baths are, in turn, cooled using liquid nitrogen and subsequent super-insulation within a vacuum space.

The static magnetic field used for this project is provided by an unshielded Magnex Scientific 400 MHz spectrometer with a wide-bore diameter of 152 mm and extended supports which increase the clearance below the instrument to just over a meter (1050 mm). The spectrometer has a highly homogeneous isocenter located 485 mm up the bore of the instrument, and the field strength of 9.4 T allows near unity polarization of the electron spin population below 3 K (using equation 2.1.1.9) which is a temperature achievable using liquid helium cryostat technology. The corresponding electron Larmor frequency at this field strength is 263 GHz, for which microwave generation and transmission solutions exist and can be purchased readily.

Although this spectrometer has a wide bore, the passage is restricted to 70 mm towards the base of the instrument by a set of shim coils. These are included to provide tunability of the static magnetic field via the application of external current and increase field homogeneity. Although these secondary coils impose a considerable reduction to the workable space within the spectrometer bore, the inclusion will ensure that any field inhomogeneity caused by hardware added into the spectrometer bore to facilitate the TJ-DNP experiment can be corrected, allowing higher resolution NMR to be achieved. The schematic diagram presented in figure 2.11 shows the spectrometer annotated with key dimensions for peripheral hardware design.

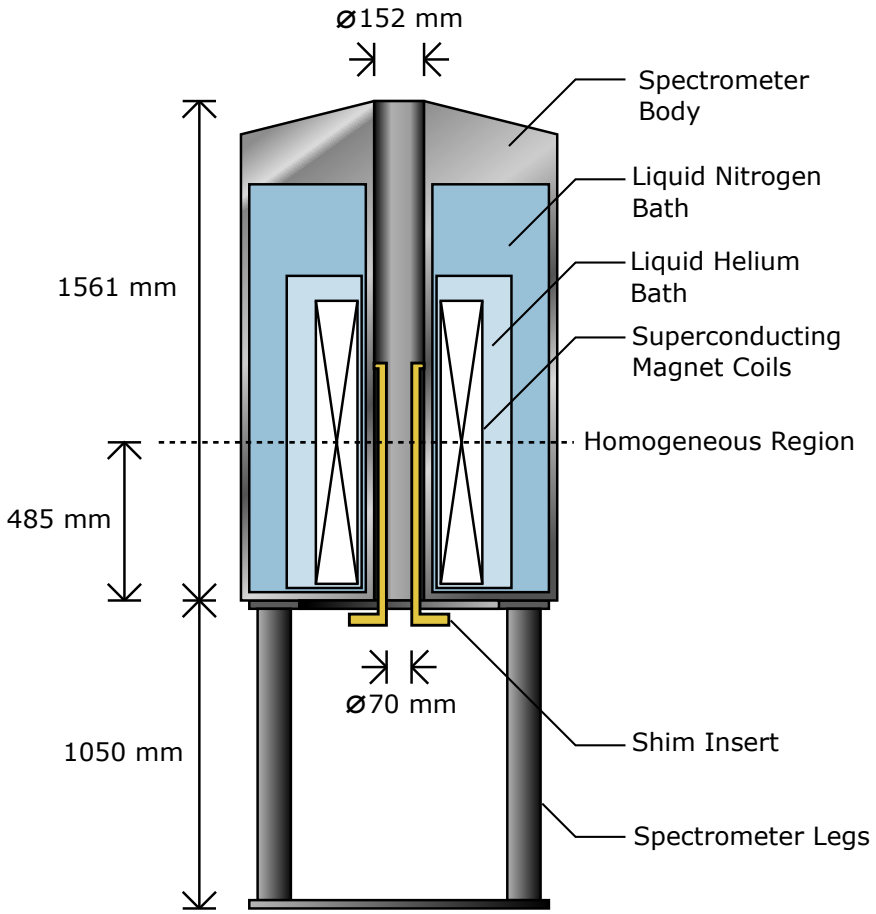

Figure 2.11: This schematic diagram shows the Magnex Scientific 400 MHz spectrometer, including the most notable dimensions for hardware design for the instrument.

Unlike a variety of modern spectrometers, which use additional fields to actively shield the lab environment from stray magnetic flux, the 9.4 T spectrometer used for this project is unshielded. This means that there is a magnetic field present within the lab, shown in figure 2.12, that could attract ferromagnetic components brought too close and effect the function of magnetic equipment. As a consequesnce, magnetic equipment such as vacuum pumps and computers cannot be kept within a few meters (∼5 m) of the magnet.

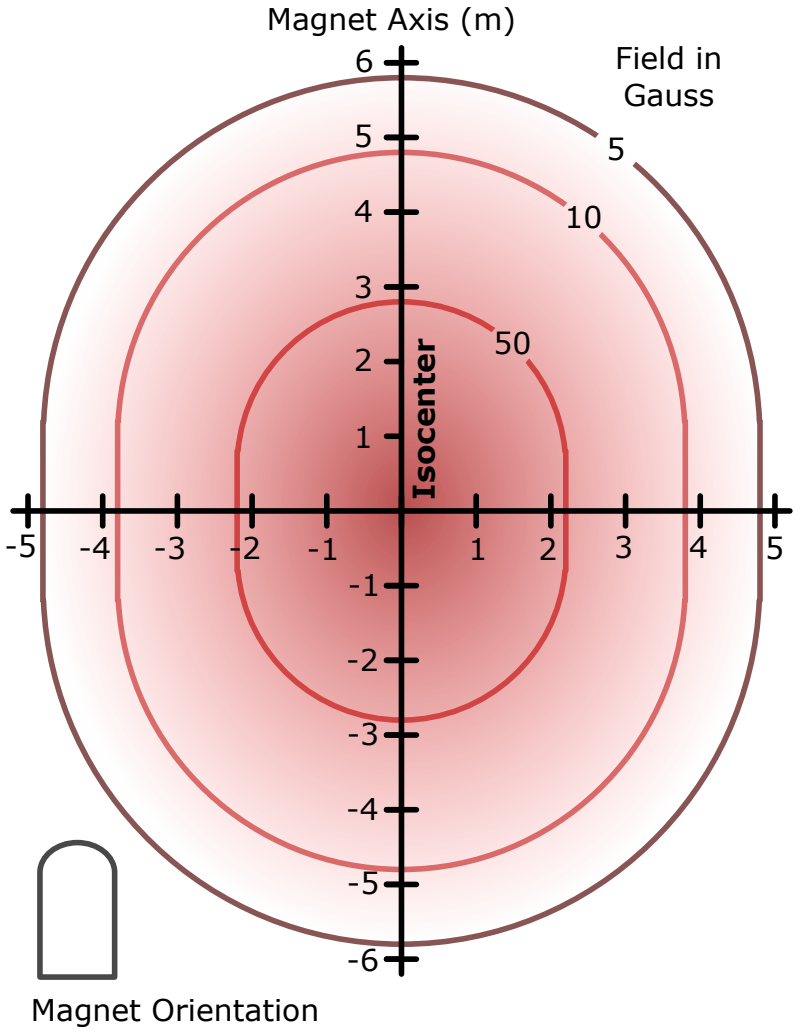

Figure 2.12: The axially symmetric stray field plot of the 9.4 T spectrometer

2.2.3 Microwave Bridge

Circularly polarized microwaves need to be guided into the NMR spectrometer to drive the DNP effect in a frozen sample. Delivery of these microwaves, from synthesis to the top of the NMR spectrometer, is achieved using a microwave bridge designed and built by Thomas Keating Ltd. and these were installed and tested with the help of Kevin Pike.

Microwave Synthesis

High frequency, microwave radiation is generated for DNP applications in a couple of ways, depending on the experimental application. While gyrotron technology is capable of producing powerful beams of microwaves for DNP experiments[92] the generation is expensive and often requires additional cryogens. Alternatively it is possible to use small scale, inexpensive oscillator technology to generate RF signals which can be passed through a series of electrical manipulators to provide frequency tunable, low-power output radiation in the microwave regime.

Microwave synthesis for this project is shown in figure 2.13, and uses an 8-20 GHz Frequency Synthesizer (Virginia Diodes, VA, US), controlled with LabVIEW, to generate frequencies around 16 GHz. This is then fed through a wideband microwave amplifier (Mini-Circuits, NY, US), boosting the signal by 18 dB. This then travels through a directional coupler, such that the signal can be monitored, before passing through a fan-cooled, high power multiplier (Spacek Labs, CA, US), doubling the frequency of radiation. After initial doubling the signal passes through a Virginia Diodes multiplier chain, featuring 3 more doublers, giving an overall frequency multiplication of 16. This signal is then coupled to the microwave bridge using a Gaussian horn.

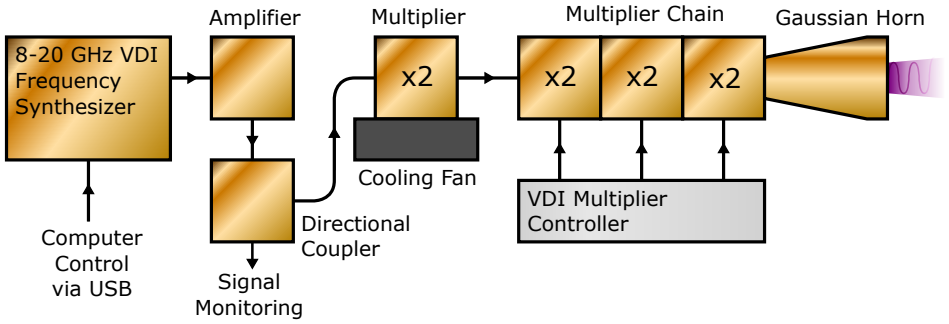

Figure 2.13: A schematic to show microwave generation, amplification and multiplication.

This generates a beam of tunable microwaves at around 263 GHz with a power measured using a THz power meter to be 47.2 ± 0.1 mW and an absolute output deviation of 0.1 mW over an hour.

Quasi-Optic Divergence Correction

When using systems in which the wavelength of electromagnetic radiation is comparable to the dimensions of optical components, diffraction effects become significant and degrade the propigating wavefront. This is the case when using radiation of 263 GHz. To overcome the effects of beam divergence from the source, the microwave bridge employs curved, refocussing mirrors along the beam path.[93] If these mirrors are placed at 45° to an oncoming diverging beam, they refocus the radiation into a waist further down the microwave path (figure 2.14). From this waist the beam will begin to diverge again, requiring periodic inclusion of the mirrors to transmit the beam longer distances (see figure 2.18).

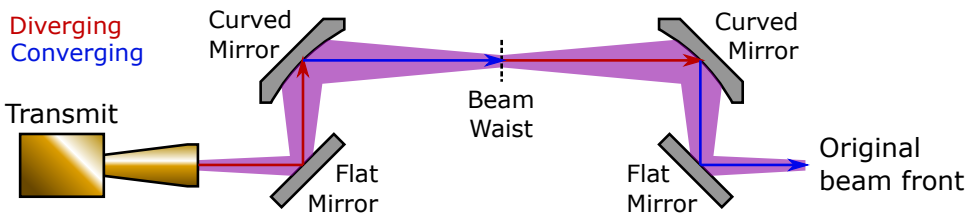

Figure 2.14: A diagram to show how curved mirrors are employed on the microwave bridge used for this project to refocus diverging microwaves.

Signal Isolation

An isolator is included on the microwave bridge to protect the radiation source from any reflections and reduce standing waves along beam length. This is built using a 45° Faraday rotator in conjunction with two wire-grid polarizers,[94] in a configuration shown in figure 2.15. Microwaves entering the isolator from the source experience a Farady rotation of 45° before passing along the rest of the bridge with little loss. However, any reflections that re-enter the isolator experience an additional 45° rotation, adjusting them such that they are deflected along a different path to a sheet of roughly textured radar absorbing material (RAM),[95] which acts as a beam dump. This offers a measured isolation of ∼30 dB.

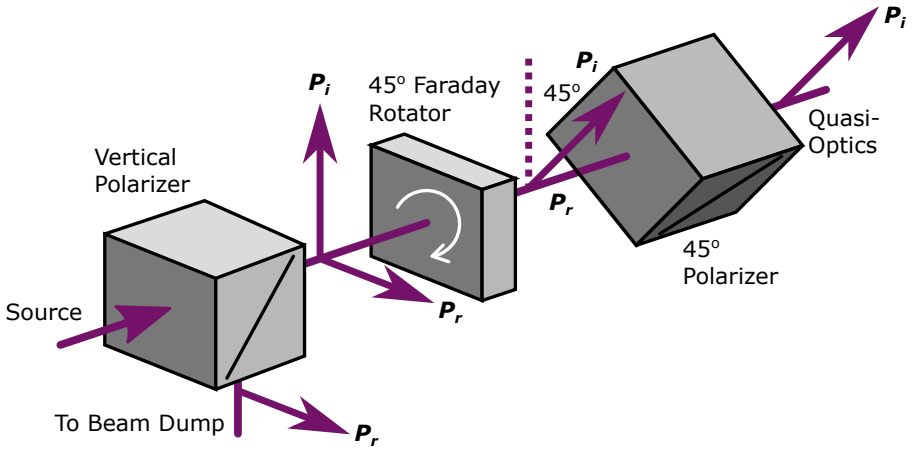

Figure 2.15: The microwave isolator used for this project, created using a planar 45° Faraday rotator sandwiched between two wire-grid polarizers at 45° to one another. P_i indicates the polarization of the incident microwaves and P_r indicates that of the back reflected radiation.

Circular Polarization of the Microwaves

To most efficiently couple the microwaves to the spin system within the spectrometer requires circularly polarized microwave irradiation.[96,97] This increases the effective strength and homogeneity of the field-matter

interaction and allows specific spin states to be addressed and manipulated. Circular polarization is created for this project using a Martin-Puplett interferometer[98] on the microwave bridge. This uses a wire-grid polarizer to split an incoming beam of linearly polarized microwaves into two, orthogonal components, which are directed along two different paths before reflecting back from a roof mirror and recombining. If the path lengths are equal, the recombination produces microwaves with an identical polarization to those entering the system, as there is no phase difference between the two components. Introduction of a path length difference imposes a phase difference that manifests itself as circular polarization of the recombined microwaves[99] (see figure 2.16).

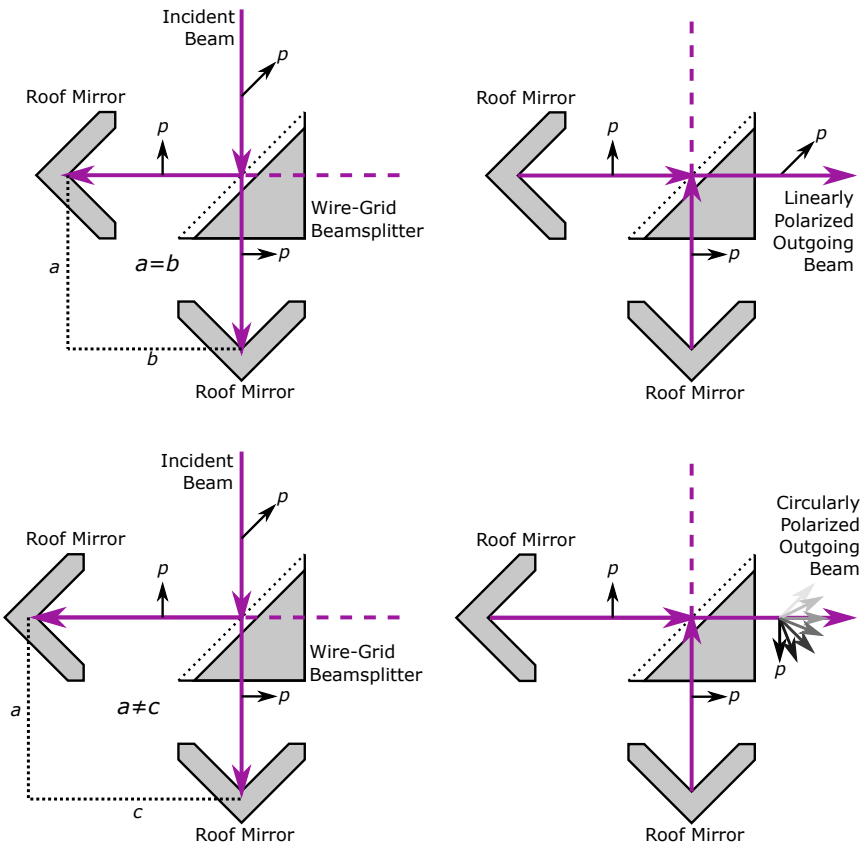

Figure 2.16: A schematic of a Martin-Puplett interferometer, showing how circularly polarized microwaves can be generated by splitting a linearly polarized beam into two, orthogonal components and allowing them to travel different distances prior to recombination.[99]

By introducing a path length difference to the interferometer, with an additional wire-grid polarizer placed after recombination such that the horizontal and vertical components of the microwaves were separated, a power meter was used to locate and lock the point at which there was circular polarization of the beam. This was achieved when the power of the split horizontal and vertical components was equal, shown in figure 2.17. The wavelength associated with the periodic path length differences at which there was verification of circular polarization was measured to be 1.14 ± 0.01 mm, corresponding to a frequency of 263 ± 2 GHz, as expected.

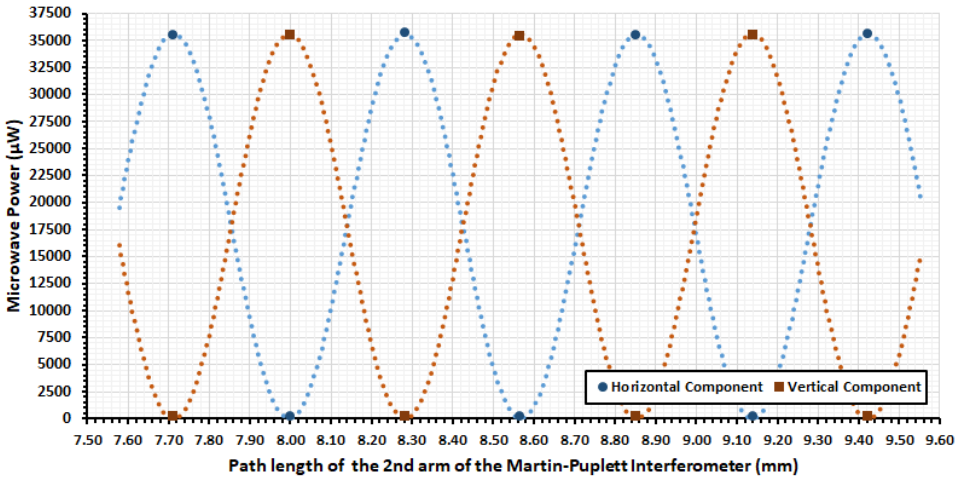

Figure 2.17: A figure to show the measured power of the vertical and horizontal components of the microwave beam as the path length difference is changed on the Martin-Puplett interferometer. The points at which the fitted curves cross give the arbitrary path lengths which generate circular polarization of the microwaves.

Microwave Bridge Schematic

A schematic of the microwave bridge is presented in figure 2.18, showing the location of all of the microwave optics. The irregular shape of the bridge allows the microwaves to be delivered to the open bore at the top of the NMR spectrometer, passing between the cryogenic liquid feeds constraining the space above the superconducting magnet.

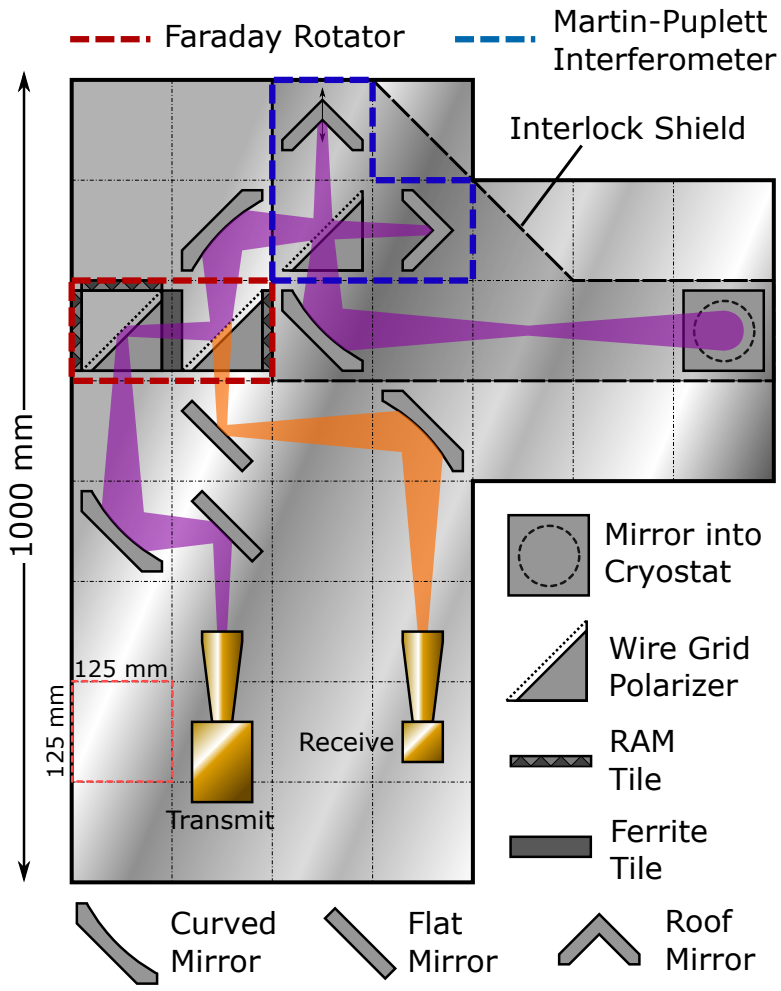

Figure 2.18: The microwave bridge used for this project, with microwave transmission indicated in purple. An orange reflection path is also indicated, which is used to measure various transmission and polarization characteristics of the table.

The surface of the microwave bridge is divided into cells 125 mm by 125 mm, designed for easier distancing and placement of the refocusing optics, and the compact nature of the bridge means that the longest side measures 1000 mm. The interlock shield shown in figure 2.18 was added in house at a later stage and is designed such that no laser radiation can escape the instrument during the rapid heating stage of the TJ-DNP experiment. The power of the microwaves was measured as 31.6 ± 0.1 mW at the entrance to the NMR spectrometer, giving the transmission loss through the microwave bridge itself as 1.74 ± 0.03 dB at 263 GHz.

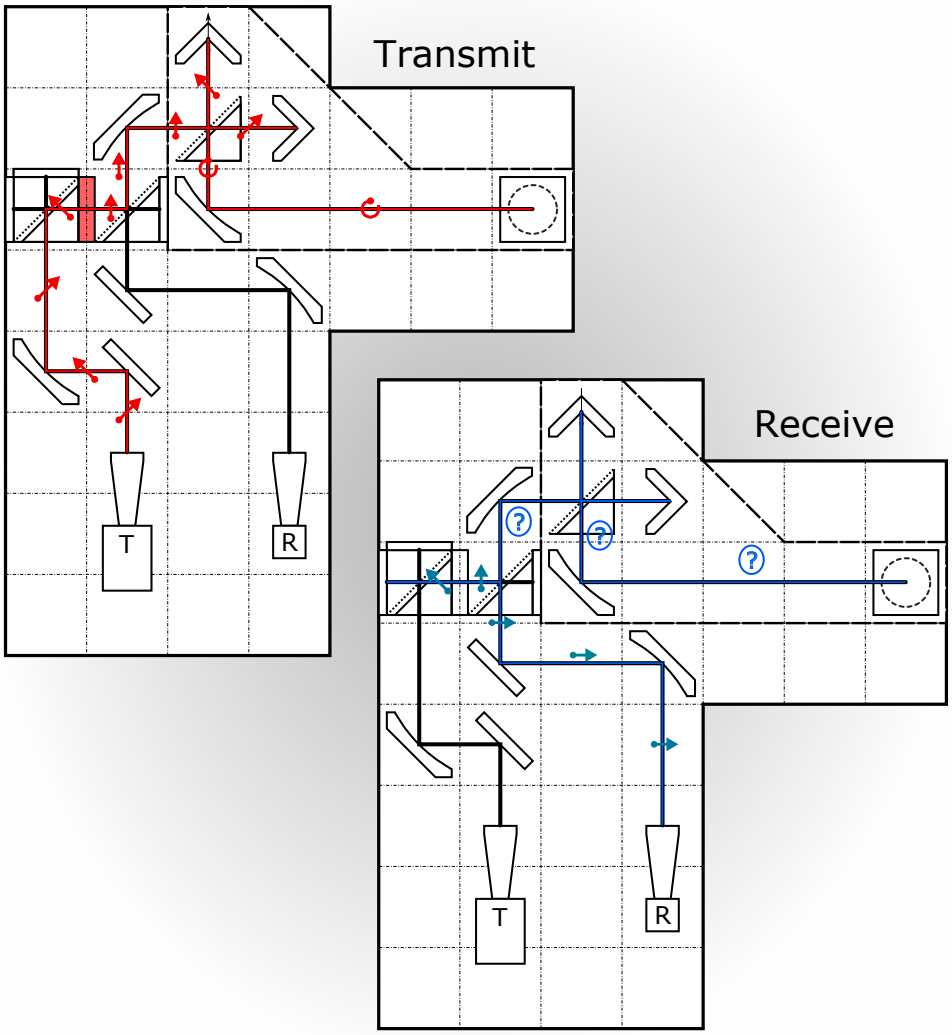

Figure 2.19: A schematic to track the polarization of the microwaves as they pass through the microwave bridge. The red trace indicates the polarization of transmitted radiation, while the blue indicates that of the reflected microwaves.

Details of the microwave polarization are indicated in figure 2.19 for reference, with the components on the bridge the same as those labelled in figure 2.18.

Chapter 3

The Variable Temperature Insert (VTI)

Building on the hardware described in section 2.2, design of an experiment to match the conditions required for the TJ-DNP experiment can begin. The first thing that this requires is a bespoke, low-temperature cryostat in which to allow an electron spin ensemble to reach near unity polarization (see figure 2.3). As this instrument will be inserted into the bore of the NMR spectrometer to realize both a low temperature environment for polarization and an ambient temperature environment for NMR spectroscopy, the cryostat is hereafter referred to as the Variable Temperature Insert (VTI).

This VTI has been designed at Nottingham, following initial discussions with Thomas Keating Ltd., ICE Oxford and Jonathan Cole, and numerous technologies were considered before the final instrument detailed in this chapter was decided upon. Technical drawings were created by Jonathan Cole and the instrument was manufactured at Thomas Keating Ltd. during a period of academic placement at the company.

3.1 Cryogenics

3.1.1 Liquid Helium

Liquid helium (^{4}He) has a boiling point of 4.22 K,[100] far lower than any other element in the periodic table, and is used for a number of low temperature applications. The liquid is available by the Dewar, all be it expensively, making it a costly but suitable liquid to experimentally realize single digit temperatures via immersion. Total immersion of the sample in helium is not realistic in this case, as a rapid heating stage would not be possible, and alternative methods of cooling are required.

3.1.2 Sub-Helium Temperature

It is possible to use a high throughput vacuum pump to reduce the pressure above a bath of liquid helium and reduce its temperature below 4.22 K via evaporative cooling from the surface. The reduction in vapour pressure above the bath effectively lowers the boiling point of the cryogenic liquid, allowing particles with high enough kinetic energy to escape. This then reduces the mean kinetic energy of the remaining helium, lowering the temperature. Temperatures down to $\sim$1 K may be reached using this method,[101] but about 50% of the bath must be evaporated away and the remaining helium must be well thermally isolated from any surroundings. An alternative to evaporative cooling is to use isenthalpic expansion (otherwise known as Joule-Kelvin expansion) of the helium at low temperatures.[102] This method forces an expanding substance to perform work against its own internal forces, and can cool helium provided it is below an inversion temperature to begin (43.2 K).[101] This expansion can be realized using a needle valve, which is a high impedance, controllable orifice, feeding into a low vacuum space.

Helium does not form a solid when taken down to absolute zero at atmospheric pressure, as the molecules have a zero point energy higher than the weak van der Waals interaction that would otherwise bond them together.[101] Despite this, the liquid does transition into a new phase, known as helium-II, below a critical temperature λ_{C} of 2.17 K. This helium-II can be described as two completely mixed, yet separate and entirely non-interacting fluids, helium-I and superfluid phase helium.[103]

While helium-I is simply the proportion of the helium-II exhibiting properties identical to those above λ_{C}, superfluid helium behaves quite differently and gives helium-II some extraordinary properties. ^{4}He is a boson, allowing the matter to occupy identical quantum states and condense into a common lowest energy level when enough energy is extracted from the system.[104] Thus, as helium is cooled past λ_{C}, ordering amongst the ensemble increases (as per the third law of thermodynamics) and a proportion of the matter enters a mutual ground state, creating superfluid helium. This phase has zero viscosity ($\eta_{\mathrm{s}} = 0$) and zero entropy ($S_{\mathrm{s}} = 0$). The remaining fraction of helium-I is distributed amongst various higher energy states and retains the original properties of the matter above this point. Below $\sim$1 K helium-II becomes almost all superfluid.[101] In the absence of viscosity, the superfluid component of helium-II covers any surface with which it comes in contact with a thin film a few atoms thick.[105] This film rapidly evaporates, cooling the surface as it does so, but increasing the vapour pressure above the liquid helium.

3.1.3 Cryostat Technology

Bath Cryostat

It is possible to reach temperatures down to the boiling point of liquid helium on the surface of a large metallic mass, held within a vacuum space, in thermal contact with a bath of liquid helium. The helium bath is fed as it boils away, cooling the mass in turn. Although these systems cannot be used to reach temperatures below the boiling point of helium, and will not be used for the TJ-DNP experiment, this type of cryostat was used during testing of the Raman thermomter detailed in section 4.7.

Continuous Flow Cryostat

Cryostats can also be built which are cooled directly by a feed of cryogenic liquid from a Dewar, with the instrument dropping in temperature as the liquid boils away within the space. This spent helium is then removed via a vacuum system and recycled. This technology allows control of the temperature within the space by adjusting the flow of helium through the instrument, and is capable of realizing temperatures below the boiling point of helium by carefully manipulating the helium feed and the vacuum properties of the inside of the space.

Continuous flow technology is relatively simple and inexpensive, making it a strong contender for the TJ-DNP experiment at Nottingham. By implimenting an intermediate, low temperature helium reservoir within the cryostat space the cooling power of the intrument can be increased. Furthermore, a system of high impedence capillaries in conjunction with a powerful vaccum system could be used to promote Joule-Kelvin expansion and comfortably reach temperatures around 2 K.

Closed Cycle Cryostat

It is also possible to create a cryostat using much the same technology and reaching similar temperatures to the contuous flow design by using a cold head and internal recycling system, effectively reducing helium consumption to zero. These systems are often refered to as 'dry' or cryogen free cryostats, as the technology removes the need to siphon cold liquid helium into the system. Although this instrument would drastically reduce long term running costs and possibly circumvent issues associated with an impending helium shortage, a number of factors make this technology unsuitable for this experiment.

Firstly, although a dry system removes the need for a continuous flow of helium while performing an experiment, the costs of the instrument itself is expensive (about 5 times that of the continuous flow cryostat). On top of the costs of keeping the dry system running, such as powering the cold head inside, any long term saving provided by this technology would not be realized until a number of years of continuous use. For prototyping a novel instrument the option is therefore not sensible. A couple of practical considerations also make the dry system less desirable for TJ-DNP. Vibrations associated with the running of the cold head, used to regenerate liquid helium, are destructive to high resolution NMR. Although discussions were held during the early stages of design to propose a bellows system that would greatly dampen these vibrations, this idea was dismissed as an unnecessary complication compared to other designs. It was also decided that, were anything to go wrong with the dry system, diagnostic work and rapid turnover fixes would be harder to perform when compared to a continuous flow system.

3.2 Practical Considerations

A number of important practical aspects need to be kept in mind while designing the VTI for this project. The majority of matter at low temperature behaves very differently to that at room temperature, often impacting mechanical or thermal properties of the bulk material and making it unsuitable for use. The instrument therefore needs to be designed such that it can reach and withstand sub-helium temperatures, is well thermally isolated from the lab space and such that any chosen materials interfere as little as possible with high-resolution NMR.

3.2.1 Low Temperature Matter

Expansion and Contraction

As the mean kinetic energy of the particles that comprise matter increases, so does the molecular movement and subsequent length and volume of that material. Around room temperature this relationship is described using the expression

$$\Delta L = \alpha L \Delta T \tag{3.2.1.1}$$

where α is the coefficient of linear expansion of a material of length L, and is material specific. While most materials have a small α value (usually of the order of $\times 10^{-6}$ K^{-1}),[100] and small specimens do not exhibit large changes in length when taken through moderate temperature changes, longer examples exhibit more drastic changes in length. It should also be noted that the fractional change in length due to thermal contraction decreases below liquid nitrogen temperatures, as the effect becomes highly non-linear.[101]

Using the spectrometer bore length from section 2.2.2 and the temperature dependent coefficicient of linear expansion quoted for SS-316L[106] (the stainless steel that will be used primarily for this project due to its superior low temperature properties and low magnetic susceptibility) the maximum change in length caused by a cooldown can be calculated. Between 300 K and 1 K this can be estimated at ∼6.5 mm. Although this change is not large compared to the overall length of the bore, this change may be significant enough to introduce strain within the VTI (as the cryogenic space will be at a dramatically different temperature to the outer body of the instrument) and could move the sample out of the homogeneous region of the spectrometer.

In reality the extent to which the VTI changes in length will be much lower than that originally estimated, as the entire length of the instrument will not be at 1 K. It is expected that only a very small region of the interior of the VTI will reach the lower temperature range required for TJ-DNP, with the temperature increasing swiftly as it is measured further from the sample space. Furthermore, the sample is held in place using a bottom-loaded probe which is, in the majority, made from the same material as the VTI (SS-316L) and is about 0.4 times the VTI length. Because the VTI will be fixed in place at the top of the spectrometer, translating a decrease in length as an *increase* in sample height with respect to the spectrometer, and the probe is attached to the base of the VTI, translating a decrease in length as a *decrease* in sample height with respect to the VTI, any contraction and expansion should be largely cancelled out. With these two factors in mind, the real change in sample height brought about by any change in temperature can be estimated to be below 1 mm, and is thus considered negligable.

Material Weakness

Metals, from which the majority of the hardware for this project will be made, may experience changes in ductility and strength when brought to lower temperature. These changes arise due to the trapping of atoms within crystal cells, subsequently decreasing the occurrence of interstitial and vacancy defects within the lattice.[107] The creation of these imperfections at higher temperatures ease the transport of dislocations within the bulk material, allowing the metal to yield at lower levels of applied stress than a perfect crystal and exhibit higher ductility.[108] Some metals remain ductile at lower temperatures because their crystal lattice geometry introduces a greater number of available slip planes through which dislocations may move.[107]

Flexible plastics and rubbers, which are ductile at room temperature, may become brittle at low temperatures. The long-chain polymers that comprise these materials experience reduced mobility as the thermal energy and molecular motion within the system decreases and van der Waals forces become dominant.[109] This loss in ductility often means that the internal stresses introduced by thermal contraction are enough to crack and shatter these materials. Teflon (PTFE) is an example of a plastic that remains ductile at low temperature, as the fluorinated arms of the long-chain polymer continue to contend with the van der Waals forces that would otherwise become dominant as the thermal motion decreases.[110]

3.2.2 Thermal Isolation

In order to build a cryostat capable of reaching temperatures around 1 K, the sample space within the instrument needs to be well thermally insulated from the laboratory. There are three mechanisms of heat transfer that therefore need to be minimized within the space, namely conduction, convection and radiation.

Conduction

Thermal conduction is the transfer of heat through a medium via direct particle interaction, with more energetic particles transferring their energy to less energetic ones, bringing the system towards thermal equilibrium. If there is a temperature difference T along a length x of a material, then thermal collisions will cause heat to flow from warm to cool at a rate given by $\mathrm{d}Q/\mathrm{d}t$.

$$\frac{\mathrm{d}Q}{\mathrm{d}t} = -kA\frac{\mathrm{d}T}{\mathrm{d}x} \tag{3.2.2.1}$$

Here the constant k is the coefficient of thermal conductivity, a material dependent coefficient dependent on density,[111] and A is the cross-sectional area through which heat can flow. In a gas it is the particles themselves that transfer heat, whereas more restricted solid structures rely on phonons and, in the case of electrically conducting metals, electrons. This means that metals are usually good conductors of heat (and subsequently poor thermal insultors). Equation 3.2.2.1 suggests that heat flow via conduction into the sample space can be reduced by either reducing the cross-sectional area in contact with the system, A, or by using materials with lower values of thermal conductivity, k.

Convection

Convection is the transfer of heat via a bulk fluid flow and is the product of both heat conduction through the particles of the fluid and the transport of the fluid itself, often through heating processes. Although convection does not occur within a solid, it may be a relevant heat transfer process if a fluid is in contact with the solid surface. The rate at which heat is transferred via convection may be given by Newton's law of cooling[112]:

$$\frac{\mathrm{d}Q}{\mathrm{d}t} = -hA\mathrm{d}T \tag{3.2.2.2}$$

where h is a density dependent coefficient of convective heat transfer, and all other variables have the same meanings as equation 3.2.2.1. In order to reduce convective heating processes acting upon a sample in the case of the TJ-DNP experiment, surrounding gases will be evacuated so as to decrease their concentration and reduce h.

Radiation

Conductive and convective heat transfer is absent within a perfect vacuum, as there is a void of matter which can carry thermal energy, and both k and h are equal to zero. Using an evacuated space is therefore a good way of thermally insulating two separate objects. In reality it is impossible to achieve a perfect vacuum or to suspend a system (in our case) such that it does not contact its surroundings, and both k and h are not equal to zero. Even in a perfect vacuum the mechanism of radiative heat transfer is still present, caused by the oscillating motion of energetic matter creating electromagnetic waves which permeate through the vacuum.

The rate of this radiative heat transfer is governed by

$$\frac{\mathrm{d}Q}{\mathrm{d}t} = \varepsilon\sigma A(T_{\mathrm{high}}^4 - T_{\mathrm{low}}^4) \tag{3.2.2.3}$$

where ε is the emissivity of the material and $\sigma = 5.67 \times 10^{-8}\ \mathrm{Wm^{-2}K^{-4}}$, the Stefan-Boltzmann constant.[111] This miniscule value for σ means that radiative heat transfer is weak unless the difference in temperature between two surfaces, T_{high} and T_{low}, is very large. This stated, radiative heat transfer becomes the dominant mechanism of heat flow in systems where conductive and convective flow have been minimized using high vacuum spaces.

Reducing Heat Inflow

The cryostat bore will be surrounded by an Outer Vacuum Chamber (OVC), effectively stopping thermal conduction and convection through the walls of the instrument by bringing k and h close to zero. To reduce heat flow into the system where physical support of the sample is required, and contact is necessary, careful material selection is required such that thermal conductivity k is as low as possible. For this reason low-temperature materials such as Macor$^{\mathrm{TM}}$, PTFE and PEEK (polyether ether ketone)[100] are used alongside low-temperature, non-magnetic stainless steel (SS-316L).[113] To further decrease thermal conduction through the hardware, macroscopic breaks are introduced to impede heat flow through the bulk material. This introduces cross-sectional area reductions along the path where the two materials do not perfectly match, subsequently restricting the flow of heat into the space (see figure 3.1). A thermal boundary resistance is also associated with any material interface,[114] such that the heat transport is reduced.

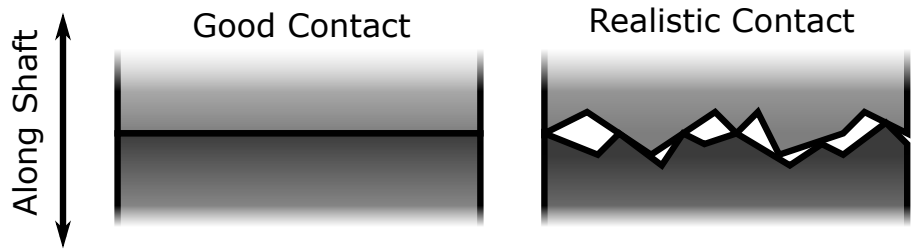

Figure 3.1: An illustration of how the microscopic cross-sectional area through which heat is transferred is reduced in reality by a boundary.

Radiation shields are used in vacuum spaces to reduce radiative heat transfer, usually comprising of a metallic sheet, that acts as a thermal anchor point between the warmer surfaces of the space and the low temperature region. If one shield is used, at ∼50 K for example, the radiative heating into the cold space becomes reduced by a factor of $(295/50)^4 \approx 1200$. Mylar super-insulation may also be used as a radiation barrier, but must not contact the vacuum walls. An additional practical reduction in radiative heating can be brought about by altering the emissivity of the cold surfaces of the VTI. For a black body $\varepsilon = 1$, but for a well polished, metallic surface it is possible to reach values of $\varepsilon = 0.01$. Expanding upon equation 3.2.2.3 to include two surfaces a and b,[101] where $\varepsilon_{\mathrm{a}} \neq \varepsilon_{\mathrm{b}}$, it is possible to see how polishing the inside surfaces of the cryostat, thus reducing emissivity the ε, can decrease radiative heat flow into the space.

$$\frac{\mathrm{d}Q}{\mathrm{d}t} = A\sigma(T_{\mathrm{a}}^4 - T_{\mathrm{b}}^4)\left(\frac{\varepsilon_{\mathrm{a}}\varepsilon_{\mathrm{b}}}{\varepsilon_{\mathrm{a}} + \varepsilon_{\mathrm{b}} - \varepsilon_{\mathrm{a}}\varepsilon_{\mathrm{b}}}\right) \qquad (3.2.2.4)$$

This is the reason that commercial cryostats tend to be highly reflective on the inside and the reason why the VTI for the TJ-DNP experiment at Nottingham will have a highly polished internal space.

The conduction of heat down the shaft holding the sample can be calculated using the thermal resistance of the material, R.

$$R = \frac{L}{k} \tag{3.2.2.5}$$

where L is the length of a shaft with thermal conductivity k. If the shaft is assumed to be a hollow tube, with an outer diamter of 8 mm and an inner diameter of 6 mm (as proposed in section 5.3), the heat flow into the system can be calculated using equation 3.2.2.6.

$$\frac{\mathrm{d}Q}{\mathrm{d}t} = \frac{-A(T_2 - T_1)}{R} \tag{3.2.2.6}$$

For the case of a 600 mm long shaft made entirely from SS316L stainless steel, with one end at room temperature and the other at 1 K, a heat flow of 0.86 W can be estimated. This acts against sample cooling, but aids the heating stage. This conduction can be reduced by making the shaft out of a material with a lower thermal conductivity, or making it from a number of materials. The flow down a composite shaft can be evaluated using equation 3.2.2.7.

$$\frac{\mathrm{d}Q}{\mathrm{d}t} = \frac{-A(T_2 - T_1)}{\sum_m^n R_m} \tag{3.2.2.7}$$

where the thermal resistances of the multiple materials, R_m, add together. Using the same stainless steel shaft as before, but replacing 100 mm at the colder end with Macor$^{\mathrm{TM}}$, the composite steady-state heat flow down the entire shaft is dramatically reduced to 0.26 W. This idea is adopted in the design for the NMR probe to reduce conductive heat tranfer into the cold space (section 5.3.2).

3.2.3 Magnetic Susceptibility Matching

It is important to have a highly homogeneous magnetic field for high resolution NMR, as any magnetic field inhomogeneity introduces differences in the individual Larmor frequencies of the nuclear spins, broadening the precession distribution and subsequently the linewidth of the NMR signal. Placing an object with a different magnetic susceptibility into a perfectly homogeneous magnetic field introduces field gradients, as shown in figure 3.2, as a consequence of the conservation of Maxwell's equations across materials. These distortions in the magnetic field destroys the field homogeneity.

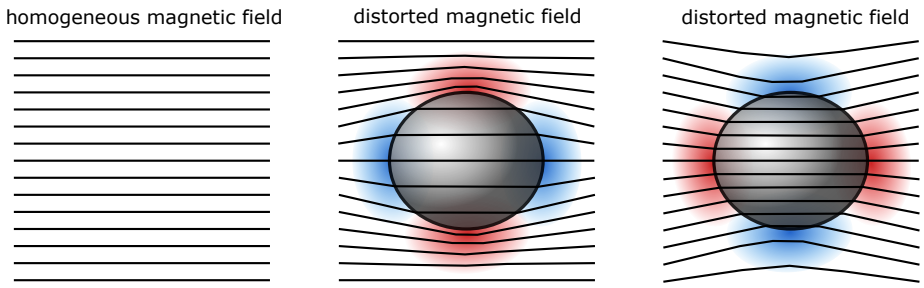

Figure 3.2: A diagram to illustrate magnetic field gradients induced when an object with $\chi \neq 0$ (shown in grey) is placed in a perfectly homogeneous magnetic field. The central image is for a medium with $\chi < 0$, with the right hand image showing the case for $\chi > 0$. The distortions are at their most severe in the regions highlighted in blue and red.

This problem is particularly notable for this project, as a great deal of additional hardware is placed into the homogeneous region of the spectrometer. Where possible, materials with magnetic susceptibilities that differ as little as possible to the vacuum space ($\Delta\chi = 0$) are chosen to minimize homogeneity degradation (see table 3.1). This is difficult when using metals, and austenitic stainless steel types (low-temperature, non-magnetic nickel alloys) such as SS-316L and SS-321 have been chosen to minimize this effect.

Material	**Susceptibility Difference ($\Delta\chi$)**
Water	1.26×10^{-7}
Quartz	2.96×10^{-7}
Sapphire	3.70×10^{-7}
SS-316L	0.03 - 0.09
SS-321	1.75
Carbon Steel (Standard)	$\sim$100

Table 3.1: A table of some $\Delta\chi$ values (from vacuum) for materials used for this project.[100,113,115] Although the $\Delta\chi$ value for SS-321 is much higher than that of SS-316L, the latter is harder to weld when thin walled,[113] and so may not be used for some applications. The value for carbon steel is also presented to highlight the suitability of SS-316L and SS-321.

3.2.4 Insertion

A limitation not shown in the magnet schematic is that concerning the space above the spectrometer, used to insert the cryostat. With an initial clearance above the magnet of just over 1000 mm, a number of complicated cryostat designs were developed which introduced breaks in the instrument (such that it could be inserted in two parts), with flexible cryogenic and pumping lines. These designs were dismissed as too complex, and the clearance above the spectrometer was increased to just over 2000 mm by reconfiguring ventilation in the roof space and raising the ceiling. The nature of a top loading instrument also restricts pumping access on the lower part of the shaft as there can be no protrusions, such as vacuum flanges, from the cryostat. This restriction can be overcome by designing peripheral hardware that fixes onto the bottom of the VTI after it has been loaded.

3.3 Vacuum Pumping

High throughput pumps are used to prepare the VTI for use, flow helium through the instrument and facilitate Joule-Kelvin expansion at low temperatures. To avoid nitrogen or moisture freezing in the VTI during cooling, air first needs to be evacuated from the space using a vacuum pump. If this is not done, gases will condense and subsequently freeze as the instrument drops past their respective boiling and melting points. Although this may not cause an issue in some open parts of the instrument, solid formation in capillaries could result in blockages, and freezing in any small defects could cause system failure. The same pumps used to evacuate the air are then used to operate the continuous flow helium cryostat by drawing the cold fluid through the VTI. This is done at a speed such that the instrument is continuously cooling, with warming and expanding helium being removed from the system immediately.

The manner by which gas particles flow through a system when being pumped upon is a function of the system pressure, pumping hardware and mean free path of the particles.[116] Most pumps displace a fixed volume per unit time,[117] described by a pumping speed, which depends heavily on the pressure of the system being evacuated.[118] If the mean free path of the gas is significantly lower than the overall system dimensions the flow is considered viscous. Conversely, if the path is larger than the system dimensions the flow is considered molecular, in which collisions with the system walls occur more frequently than those with each other. An intermediate flow regime exists between these two flow types in which a mixture of viscous and molecular flow is exhibited. A system exhibiting viscous flow can be pumped on easier than that exhibiting molecular flow.[119]

A pumping line is used to connect the vacuum pump to the system to be evacuated, as fixing the pump directly to the vacuum space is often implausible. As a result of wall friction within these lines, an associated flow resistance will reduce the pumping ability of the system.[120] An effective pumping speed for the pump can be described in terms of the resistance of any pumping lines and the pumping speed at the inlet of the pump,[119] and this will always be decreased by the nature of the connecting pumping lines. While viscous flow can be pumped on relatively easily, the ability to pump on a gas exhibiting molecular flow is independent of pressure and depends more on wall collisions. This means that it is important to keep the diameter of the pumping line large, and the length short, in order to pump on low pressure vacuum systems.[120] To ease the fact that the available cross-sectional area with which to pump is reduced by the NMR hardware and magnet bore, pumping is available from the top and bottom of the cryostat.

For this particular project a large roots pump (RUVAC WAU 501, Leybold Oerliken, UK) is used with a nominal throughput of 505 m^3/h to achieve high throughput pumping. This pump is initially roughed using a 70 m^3/h pump (DUO 65M, Pfeiffer, Germany) until the pressure in the system reaches less than 40 mbar. The pumps are connected in series, with an output that returns the thermally spent helium to the University liquefaction service. To reduce acoustic noise, and because they cannot be kept close to the spectrometer because of the high magnetic field strength, the pumps are located outside and connected to the system using a 6 meter pumping line with an inner diameter of 75 mm. A smaller pump may be connected to the OVC of the VTI if continuous pumping on this space is needed.

3.4 The VTI Design

3.4.1 Cooling Strategy

As a result of the arguements in section 3.1.3, a continuous flow, wet cryostat was chosen for this TJ-DNP experiment. This design uses a helium Dewar and a high throughput pump to draw helium through the sample environment, cooling it in the process. The VTI design for this experiment also introduces a small reservoir of helium between the continuous flow inlet and the sample space, called the 4 K pot, ensuring that a constantly replenished supply of liquid helium is available nearer the sample space, reducing the effective distance between the sample and the cryogenic helium and improving the cooling power of the instrument. To achieve the most efficient helium flow into this reservoir, the helium feed is protected by a vacuum jacket and a counterflow of cold helium gas[121] (shown in figure 3.3).

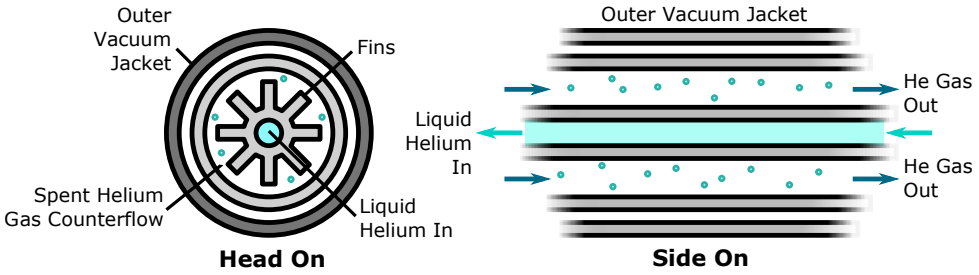

Figure 3.3: A schematic to show a counterflow helium line.[101] Fins may be added to increase the surface area over which the line is precooled.

This design requires a number of additional features in order to reach sub-helium temperatures. A number of strategies to reach temperatures below 4.22 K have been introduced in section 3.1.2, including evaporative cooling above the surface of a bath of helium and cooling via Joule-Kelvin expansion. The first of these strategies is unsuitable for directly cooling the sample used in this experiment, as it would require the sample to be

submerged in liquid helium, making rapid heating more difficult. Despite this, evaporative cooling can be implimented by pumping on the helium reservoir in the 4 K pot. It is this pumping that forms the counterflow of the helium feed. Cooling via Joule-Kelvin expansion can, however, be implimented using a high-throughput pump and by introducing a controllable, high-impedence pathway bewteen the 4 K pot and the sample space. This is realized in this TJ-DNP experiment by connecting the 4 K pot to the sample space using two capillaries controlled using needle valves. An additional heat exchanger, built using a mass of copper with an interdigitated internal structure (see figure 3.4), introduces further impedence to the pathway, ensures the helium remains cool as it is drawn to the sample and allows an easily controllable, constant stream of helium to be produced. The helium then expands from an axially symmetric annulus of fine holes onto the sample. It should also be noted that any helium sprayed onto the surface of the sample in the highly evacuated sample chamber will further be evaporatively cooled. These cooling strategies have been isolated in figure 3.4, which is a heavily simplified diagram of the VTI.

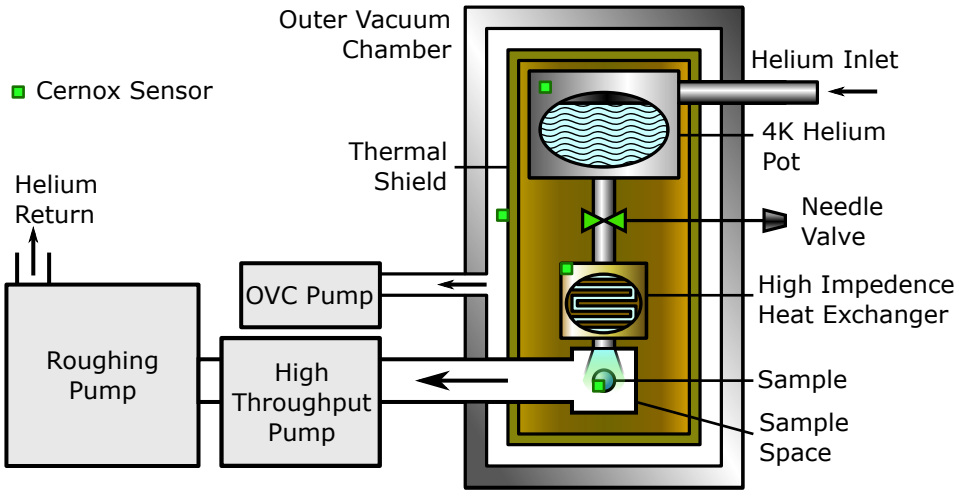

Figure 3.4: A schematic to show a simplified cryostat design which may be proposed to form the foundations of the rest of the TJ-DNP experiment.

3.4.2 Thermometry

To monitor the temperatures inside the cryostat a number of cryogenic temperature sensors are implemented (Cernox CCS, Lakeshore, US). These small sensors allow accurate temperature readings at values down to around 1 K, without introducing a large heat load to the system under test. The current applied to obtain a measurement using these devices is small to avoid heating effects, and calibration is performed to ensure that any heat that is generated and dissipated to the surroundings during read out is corrected for. These sensors are used to monitor the sample space, internal 4 K helium pot, heat exchanger and vacuum chamber radiation shield, fixed in place using a thermal paste to increase thermal contact, as shown in figure 3.5 (except at the sample space, where it is fixed using cryogenic tape). The locations of all sensors are highlighted in both figure 3.4 and 3.7.

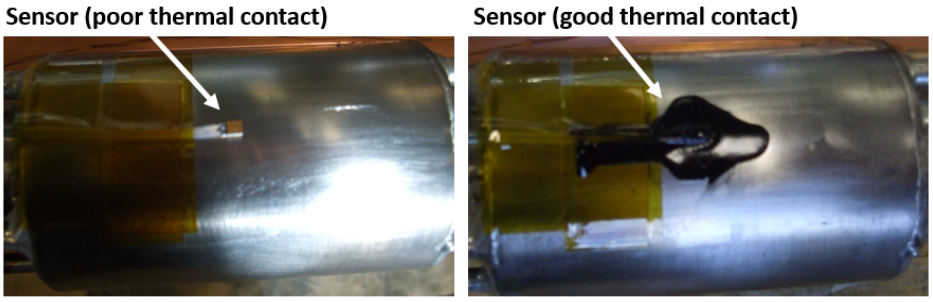

Figure 3.5: An image to show the Cernox temperature sensor adhered to the internal heat exchanger on the VTI using thermal paste.

These sensors give an indication of sample temperature and provide important information that allows both effective control and diagnostics of the instrument during operation. It should be noted that a fifth sensor was fitted to the outer radiation shield of the VTI, but was later removed and reassigned as the temperature reading did not change dramatically during the cooldown.

3.4.3 The Dummy Probe and Waveguide

A dummy probe and dummy microwave insert were built to initially test the VTI, as work on the NMR probe and microwave insert had not yet been completed during initial testing and the cooldown procedures needed to be realistic. This dummy hardware had to match the characteristics of the real NMR probe and microwave guide as closely as possible, built from similar materials of similar dimensions. The dummy waveguide was made out of a hollow copper tube 1000 mm long with an inner radius of 14 mm and an outer radius of 16 mm. A bespoke T-junction, shown in figure 3.6, was required to couple the waveguide to the non-standard connections of the VTI and allow pumping access.

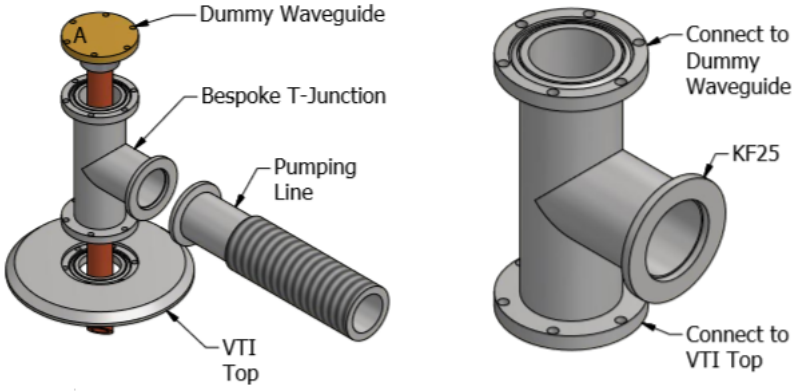

Figure 3.6: A CAD representation showing the custom T-junction which was used to insert the dummy waveguide into the VTI while also allowing pumping.

The dummy NMR probe was made from a stainless steel tube 850 mm in length, of outer diameter 8 mm and inner diameter 6 mm. This tube was fixed in the center of a KF40 blanking plate and fed through a 4-way KF40 vacuum connector which allowed both high throughput pumping and thermometry using a Fischer connector and a Cernox sensor at the tip of the shaft. Triangular baffles, just shy of the 25 mm internal diameter of the VTI, were fixed periodically along the length of the shaft to keep it centralized but not restrict pumping.

3.4.4 Bespoke VTI

An annotated schematic (figure 3.7) of the VTI can now be presented, alongside an adapted technical drawing (figure 3.8) and photograph (figure 3.9), to clearly show both the inner workings and critical dimensions of the instrument. The positionings of the ports at the top of the VTI are such that the instrument avoids the cryogenic feeds at the top of the NMR spectrometer.

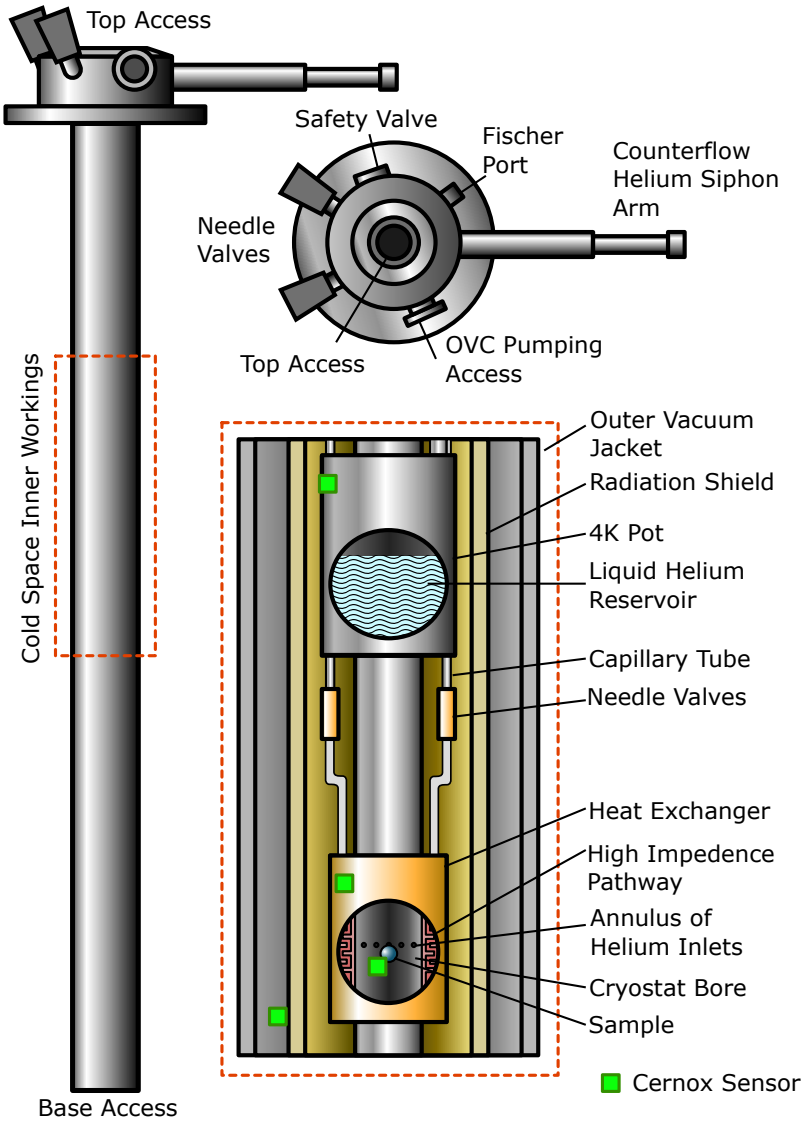

Figure 3.7: A schematic diagram of the VTI. The helium inlet annulus is higher than the sample plane as pumping from the base draws cold helium downward, a factor that was observed experimentally during testing stages. This schematic does not feature any dimensions, as these are included in the adapted technical drawing.

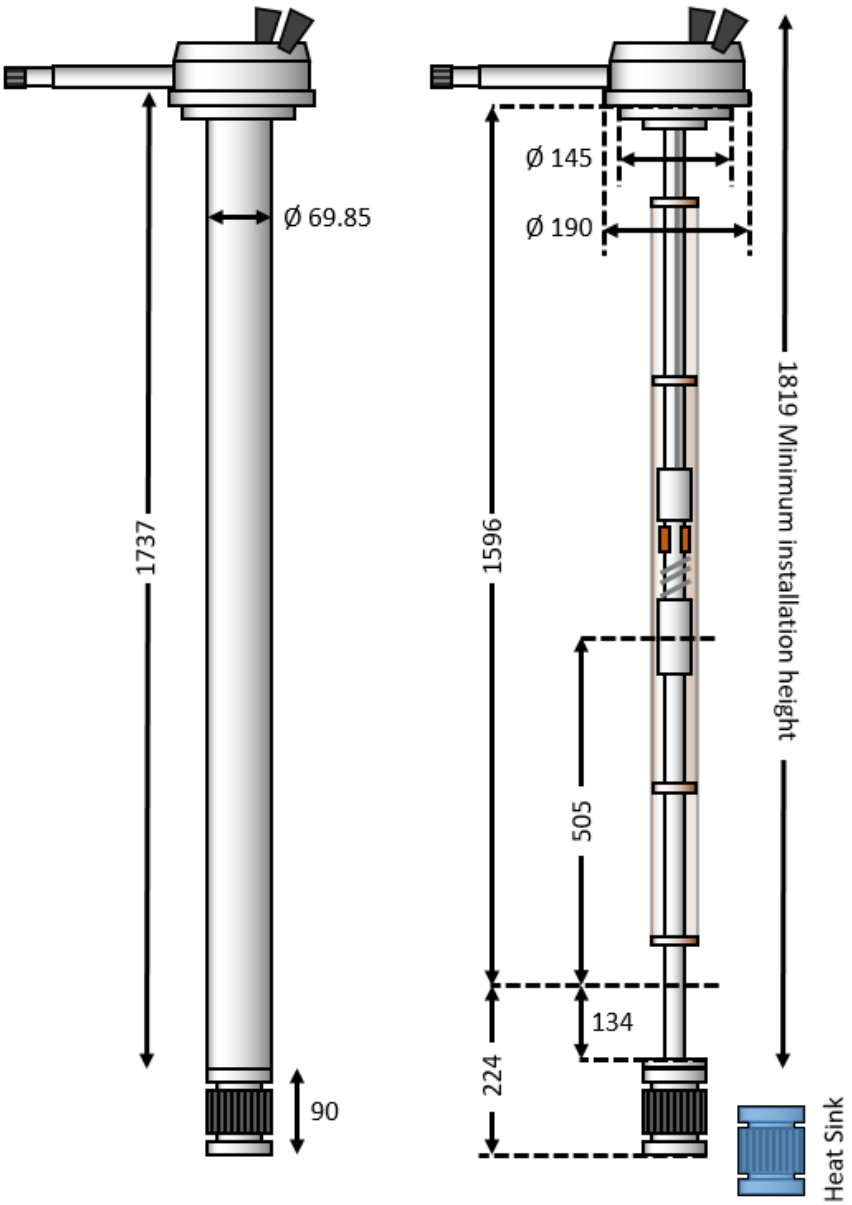

Figure 3.8: An adapted technical drawing of the VTI, showing key dimensions in millimeters. The drawing is not to scale.

The adapted drawing in figure 3.8 shows the minimum installation height to be 1819 mm. A heat sink is shown at the base of the instrument, despite being peripheral to the VTI, which is described in more detail in chapter 5 as it is designed to protect the NMR probe from cryogenic damage. The radiation shields have been hidden in the figure so as to allow the inner workings to be visible, but the four mounts can be seen along the length of the instrument upon which these are fixed.

The outer casing of the VTI could be removed to expose the inner workings of the instrument, as shown in figure 3.9. This image shows the central cooling shaft against a backdrop created by half of the inner radiation shield. Although this inner shield was removed during operation, due to the belief that it was contacting the 4 K pot and disabling the instrument (hence why there are also PTFE windings between the two to thermally insulate them - this is described further in section 3.7), an outer radiaition shield remained in place surrounding the cold space. The helium feed can be seen to enter the 4 K pot, where liquid helium is able to collect prior to being pulled through a capillary and heat exchanger system and onto the sample via manipulation of a pair of needle valves.

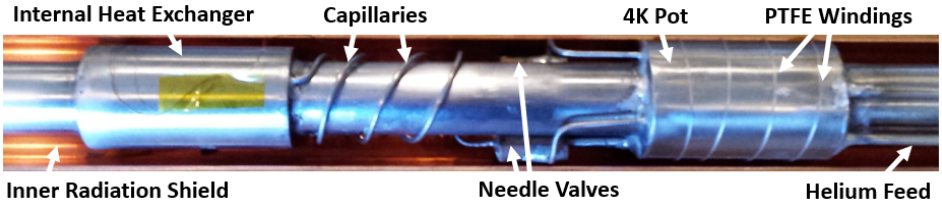

Figure 3.9: An image to show the inner workings of the cryogenic space of the VTI. Any temperature sensors are attached on the opposite side of the hardware shown.

3.5 VTI Positioning

Although the VTI dimensions were designed to match the NMR spectrometer, such that the sample was situated in the homogeneous region of the magnetic field, the practical design includes a removable collar at the top of the instrument to allow fine adjustment of this distance. This allowed any mismatch between the instruments to be corrected using a cheap, peripheral solution, rather than the instrument requiring serious adjustment. The correct VTI height within the spectrometer bore was investigated using NMR of distilled water. The strength of the axial z-gradient was changed, causing the NMR peak of water to shift if the sample was not in the center of the gradient (figure 3.10).

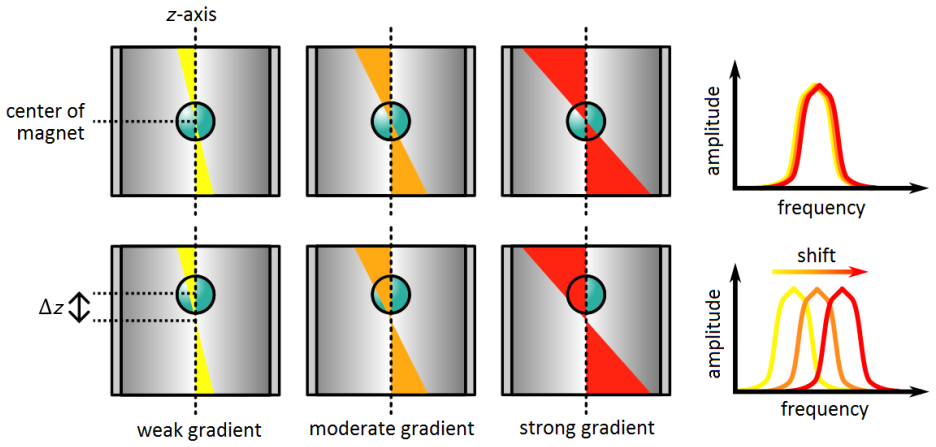

Figure 3.10: Applying a gradient along the z-axis results in a frequency shift of the NMR signal if the sample is not centred, due to the asymmetric spin response. Using this effect allows the vertical position of the sample to be checked.

Incremental steps in the VTI height were tested, showing that the frequency shift was minimal (and the sample was in the homogeneous region of the magnetic field) was when the VTI was rasied 28 mm higher in the bore (see figure 3.11). These investigations were performed at ambient temperature, with calculations performed in section 3.2.1 indicating that the sample height would remain relatively invariant of any change in temperature as the VTI sample temperature decreases towards 1 K.

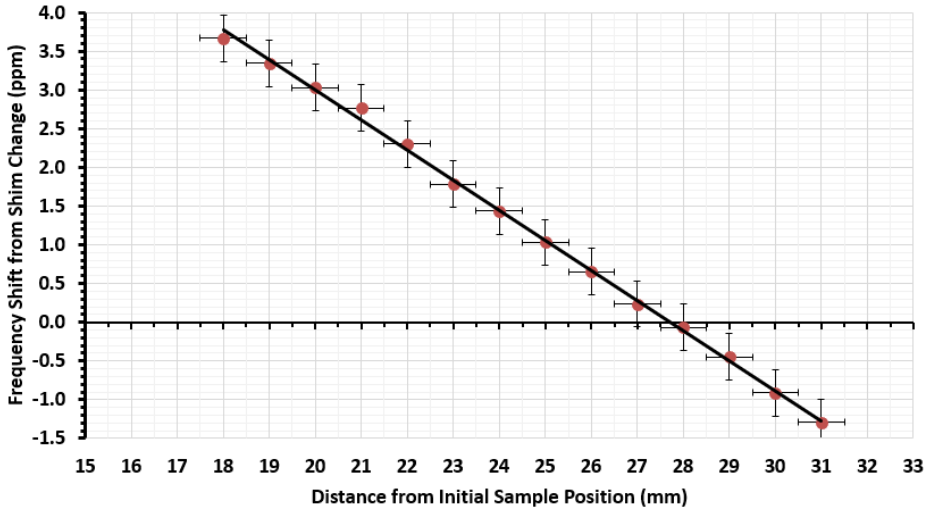

Figure 3.11: A plot to show the extent by which the NMR signal shifted when the z-shim was changed by a constant value. The error in frequency shift accounts for the width of the NMR line and that in distance is a standard measuring error.

A collar with a fixed height of 28 mm was designed and built to fit around the VTI (figure 3.12), keeping it at the correct height and allowing reproducible and accurate sample loading at room temperature.

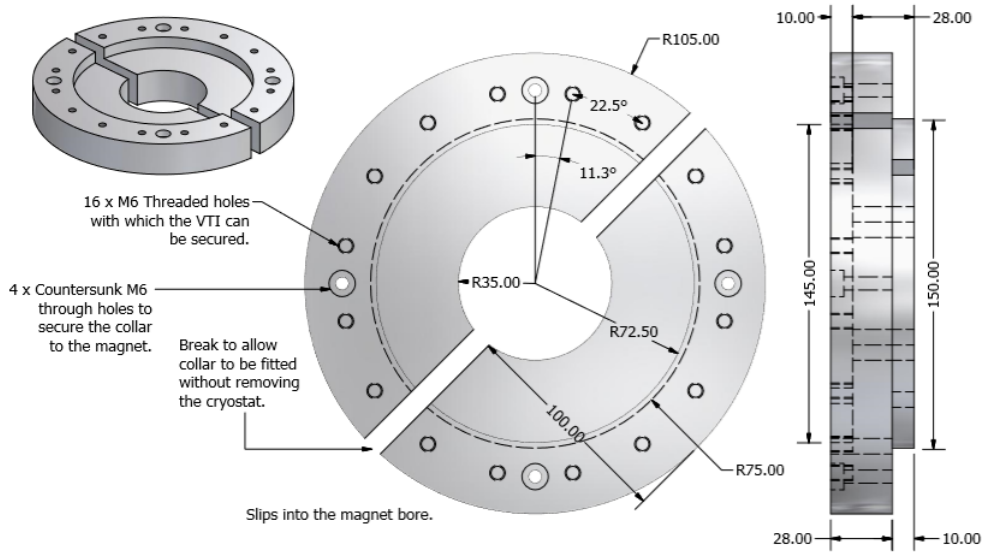

Figure 3.12: A CAD representation of the spacer designed to artificially raise the sample with respect to the static magnetic field by lifting the VTI up by 28 mm within the spectrometer bore.

3.6 Microwave Delivery

The microwave bridge described in section 2.2.3 was designed to deliver circularly polarized microwaves to the top of the NMR spectrometer used in this project, and is only part of the microwave hardware required to succesfully deliver the radiation to the sample for DNP. To ensure that the microwaves are able to efficiently continue the journey to the sample contained within the VTI, the microwave bridge has to be carefully aligned with the top of a waveguide inserted into the instrument.

The Waveguide

A stand-alone, 1 m long metallic waveguide is used inside the VTI to transmit the microwaves with as little loss as possible, featuring a tapered end which couples the radiation effectively into the sample.[96,122] This waveguide was made by Thomas Keating Ltd., has an inner radius of 12 mm (overmoding the waveguide, as this value is considerably greater than the wavelength of microwaves) and features characteristic corrugations down the entire inner length, specified in figure 3.13.[92] This reduces standing waves and eddy currents in the surface of the metal,[123] decreasing ohmic losses and improving tranmission.[124]

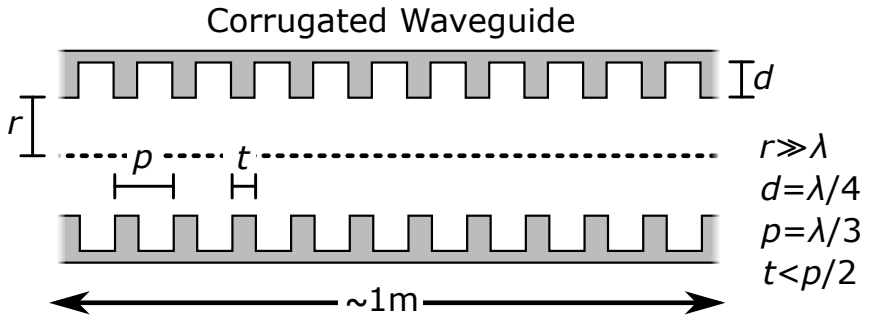

Figure 3.13: A cross-sectional schematic of the corrugated waveguide, featuring characteristic dimensions for efficient microwave transmission.

Furthermore, the propigating Gaussian mode (HE_{11}) may be thought of as a superposition of the transverse electric and magnetic modes (TE_{11} and TM_{11} respectively) propigating together. These travel at different speeds in a smooth waveguide, distorting the radiation profile and hindering microwave irradiation.[96,125]

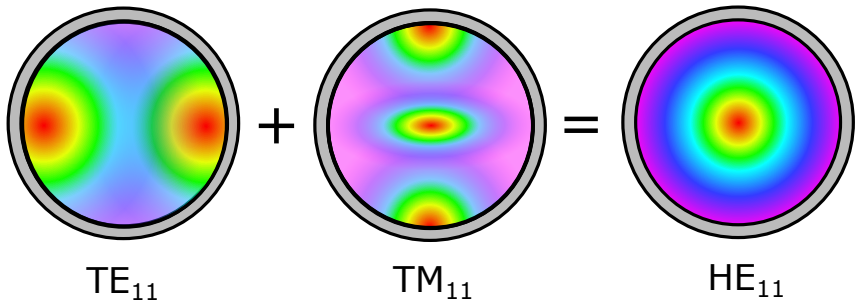

Figure 3.14: A schematic to show the superposition of the transverse electric (TE_{11}) and transverse magnetic (TM_{11}) modes to create a propagating Gaussian mode (HE_{11}).

The waveguide features a TPX^{TM} window at the top, exhibiting low loss in the millimeter regime,[126] to form a hermetic seal. To measure transmission loss through the waveguide, and because the hardware could not be tested *ex situ*, a small roof mirror was required at the end of the waveguide to reflect the radiation back out of the VTI and overcome the fact that a power meter could not be placed at the sample location. This roof mirror was designed at Nottingham to clamp onto the end of the waveguide and the power meter was used to measure the power of the reflected microwaves, with any additional measured loss associated with the inclusion of the waveguide. It is necessary to note that the raw value for this loss should be at least twice the true value, as the radiation travels along the waveguide twice (transmission and reflection). These investigations allowed a further loss of 1.18 $\pm$ 0.02 dB to be associated with microwave delivery along the corrugated waveguide.

Microwave Table Alignment

To support the microwave bridge above the magnet a precision aluminium support was built in-house. This system allows the table to slide freely into place during an experiment, at which point it may be fixed using a clamp, and be moved out of the way otherwise. A set of adjustable nuts (one at each corner), supporting the microwave bridge on its sliding mount, were used to adjust the angle and vertical position of the table. A spirit level was used to keep the bridge horizontal, while the nuts were adjusted in turn such that the center of the curved mirror face directing the microwaves downwards was 250 mm above the TPX^{TM} entry window of the waveguide. This ensured entry to the waveguide at the middle of the microwave beam waist.

Once at the correct height, lateral positioning of the microwave bridge was performed using a bespoke roof mirror, again designed at Nottingham, placed at the top of the waveguide. This reflected microwaves back from the top of the spectrometer and into a power meter monitoring the reflection arm of the microwave bridge (see figure 2.18 and 2.19). Iterative adjustments to micrometers controlling the position of the bridge in both the x and y-axis were made until a maximum power of reflection was measured, indicating that the microwaves were perfectly incident in the center of the roof mirror and all incident radiation was reflected back along the microwave path. This stage was completed with help from Kevin Pike of Thomas Keating Ltd., and once the optimum microwave table position was identified the micrometers were locked in place.

3.7 The Cooldown

Full testing of the VTI took about 6 months, with a number of leaks during the early stages of validation slowing progress. The leaks were identified by a loss in OVC vacuum integrity as the inner space of the instrument began to reach low temperatures, followed by a subsequent raise in this temperature as the expanding helium in the OVC caused thermal bridging. Visual inspection, mass spectrometry and partition testing were all employed to locate the leakages, one-by-one, and have them sent off for repair. Because the leaks were only apparent at low temperature it was not possible to locate them all with certainty at once.

Initial Testing

Initial testing was performed at Thomas Keating Ltd. prior to shipping, using the limited equipment available there. These tests used the dummy NMR probe as the real probe had not been built. This consisted of a hollow steel tube with a temperature sensor on the end where the sample would sit and involved a rudimentary cooldown procedure by which the helium Dewar was pumped on through the instrument. These tests, results of which are shown in figure 3.15, showed that the VTI was capable of reaching temperatures down to $\sim$40 K after a period of 5 hours if left under these conditions. A repeat experiment was performed to ensure the same results were obtained, reaching the same base temperature after 4 hours. Noting this plateau, an external pressure was applied to the helium Dewar, forcing more cryogenic helium to enter the instrument. This reduced the minimum temperature to $\sim$10 K, at which point it was decided that testing should continue in Nottingham, where both the pumping power could be increased and the sensing equipment was more advanced.

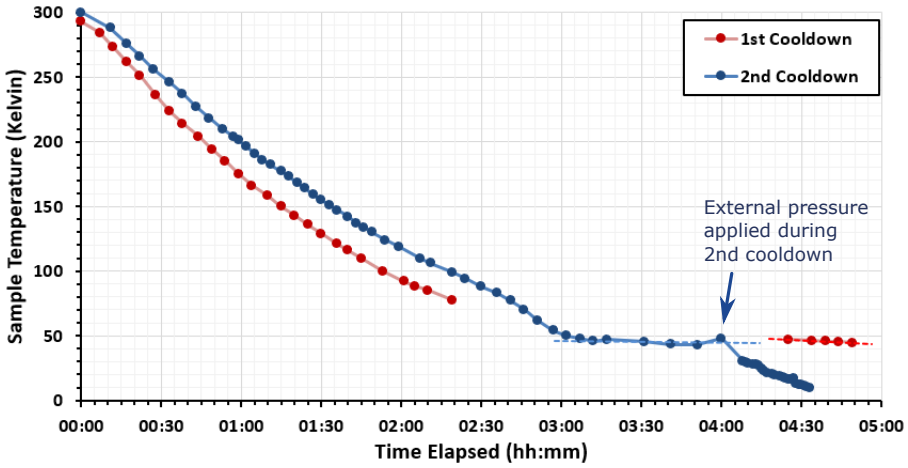

Figure 3.15: Initial testing of the cryostat at Thomas Keating Ltd. using a small pump to draw cold helium through the instrument. Both experiments show a similar base temperature plateau of ∼40 K, indicated using a dotted line and believed to be higher than expected due to peripheral hardware limitations. The point at which external pressure was applied during the 2nd cooldown is indicated.

Experimental Procedure

The cryostat was transported to Nottingham University and testing was continued. Again, this used the dummy probe and sample sensor, but the equipment at the university meant that a clearer idea of the temperatures and pressures inside the instrument was available. These early cooldowns yielded differing results, depending on the procedure used to control the instrument. For example the first test comfortably reached a temperature of ∼10 K, but took 9 hours to do so, and subsequent runs only reached ∼ 40 K with no signs of further decrease, albeit in shorter times. These drastic differences were a result of inexperience with the novel instrument, and as the cooldowns continued certain actions were linked to internal VTI behaviour and an optimal cooling procedure was converged upon. The method allowing the lowest base temperatures to be realized in the shortest time was when the entire instrument was opened (all needle valves, etc.) and an initial blow through with cold helium gas from the Dewar chilled the inner space. The effects of this can be seen in figure 3.16. The pressure within the sample chamber was monitored and

kept at ∼40 mbar, ensuring cool helium gas was spent within the sample environment before extraction. As the VTI cooled and the pressure dropped, action was taken to counter the change. It may also be noted that, once the inner space began to drop significantly in temperature, cryopumping caused the pressure in the OVC to drop.

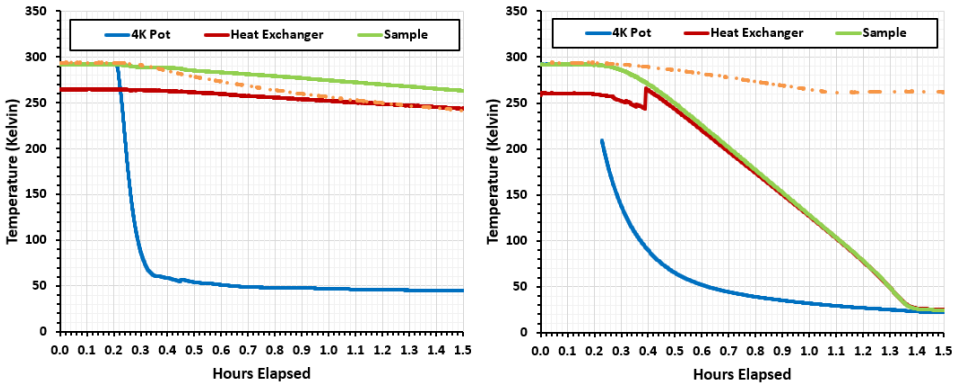

Figure 3.16: A comparison of two initial cooldowns, one with the needle valves closed to begin (*left*) and the other with them open (*right*). Although the cooling time of the 4 K pot is shorter when the valves are closed (as the helium remains in the pot for longer) the overall base temperature achieved achieved is higher. The dotted orange line indicates the temperature of the radiation shield.

Once the inner space was cooled and liquid helium began to form in the internal 4 K pot the needle valves could be closed and the VTI used in Joule-Kelvin mode. This stage was difficult to control, requiring practise to respond suitably to slight changes in the sample environment using the valves that govern the inflow of helium. Fluctuations in temperature were caused by improper response, shown in figure 3.17, with the helium pot filling (a) and the needle valve being opened (b). If the valve was not carefully opened it would deplete the reservoir, cooling the sample rapidly but only briefly. The cooling then stops (as helium is depleted) and the temperature increases again as the pot fills. In this case the needle valves must be closed (c) and the 4 K pot allowed to replenish. Care must then be taken to match the emptying of the pot, caused by opening the needle valves, with filling.

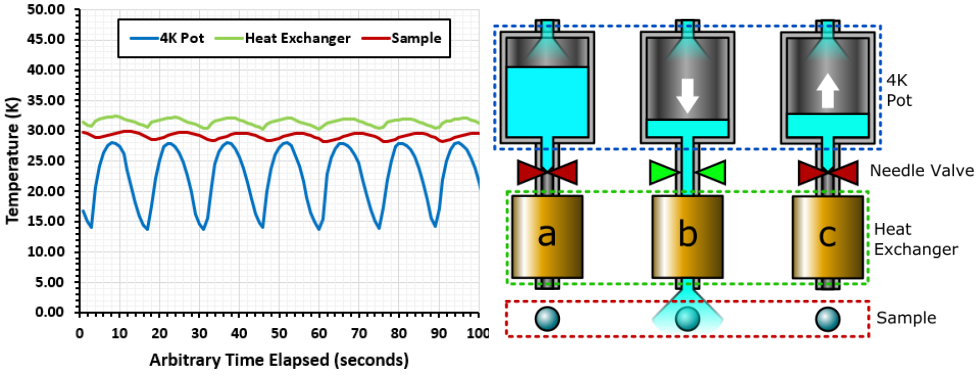

Figure 3.17: A plot (*left*) to show how the core temperature could fluctuate within the cryostat with poor control of the needle valves. The mechanism for this fluctuation (*right*) is explained in the text.

VTI Modification

The function of the VTI itself was also improved by inspecting the inner workings. For example, it was noted was that the helium inlets, delivering liquid helium to the 4 K internal pot, were in thermal contact with the bulk of the instrument. This was causing the cooldowns to take a longer time and a PTFE spacer was built to insulate the inlet (see figure 3.18) which immediately reduced cooldown times by ∼60%.

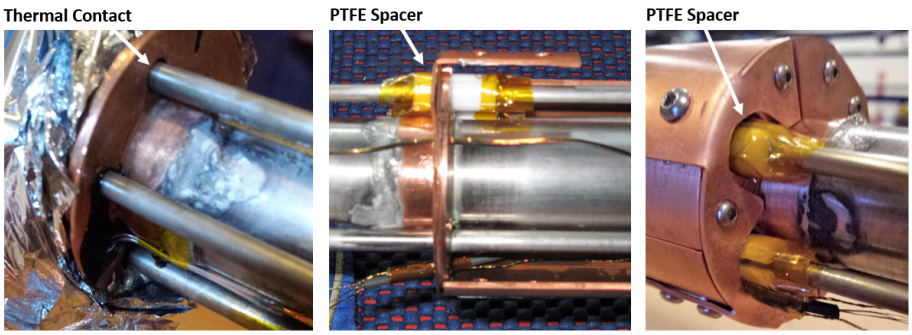

Figure 3.18: An image to show the helium feed in thermal contact with the radiation shield support (*left*) which was causing slower cooldowns than expected. This was improved by introducing a PTFE jacket around the helium feed (*centre* and *right*).

Further to this, the inner radiation shield was seen to loosely touch the outside of the 4 K pot. Initial efforts to wrap the 4 K pot in PTFE wire had no discernable effect, and so the inner radiation shield was removed completely, along with the superinsulation in the vacuum space

(figure 3.19). The cooldown was repeated, including the outer radiation shield for protection against radiative heating, this time reaching a single digit base temperature in 2 hours.

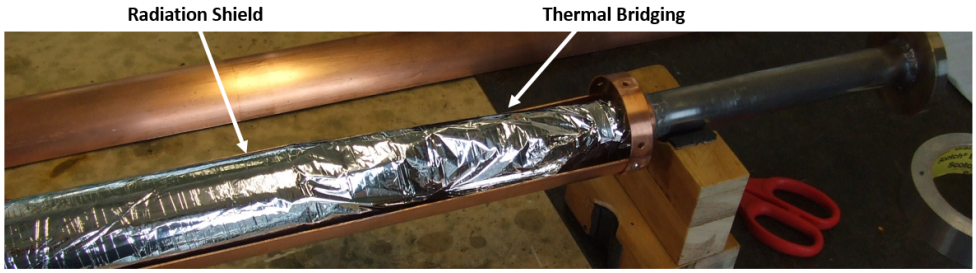

Figure 3.19: An image to show the Mylar superinsulation causing thermal bridging between the inner workings of the VTI and the outer radiation shield.

Dummy Probe Cooldown

Following VTI modification and development of the cooldown procedure, a temperature of ∼2 K was achieved in 2.5 hours using the dummy probe (figure 3.20). No attempt was made to hold this temperature stable, but rather it was used as a benchmark to allow the project to progress using the real, bespoke NMR probe (detailed in Chapter 5).

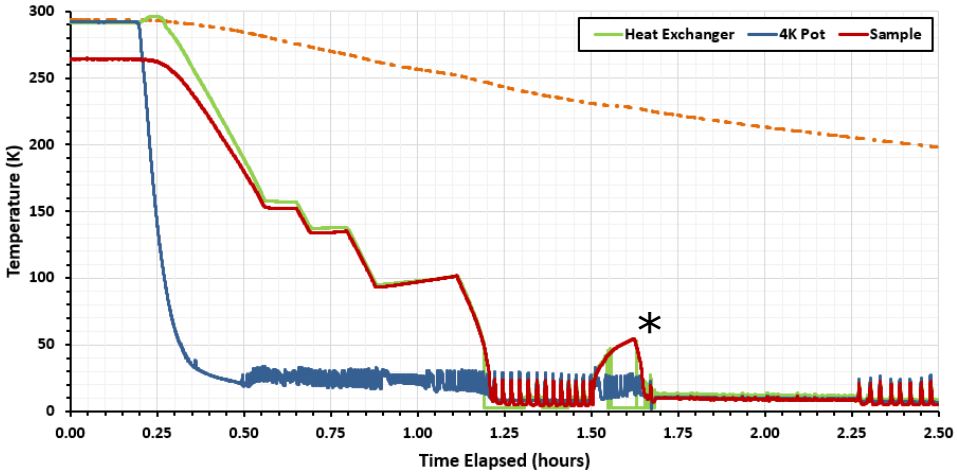

Figure 3.20: A cooldown to show success of the VTI using a dummy probe. The '*' shows control to overcome fluctuations in core temperature, which started up again later on. A base temperature of ∼1.9 K was achieved at the end of this cooldown, measured using a multimeter due to readout complications at the lowest values. The outer radiation shield (dashed orange line) is still cooling at the end of the experiment.

Cryoleaks

At this point it was noted that the primary cooldown stage was unable to drop below ∼50 K, frosting was seen on the helium feed of the VTI and vacuum integrity in the OVC was lost. These indicators suggested a leak, possibly caused as the instrument reached the lower temperatures using the dummy probe. Cryogenic leaks through any micro-cracks and pits in welded joints would have been further damaged as the cold helium expanded into the vacuum space of the OVC (a visible example is shown in figure 3.21). These leaks were found using helium gas and mass spectrometry, before the VTI was marked and sent for repairs. This process was repeated a couple of times, as the cryogenic nature of the leaks made them both difficult to fix and validate. Eventually the instrument was able to reach the low temperatures previously obtained without showing evidence of leaking and the cooldowns could continue.

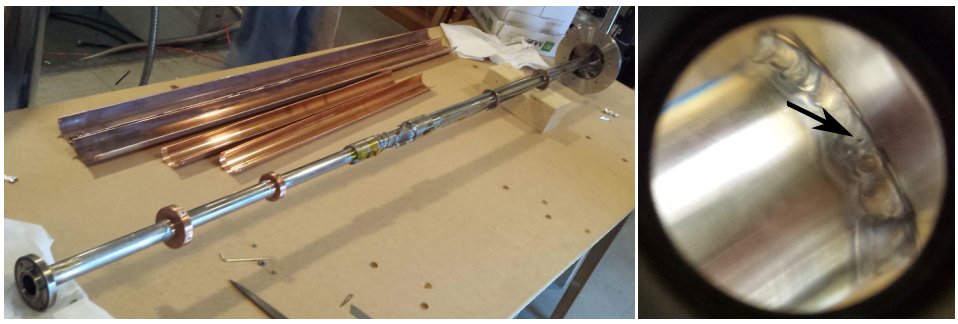

Figure 3.21: An example of a small leak found by filling the VTI bore with helium gas and using a mass spectrometer to detect where it was escaping along the shaft.

Final Performance

Once all cryogenic leaks were fxed the variable temperature insert was shown to reach a base temperature of ∼1.75 K in under 2.5 hours, and was subsequently held steady for a period of 15 minutes. Figure 3.22 shows the cooldown in which this base temperature was achieved.

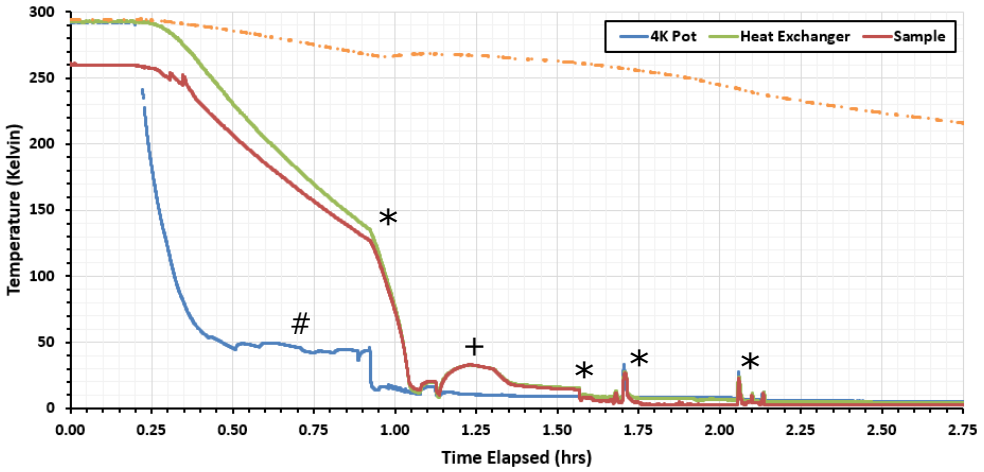

Figure 3.22: An example cooldown in which a stable base temperature of ~1.75 K was achieved after 2.5 hours. The pressure in the bore was kept stable at 40 mbar over '#', after which helium purges were used to increase and then decrease the helium in the bore (*). At '+' the needle valves were closed, showing a raise in heat exchanger and sample temperature but a steady 4K pot reading, as expected.

It may be noted that the temperature readings bottom out at 2.55 K due to the limiting range of a readout box that was used with them, and to measure the lowest temperatures a multimeter and manual calibration with a curve was used. This cooldown was repeated, to ensure that the conditions were reproducible, and a base temperature of 1.76 ± 0.02 K was recorded for longer than 10 minutes (see figure 3.23).

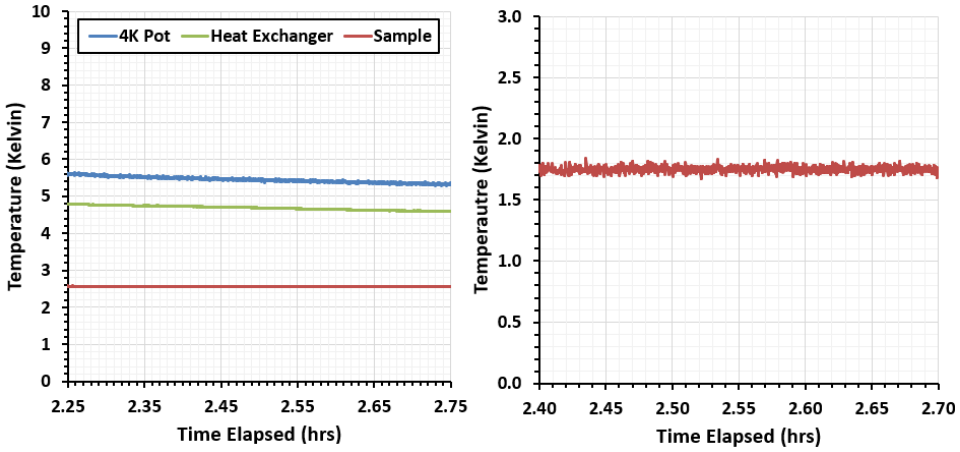

Figure 3.23: Two figures to show the lowest, stable temperature achieved using the cryostat. The figure on the *left* shows the raw temperature traces, with that on the *right* showing the calibrated sample temperature.

Chapter 4

Rapid Heating

Following sufficient transfer of electron polarization to the nuclei of interest at low temperture using the microwave system describd in section 2.2.3, a rapid temperature rise is required to bring the sample to ambient temperature for NMR spectroscopy. This temperature rise needs to be rapid, so as to preserve as much nuclear polarization as possible, and must not destroy the sample.

4.1 Heat Required

4.1.1 Melting

It is possible to calculate the amount of heat energy required to bring about a temperature rise in the sample using equation 4.1.1.1. The amount of heat energy, Q, required to bring about a change in temperature ΔT is dependent on the specific heat capacity C_{p} and mass m of the sample.

$$Q = mC_{\mathrm{p}}\Delta T \tag{4.1.1.1}$$

If the sample experiences a phase change, an additional quantity of heat will be required to account for this. To melt the frozen sample

considered in this project, a term for the latent heat of fusion, L_{F}, needs to be included, which describes the heat required to bring the sample from solid to liquid state, without a raise in temperature. It should also be noted that the specific heat capacity C_{p} is dependent on temperature.[100] This means that, when simulating the energy required to bring about a change in temperature for a realistic sample, it is necessary to evaluate the heat required to bring about temperature changes in different regimes separately, as the specific heat values of water and ice differ substantially. For the purposes of the TJ-DNP experiment in Nottingham, equation 4.1.1.1 can be written in the form of equation 4.1.1.2.

$$Q_{\mathrm{total}} = (mC_{\mathrm{pI}}(\Delta T_{\mathrm{I}})) + (L_{\mathrm{F}}m) + (mC_{\mathrm{pW}}(\Delta T_{\mathrm{W}})) \qquad (4.1.1.2)$$

Here, C_{pI} and C_{pW} are the average isobaric heat capacities of ice and water from ∼20 K to 273.15 K and 273.15 K to 300 K respectively[100] (with $\Delta T_{\mathrm{I}} = 273.15 - 1$ and $\Delta T_{\mathrm{W}} = 300 - 273.15$) and take the values $C_{\mathrm{pI}} = 1.28$ kJ/kgK and $C_{\mathrm{pW}} = 4.19$ kJ/kgK. This choice of C_{pI} is assumed fair as there is a linear dependance between C_{p} and temperature once the water freezes. The mass of the sample will depend on the volume, with initial calculations using a sample of the dimensions defined in section 2.2.1 (a cylinder of height 4 mm and base radius 4 mm). Making the assumption that 1 litre of water has a mass of 1 kg, the heat required to bring a sample of pure water from 1 K to 300 K, undergoing a phase change as it does so, can be estimated around 50 J.

In reality, 40:60 water-glycerol will make up the majority of the sample, and will be used during simulations as a dummy system. Although the inclusion of glycerol to water introduces a glass-phase transition at

low temperature, this transition does not require an associated enthalpy of change, as the molecular movement inside the mixture simply becomes frozen. This stated, confirmational changes in the ensemble mean that the heat capacity is drastically reduced below this transition.[127] Despite these changes in heat capacity, the thermal behaviour of the mixture has been shown to behave similarly to that of a pure water sample.[128]

The compound specific heat of a homogeneous mixture of n materials has been experimentally found[129] to follow equation 4.1.1.3.

$$\langle C_{\mathrm{p}} \rangle_{\mathrm{Mix}} = \sum_{m=1}^{n} \langle C_{\mathrm{p}} \rangle_m X_m \tag{4.1.1.3}$$

Where a material m with an average heat capacity $\langle C_{\mathrm{p}} \rangle_m$ is weighted by its concentration within the mixture, X_m. Values for the density and specific heat capacity of glycerol across the limits of equation 4.1.1.2 were found such that the mixture could be evaluated[100,130] to give the heat required to bring the compound mixture from 1 K to 300 K. The sample mass was amended so as to account for substituting 60% of the water with glycerol. These calculations confirm that a similar amount of heat energy, ∼45 J, is required to bring the mixed 40:60 water-glycerol sample from 1 K to 300 K. This amount of energy can be delivered using a 30 W laser, if delivery is perfect, in 1.5 seconds.

4.1.2 Heat Sinks

Although an amount of heat energy required to heat the sample has been estimated, heat sinks will exist that will redistribute this heat energy to the sample surroundings that must also be considered. The nature of the VTI detailed in Chapter 3 means that the primary heat sinks in the

system will be caused by heating of the sapphire sample holder by the heated sample and radiative heating from surfaces within the vacuum space. Heat sinks through the hardware supporting the sample in place will be neglected, as the sample cup will be assumed to be thermally isolated from the probe shaft.

The heat energy required to bring the sapphire sample cup (section 4.4.4) from ∼1 K to room temperature can be calculated using equation 4.1.1.1. This energy will be provided by the sample itself, rather than the laser, as the cup is mid-IR transparent, and the thermally conductive properties of the sapphire[100] ensure heat diffusion through the sapphire occurs on the same time scale as sample heating. This was calculated to be ∼22 J, and is of the same order as the energy required to heat the sample. Furthermore, once hot the sample will radiate into the surrounding cryostat via equation 3.2.2.3. Although there is a large temperature difference between the sample and the surrounding walls of the VTI during the rapid heating stage of the experiment, the small surface area of the sample means that, using an emissivity for water of 0.98,[100] the heat flow from the sample via radiation can be calculated as 0.03 W. This value is far smaller than the any heat supplied by the laser and can be neglected.

These considerations mean that, for a sample under the conditions prescribed by this TJ-DNP experiment, additional heat energy is needed to warm up the sample container. This energy can be added to that required to heat the sample alone to give an overall energy requirement of ∼70 J. Using a 30 W laser the sample and cup can be brought to ambient temperature in just over 2300 ms (2.3 seconds).

4.1.3 Limitations

This experiment requires a large amount of heat energy to be delivered to the sample during the heating stage of the cycle, and the delivery will be as localized as possible to ensure the process is rapid. Although a high amount of energy may need to be delivered to the sample in a short amount of time to achieve this, care must be taken to ensure it is not destroyed.

As described in section 3.2.1, an increase of temperature in a material usually brings about an increase in dimension. Although the sample used for this experiment will not significantly change in volume over the TJ-DNP temperature range, due to both its small volume and small coefficient of cubical expansion $\beta = 3\alpha$, localized small-scale expansion may still cause problems. Significant heating from one side of the sample while the other remains comparatively cool, as will be proposed, may induce thermal cleavage, an effect by which macro- or micro-fractures manifest from local volume changes.[131] Although this may help to melt the sample overall, this effect may also reduce conduction through the sample and damage surrounding hardware.

Similarly, extreme heating of one side of a trapped solid may deposit heat energy into the sample such that melting and subsequent vaporization occur on one side before the energy can diffuse through the medium. This generation of an expanding gas below a frozen mass, and continued absorbtion of radiation by the vapour, could cause the sample to dislodge from the sample container and NMR coils and stop the TJ-DNP experiment.

4.2 Heating Methods

A number of heating mechanisms exist which could deliver the energy calculated in section 4.1 in the desired time, and the modular nature of the hardware, along with the modification capability of the NMR probe, allow these all to be considered and introduced more easily. This project primarily explores the ability to heat the sample using the interaction of certain nanoparticles with visible light (section 4.3) or a high powered, mid-infrared laser (section 4.4), however a number of additional heating methods warrant mention, as they could help the rapid temperature jump. These mechanism should not destroy the sample, should perform the temperature jump in a short period of time and should allow swift cooldown of the VTI after heating for experimental recycling.

Hot Gas

Hot helium gas could be introduced into the sample space, temporarily flooding the environment and bringing the entire space to a higher equilibrium temperature, resulting in a rapid temperature increase of the sample. The gas could easily be introduced via small diameter gas lines which would be closed during the cool down stages of the experiment and opened when required. The heat introduced using this mechanism could be increased by using gas of a higher temperature, although helium should always be used as it can be easily pumped out and will cause no freezing problems when the system is cooled again. This heating is similar to that used in a dissolution DNP experiment, except the use of gas avoids dilution and allows sample recycling. Although this method of heating seems promising, the hot gas would not locally heat the sample and would cause a considerable rise in temperature throughout the VTI, reducing the temperature cycling capability of the instrument.

Microwave Irradiation

Although molecular rotational modes in the sample into which microwaves couple energy are frozen out at the lower temperature range of this experiment,[132] this already available energy source could be used as the jump progresses to speed up the heating process. Section 1.3.5 mentions work using microwaves to bring about considerable temperature jumps using dielectric heating[63] and, although the temperature range for this work ($T_{\mathrm{DNP}} = 20$ K) is not as large as that proposed in this project, it demonstrates the use of microwaves as a possible additional heating mechanism during the latter stages of this temperature raise.

Resistive Heating

Passing a current I through an element with a resistance $R(T)$ causes Joule heating with a heating power P calculated using equation 4.2.0.1.

$$P \propto I^2 R(T) \tag{4.2.0.1}$$

This method of heating could be easily implemented by introducing a length of wire to the sample space through which a high current could be passed. Having said this, the temperature dependance of the resistance of regular electrical conductors causes their resistance to decrease with temperature,[101] meaning this method of heating becomes more difficult at the low temperatures associated with the TJ-DNP experiment. To overcome this, cryogenic heaters are available, made out of materials with high resistance at low temperature, such as Nichrome™, Constantan™ and Manganin™.[133] The applicability of this heating method relies on the elements not interfering with the NMR electronics or introducing field inhomogeneity that degrades the resolution of the NMR spectra.

4.3 Nanoparticle Heating

4.3.1 Plasmonics

Localized Surface Plasmon Resonance (LSPR) arises due to the electromagnetic interaction of light and matter when the wavelength of the incoming radiation is comparable to the physical dimensions of a metallic medium. Incident electromagnetic radiation causes deformation of the free electron environment within the metal which will establish a coherent, propagating charge density if the incident photons couple to the natural oscillation of the electron cloud. On a large, flat metallic surface this surface plasmon polariton manifests as a plane travelling wave (figure 4.1, *left*). If however the physical dimensions of the metallic medium are of the same order as the wavelength of the incoming radiation, as may be found for nanoparticles or structured surfaces, the resonance is confined to the surface conduction electrons of the metal and manifests as a localized standing wave (figure 4.1, *right*) which generates heat. This occurs in the visible range of the electromagnetic spectrum for gold and silver nanoparticles, with a spectral response that can be tuned by manipulating a number of physical parameters, allowing heat to be coupled directly to such a system using a specific visible frequency of light.

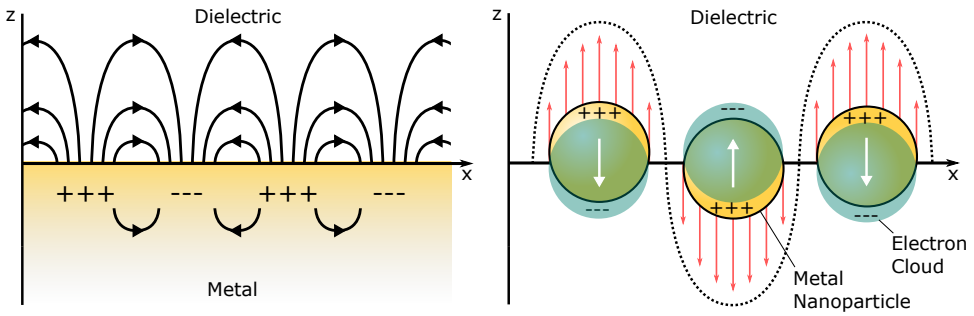

Figure 4.1: Schematic diagrams illustrating the propagation of a surface plasmon polariton (*left*) along a large, metallic surface and the standing wave induced in an ensemble of nanoparticles by localized surface plasmon resonance (*right*) [134].

The exact spectral response of the nanoparticles depend on a number of physical parameters,[134] such as the particle radius a, morphology of the nanoparticles (expressed using a shape factor χ which is equal to 2 for a sphere) and material from which they are made. Their dielectric environment also effects their response, making nanoparticles that exhibit LSPR good candidates for a number of sensing applications.[135]

$$\mathrm{Ext}(\lambda) = \frac{24\pi^2 N a \varepsilon_0^{3/2}}{\lambda \ln(10)} \left[\frac{\varepsilon_\mathrm{i}(\lambda)}{(\varepsilon_\mathrm{r}(\lambda) + \chi\varepsilon_0)^2 + \varepsilon_\mathrm{i}(\lambda)^2} \right], \qquad (4.3.1.1)$$

where ε_r and ε_i are the real and imaginary parts of the nanoparticle dielectric function and N corresponds to the number of nanoparticles in the solution.

Nanoparticles of different shapes have different spectral responses, with spheres exhibiting sharp, material characteristic resonances, tetrahedrons having more broadband responses and nanobars displaying a characteristic heating frequency as a function of particle length.[136] A great range of nanoparticle morphologies are available, each offering slightly different optical behaviour.[137] Nanoparticles may also be synthesized and attached to various biologically relevant molecules for biosensing purposes.[135] These functionalized molecules could be included in the DNP sample to increase plasmonic effects and provide sample information. Whether heating is provided by a nanoparticle suspension held within the sample or a nanoparticle layer on the surface of the sample cup, it is possible to turn nanoparticle ensembles, when irradiated with light of the correct frequency, into efficient nanoheaters.[138,139] This would require an optical path into the sample space through which visible frequencies of light could pass.

4.3.2 Nanoparticle NMR

Introducing metallic nanoparticles to an NMR sample creates magnetic susceptibility mismatches at the metal-sample boundaries. As described in section 3.2.3, this will lead to unwanted magnetic field gradients which decrease magnetic field homogeneity and degrade the NMR experiment. A known concentration of gold nanoparticles (10^{16} particles ml^{-1}, as this is the upper limit of nanoparticles per volume before aggregation of the particles prohibit the LSPR effect) of varying sizes (5 nm, 12 nm and 30 nm in diameter, all with good optical response) were suspended in water to investigate how their inclusion impacted the relaxation characteristics of the sample.

Using pure water as a control, an inversion recovery experiment was performed to investigate T_1 relaxation and a spin echo experiment was performed to investigate T_2 relaxation. The inversion recovery experiment varies a time delay τ_d between initial magnetization (M_0) and NMR acquisition (see figure 4.2) in which the magnitude of the magnetization vector $M_{(\tau_d)}$ decreases through spin-lattice relaxation, allowing a value for T_1 to be extracted[140] using the equation 4.3.2.1.

$$M_{(\tau_d)} = M_0 \left(1 - 2\exp\left(\frac{\tau_d}{T_1}\right)\right) \tag{4.3.2.1}$$

T_2 relaxation was simply investigated by observing the reduction in the magnetization $M_{(t)}$ as a train of spin echoes was collected,[140] with the magnetization decreasing from a value of M_0 as the time t increased due to spin-spin relaxation mechanisms.

$$M_{(t)} = M_0 \exp\left(\frac{-t}{T_2}\right) \tag{4.3.2.2}$$

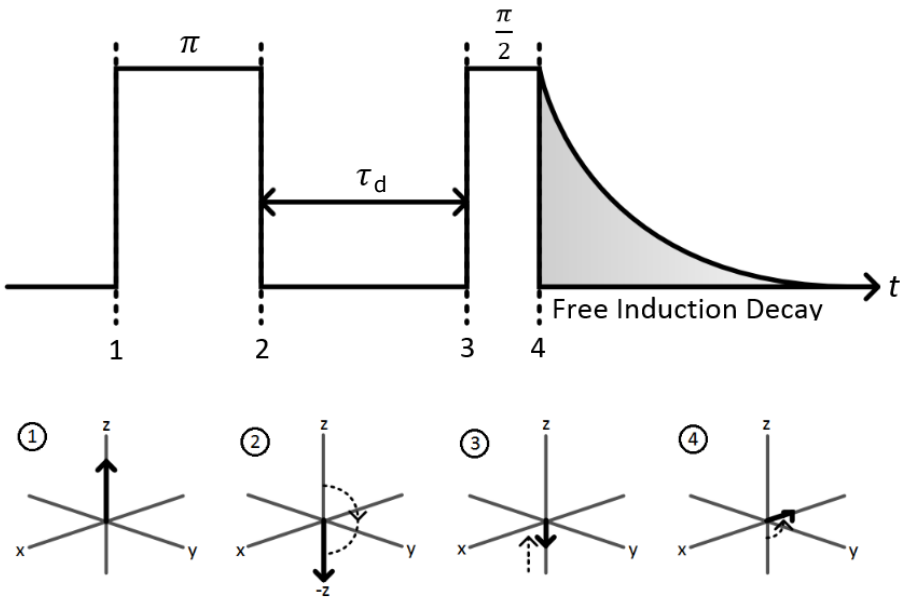

Figure 4.2: An illustration of the inversion recovery experiment. A π pulse is applied to invert the spins (2) and a time period τ_d is allowed to elapse, reducing the magnitude of the magnetization vector through spin-lattice relaxation (3). A $\pi/2$ pulse is then applied which brings the spins into the x-y recording plane (4) and the remaining magnitude can be measured.

Experimentally speaking, the magnetization of the samples was imaged and represented using a grey-scale pixel value, with lighter pixels representing regions of higher magnetization (figure 4.3). Regions of pixels were then assigned to different nanoparticle samples and MATLAB was used to calculate magnetization values using the average grey-scale value for each sample tube.

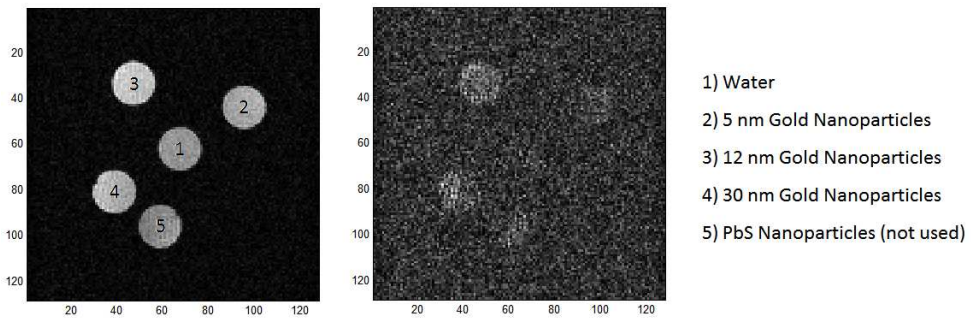

Figure 4.3: An NMR image of the spin magnetization within the sample space, indicated by pixel brightness. The image to the left was taken before relaxation mechanisms were allowed to drastically reduce the magnetization, while the image on the right shows the decreased magnetization after 1.5 seconds. The axes simply indicate spatial co-ordinates.

The results from the inversion recovery experiment, shown in figure 4.4, indicate that the inclusion of the nanoparticles at concentrations of 10^{16} particles ml^{-1} does not drastically alter spin-lattice relaxation. The T_1 value for water was calculated from this data at around 1175 ms, while that of the nanoparticles ranged from 1172 to 1177 ms (all data presented in a summary table 4.1).

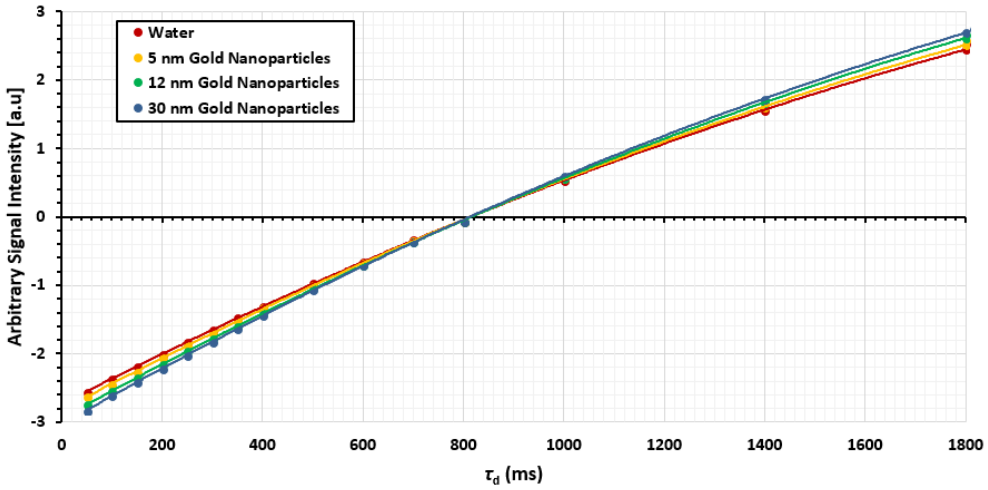

Figure 4.4: Experimental results from the inversion recovery experiment.

To investigate the effects of the nanoparticles on the spin-spin relaxation of the sample, equation 4.3.2.2 can be written in the linear form of equation 4.3.2.3, allowing T_2 to be extracted from the gradient of a straight line graph, shown in figure 4.5.

$$\log\left(\frac{M_{(t)}}{M_0}\right) = t\left(\frac{1}{-T_2}\right) + c \qquad (4.3.2.3)$$

This method to calculate T_2 was only useful for the first 15 data points, as the SNR of the results decrease drastically as the echo train subsides, and this is translated as a large error in the processed data. This was used to calculate a T_2 value for water of 594 ms and show that the inclusion of nanoparticles altered this value by a maximum of 100 ms (see table 4.1).

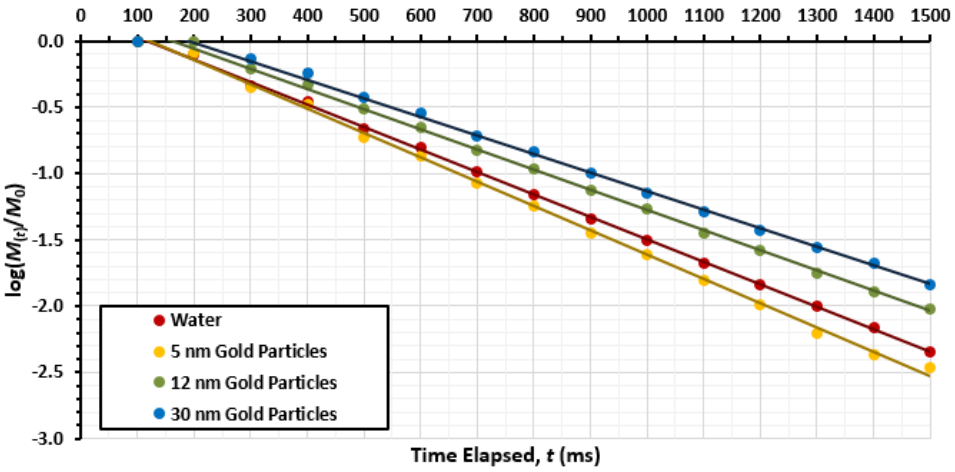

Figure 4.5: The linear data from the spin echo experiment.

From these experiments, the changes in T_1 and T_2 relaxation brought about by the inclusion of gold nanoparticles was measured to be small, with the relaxation constants for pure water similar to all three experimentally tested solutions. These are summarized in table 4.1.

Channel	$\boldsymbol{T_1}$ **(ms)**	$\boldsymbol{T_2}$ **(ms)**
Water	1175 ± 8	594 ± 7
5 nm Nanoparticles	1174 ± 8	546 ± 6
12 nm Nanoparticles	1177 ± 9	648 ± 6
30 nm Nanoparticles	1172 ± 8	694 ± 7

Table 4.1: A table to summarize the relaxation constants measured for a selection of nanoparticle solutions and compare them against water.

This suggests that any susceptibility mismatches introduced by the nanoparticles would not sufficiently alter the TJ-DNP NMR experiment. Having said this, there is still concern for using them in a DNP driven experiment as it is unknown whether the inclusion of the metal nanoparticles will affect the overall DNP effect.

4.3.3 Nanoparticle Heating

In parallel to the experiments to investigate spin relaxation effects of the nanoparticles, their usefulness as heaters was also investigated. To begin, the wavelength at which gold nanoparticles strongly absorb incident radiation was calculated using equation 4.3.1.1. Gold was chosen due to its bio-inert nature and the fact that it has a LSPR resonance falling within the visible range of the electromagnetic spectrum. Published constants were used[141] to calculate the real and imaginary components of the dielectric parameter for gold, and the extinction cross section was simulated for 30 nm nanoparticles using MATLAB (see figure 4.6), showing that visible light of wavelength ∼530 nm couples effectively to the nanoparticles and may be used to heat a sample containing them.

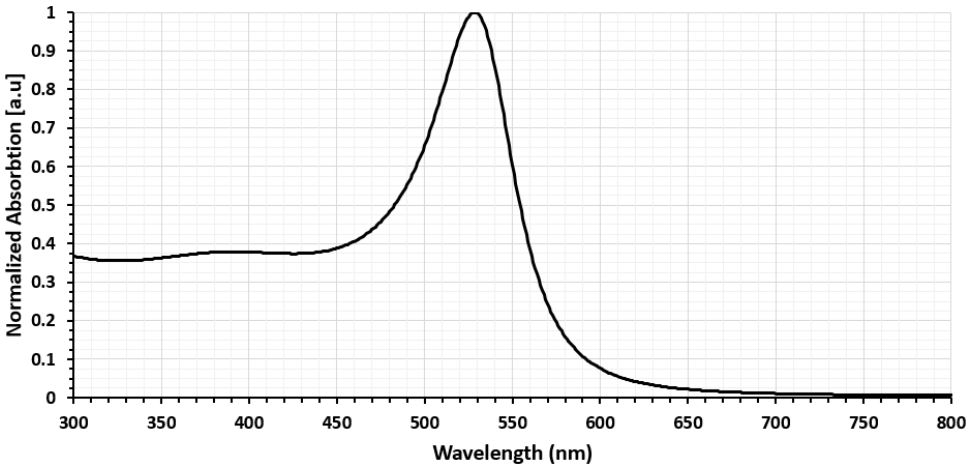

Figure 4.6: A plot of the extinction cross section, directly relating to radiation absorbed, against wavelength of incident radiation for 30 nm diameter gold nanoparticles in water.

The rate of energy supplied by a laser to a nanoparticle ensemble, Q_{nano}, can be found using equation 4.3.3.1.[138] This factors in the power of the laser, I, the absorbance of the nanoparticle solution, A_λ, and an efficiency factor, η (which is considered close to 1 for gold nanoparticles).

$$Q_{\text{nano}} = I(1 - 10^{A_\lambda})\eta \tag{4.3.3.1}$$

The absorbance A_λ can be further defined using equation 4.3.3.2,[138] where l_{opt} is the length of the optical path, C is the molar nanoparticle concentration (with an upper limit of around 10^{16} particles ml^{-1}) and $\text{Ext}(\lambda)$ is the extinction coefficient.

$$A_\lambda = \text{Ext}(\lambda) \cdot l_{\text{opt}} C \tag{4.3.3.2}$$

The value of Q_{nano} can be calculated as a function of incident laser power, using a realistic value for $A_\lambda = 0.0217$ as quoted in the literature,[138] to give an indication of the possibility of heating using gold nanoparticles in the sub-second time period desired. Using equation 4.3.3.1, it can be shown that a laser power of 1.5 W (the power of the 532 nm LSPR excitation source) would provide just over 0.07 W of heating energy, which is negligable when compared to the 67 J required to bring the sample to 300 K calculated in section 4.1. A_λ could be raised by increasing the nanoparticle concentration, but the calculations performed so far use the limit at which the nanoparticles begin to aggregate, causing degradation of the LSPR itself.

The temperature rise ΔT per second caused by the nanoparticles can be estimated using equation 4.3.3.3.

$$\Delta T = \frac{Q_{\text{nano}}}{m C_{\text{pW}}} \tag{4.3.3.3}$$

where C_{pW} is the heat capacity of the sample with mass m (using the same values as those in section 4.1). This confirms that, at just over 0.15 Ks^{-1}, any heating caused by the nanoparticles is tiny and the mechanism can be discounted as unsuitable for TJ-DNP.

4.4 Mid-IR Radiation

The primary heating mechanism chosen for this novel system is a high powered laser module, coupling energy directly into the sample via the resonance between the laser source and the fundamental vibration of the atomic bonds within the specimen. This directly manifests as vibrational energy in the target molecules,[142] which subsequently diffuses as heat through the material via interactomic collisions.

4.4.1 Laser Heating

Laser Irradiation

The wavelength of the laser for this experiment has been chosen to couple to the fundamental vibrational modes of the hydroxyl groups abundant within the sample,[143] which exhibit resonances between 3100 and 3500 cm^{-1} at ∼300 K.[144] It should be noted that these resonances are temperature dependent,[145] narrowing in absorption bandwidth and falling in vibrational frequency as the temperature lowers from ambient temperature to ∼20 K. This drop in vibrational frequency equates to ∼100 cm^{-1} which, along with the broadening at higher temperature, does not pose an immediate problem and should still allow excitation with the laser within the temperature ranges of the TJ-DNP experiment.[146]

The laser chosen for this project is a diode-pumped, Er:YAG laser module (3mikron^{TM} DPM-30, Pantec Biosolutions, Liechtenstein), which emits an over-moded Gaussian beam with a precise wavelength of 2.94 µm (3401 cm^{-1}) and a maximum average output power of ∼30 W. This maximum output is limited by the controller, with a maximum pulse length of 250 µm and repetition rate of 1000 Hz. The nature of the module also

allows lower output powers to be realized by manipulating laser pulse parameters, such as pulse frequency and length, as shown in figure 4.7. This is done using an interface on a laser control unit (LCS-30300, Pantec Biosolutions, Liechtenstein).

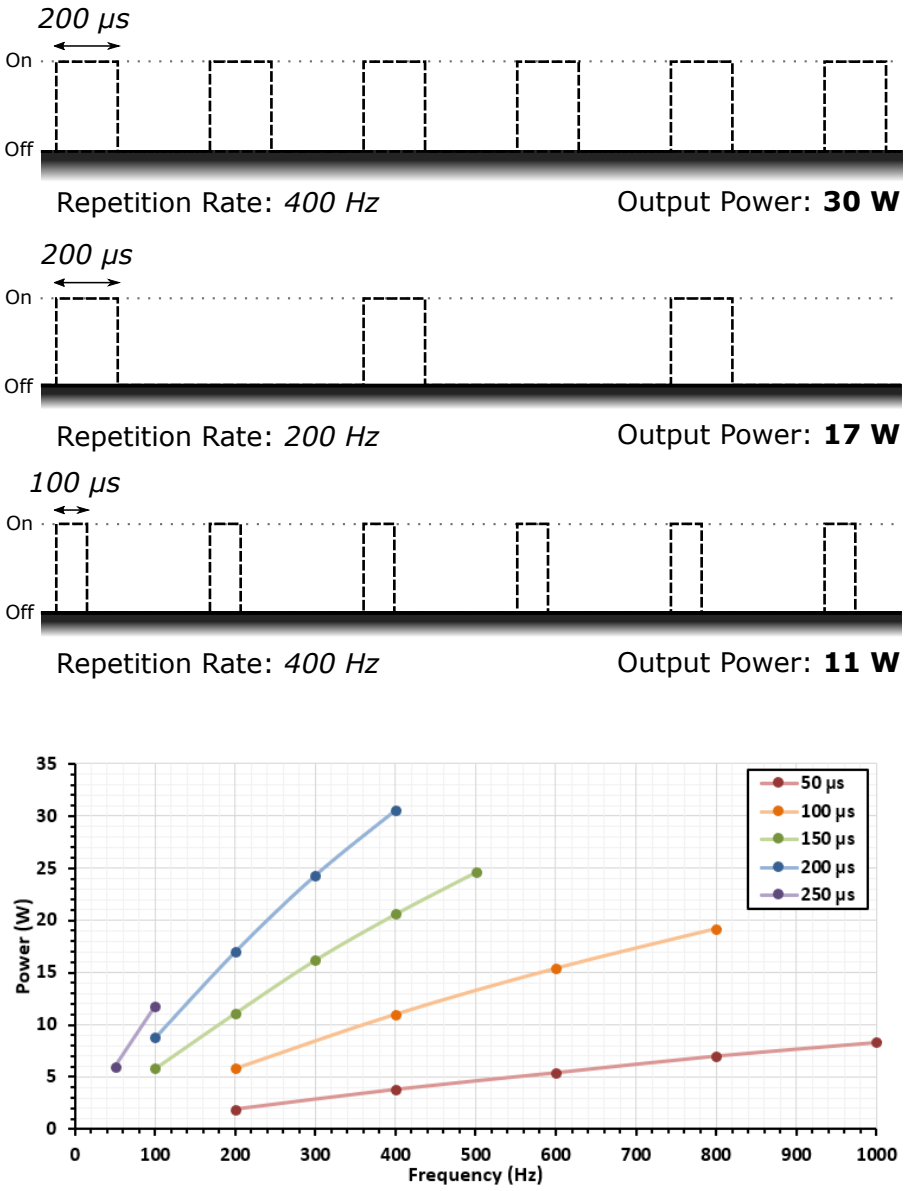

Figure 4.7: A figure to show how manipulation of the laser pulse parameters alter the power of the output radiation. It can be noted that halving the repetition rate, for example, does not half the output power. These results are obtained with a 200 A supply to the controller.

The fact that the laser output power does not scale linearly with parameters such as repetition rate and pulse length suggests that output power in not uniform accross the pulse. Doubling the pulse length from 100 µs to 200 µs, while keeping the repetition rate constant, increases the average power output by a factor of ∼3 suggesting a non-linear build up of power across the pulse (indicated in figure 4.8). Furthermore the fact that doubling the repetition rate, from 200 Hz to 400 Hz for example, increases the power output by a factor of ∼1.5 suggests that there is a non-binary switch off of the laser power and a dead time before the next pulse.

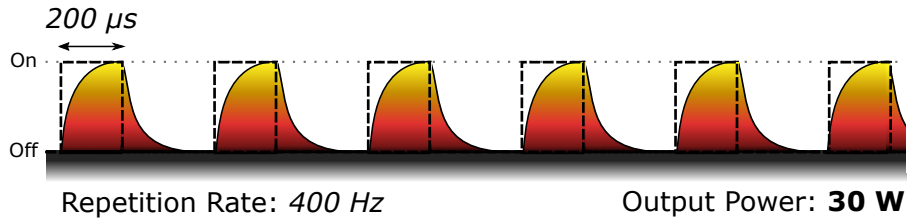

Figure 4.8: A figure to show how manipulation of the laser pulse parameters alter the power of the output radiation.

The average output power has a strong dependence on the current supplied to the laser module, which requires 200 A to realize the nominally quoted output values indicated in figure 4.7. Investigation of the output power of the laser as a function of the current supplied is presented in section 4.6, where it was noted to affect experimental results. The laser module is cooled using distilled water, circulated using a dedicated unit (P310, Termotek, Germany).

Although the laser module can be interfaced such that the output is controlled by a computer, exposure for this experiment is controlled with a gas-driven shutter (see figure 4.9) which allows the laser module to stabilize prior to exposure. The shutter uses a gas powered actuator to

move a high power beam dump in and out of the beam path. Electronic solenoid valves are not used as the system is located within the region of high magnetic field, underneath the NMR spectrometer. The speed at which this shutter functions is dependent on the gas pressure delivered to the actuator, with higher speeds resulting in a faster shutter time but more vibration through the system as the beam dump is moved. This technique allows millisecond switching of laser irradiation and a sturdy mounting system featuring foam damping strips (see section 4.5) reduce vibrations such that the NMR is not affected.

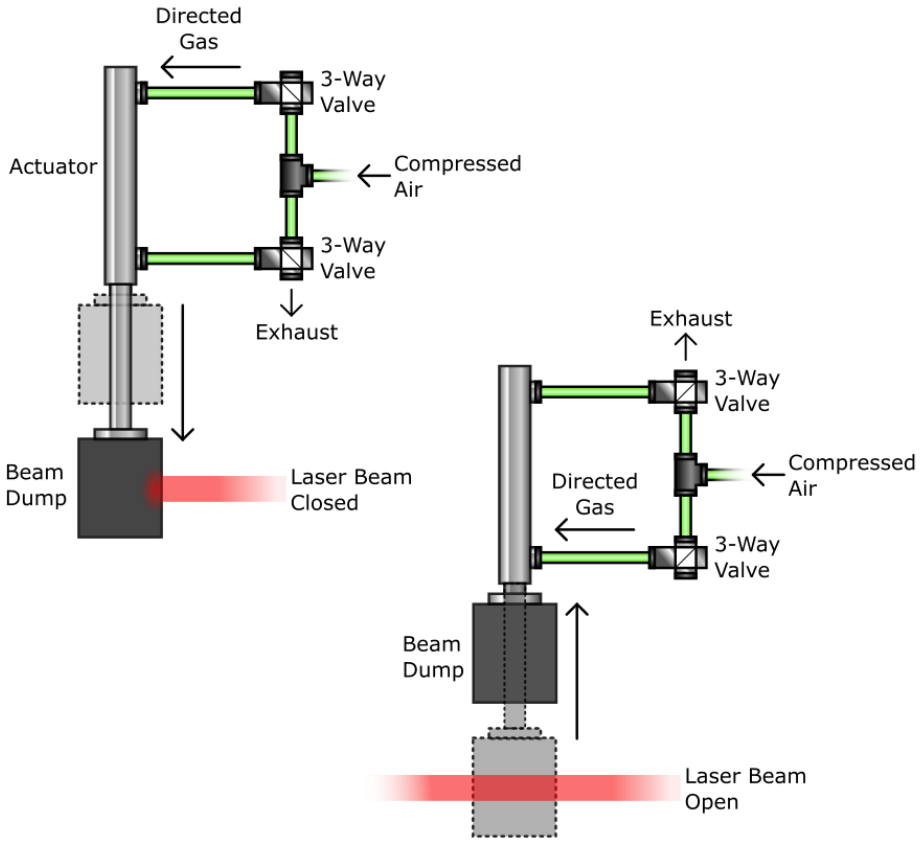

Figure 4.9: A figure detailing the function of the laser shutter system. Two 3-way valves are electronically operated in unison, conversely with one another, allowing the gas operated actuator to be driven and relieved at the same time.

Bench Top Tests

Once in possession of the laser module, a number of proof-of-principle experiments were performed on dummy samples of water to ensure that the system could heat the sample as required. As a primary investigation, small blocks of ice 20 mm in length were placed in the laser path and exposed to various powers of mid-IR radiation. The time taken for the laser to melt through the ice was recorded and used to get an idea of how fast our samples should melt. The current supplied to the laser was set to the maximum 200 A, so as not to inhibit output power, and a range of exposures from around 2 - 30 W were tested. It can be noted that, although the melt times do decrease as laser power increases, this effect begins to plateau towards the higher available powers (see figure 4.10).

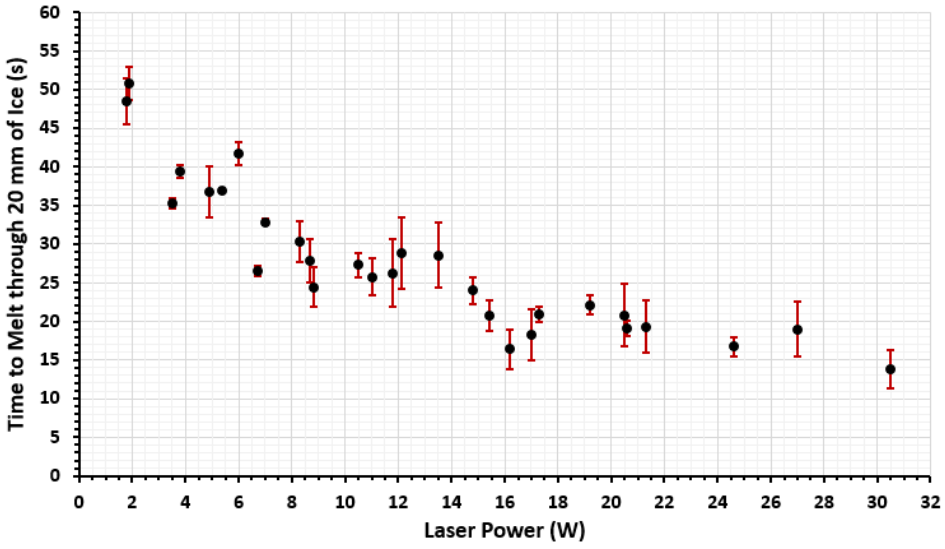

Figure 4.10: A graph to show the decrease in the time taken to melt through 20 mm of ice as the laser module output power was increased. Each data point is an average of three measurements, with the error in melting time equal to the standard deviation of these readings.

Periodic peaks and drops in the melt times can also be seen, initially thought to be due to the mixture of pulse parameters (such as pulse length and duty cycle). These paramteres were grouped to see if a pattern could be seen, but the results showed no correlation.

The plateau in melt time as the output power was increased was initially believed to be associated with heat transport through the ice as higher powers are deposited, however a number of additional observations were noted which may have an effect on the final experiment. To begin, an increase in beam diameter was seen as higher powers were delivered, perhaps as the beam quality dropped and subsequent divergence increased. This then melts a larger volume of ice, requiring more energy and subsequently taking a longer time. Another possible reason for the plateau was observed when documenting the process with a video camera, as shown in figure 4.11.

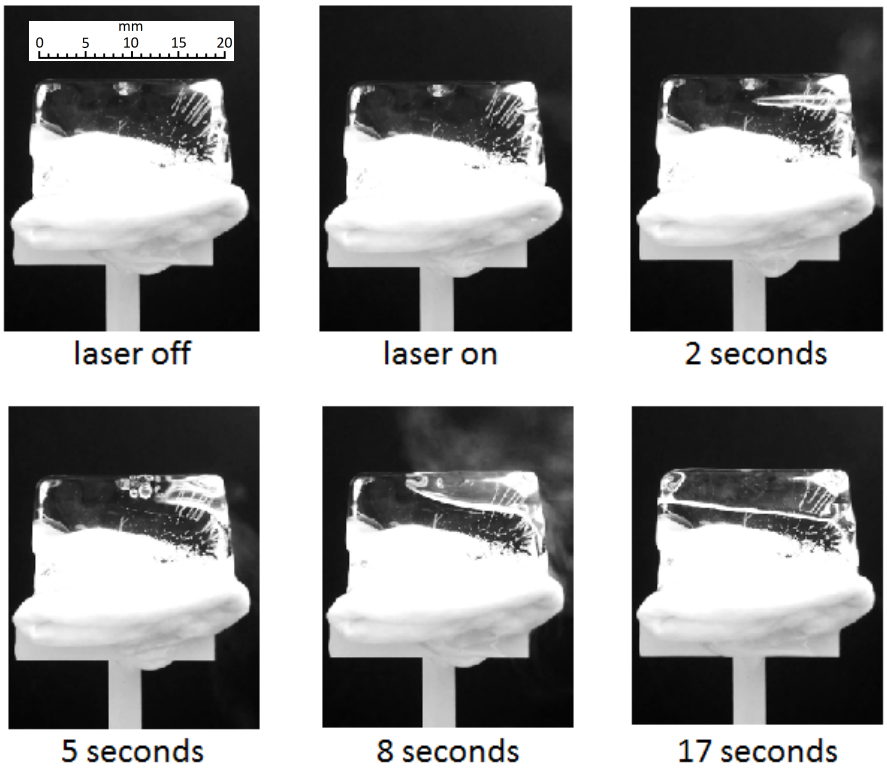

Figure 4.11: A collection of stills from an experiment in which ice was melted using a 20 W Er:YAG laser beam. The stills have been labelled with the time elapsed from initial irradiation, allowing the dynamics of the melting process to be discussed.

Although these investigations showed that the radiation has an immediate effect on the ice, boring cleanly about 10 mm into the solid after 2 seconds, this process slows at around 5 seconds. At this point bubble

formation can be noted within the tunnel, suggesting the melting process is producing liquid which is not ejecting quickly enough, absorbing the laser power and being vaporized. This prevents the solid beyond it from melting through direct laser exposure. This is further evidenced by the still taken at 8 seconds, in which a large vapour cloud can be seen to burst through the roof of the tunnel after substantial heating. After this stage the liquid is less restricted and can flow away, allowing the laser to continue melting the solid, finally boring through the specimen. This increases the overall melting time to 17 seconds, although the laser melts through half of the material in about 2 seconds. This may not be an issue in smaller specimens, such as those used for TJ-DNP.

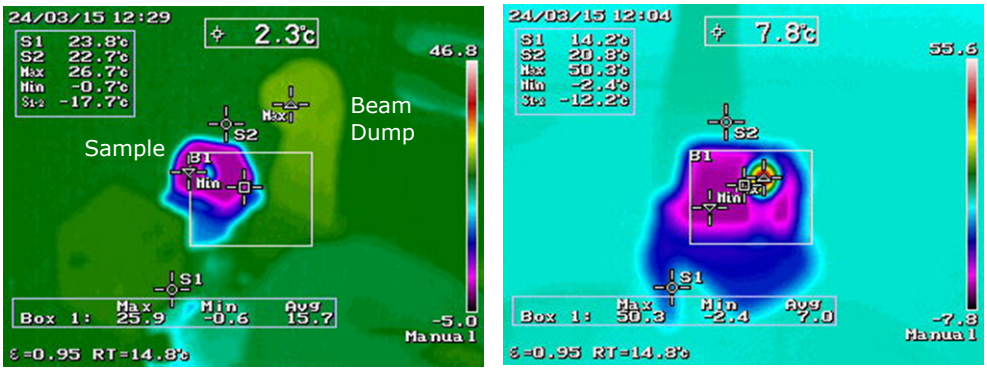

Figure 4.12: Images taken using a thermal camera during an ice boring experiment. The image on the *left* shows the set up, with an ice specimen in front of a beam dump, and the image on the *right* shows the center of the ice tunnel, as it is being bored, reaching a temperature of 50 K above melting point.

The times experimentally observed for the ice to melt were compared to the enthalpy of fusion, using the laser output power, and calculated to correspond to a requirement of over twice as much energy as theory predicts. This excess energy can be attributed to the laser heating the escaping, melted liquid, raising the temperature by 50 K in places (as shown in figure 4.12). The fact that this heated liquid was in thermal contact with the bulk ice would also include heat sink processes to the experiment, slowing it further.

To get an idea of how the laser might affect the smaller sample, the melt times were scaled down with the change in volume of the melted ice (from the cylinder with a depth of 20 mm and a diameter of ∼6 mm, bored during the bench-top tests, to the sample dimensions described in section 2.2.1). This indicated that it would take ∼1.5 seconds to melt the TJ-DNP sample (shown in figure 4.13).

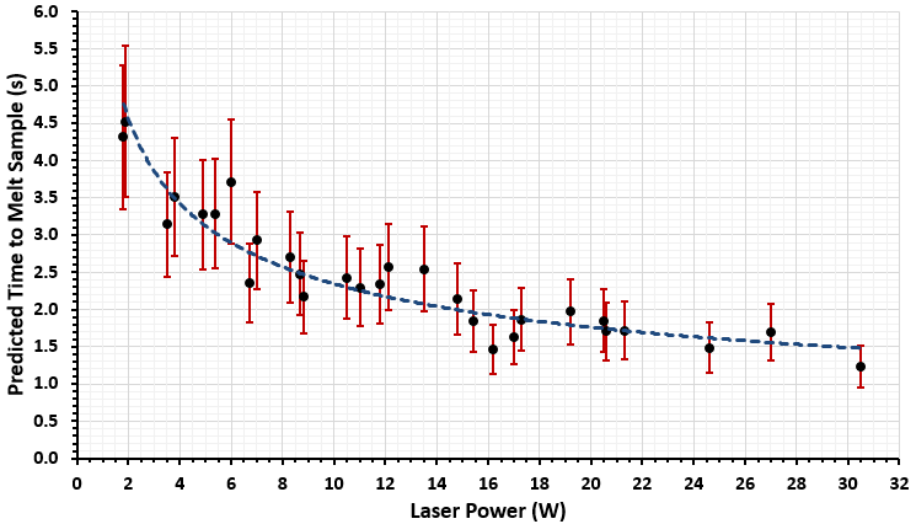

Figure 4.13: A simulation of the expected melt time for a realistic sample size, from ice at 0°C to liquid at room temperature, extrapolated from experimental data. The errors in melting time here are a propigation of the standard deviation noted in figure 4.10 combined with a number of errors due to experimental assumptions (such as the true volume of ice melted, for example).

Although this data shows a melt time under 2 seconds for the sample, this is only associated with the energy delivered to overcome the heat of fusion of the sample, rather than a rise from 1 K to 300 K. To take the investigation further, ice samples 20 mm in length were immersed in liquid nitrogen (at 77 K) prior to 27 W laser exposure. This raised the experimental melting time by 32 s ± 2 s overall, translating to a further second to melt the small TJ-DNP sample. This total melt time of ∼2.8 s to bring the sample from 77 K to liquid state is not substantially different to that predicted theoretically in section 4.1, and would allow molecules with relaxation lifetimes on the order of seconds to be used for TJ-DNP.

4.4.2 Beam Manipulation

Transmission of Visible Light

Light propagates through matter with a speed lower than that through a vacuum, meaning that a light ray incident on a transparent medium at an angle $\theta_i \neq 0°$ to the normal will change propagation direction. This phenomenon, called refraction, allows electromagnetic radiation to be manipulated and directed towards specific targets. Refractive media can be shaped in such a way as to create lenses, components that, when placed axially in a beam of light, act to direct all incident parallel rays towards a particular point, or focus. This is done by introducing an axially symmetric, varying propagation angle using a radius of curvature. A number of simple beam operations are made possible using these lenses, summarized in figure 4.14, allowing complex optical paths to be designed. In the following examples, all lenses are assumed to be thin (such that the thickness of the components does not contribute to the focal length) and free of aberration by assuming the small angle approximation $\theta = \sin\theta$.

A collimated laser beam of radius r_i may be focused to a spot at distance $x = f$ using a lens with a focal distance f. The minimum possible spot radius of the focused beam, r_o is limited by the divergence of the original beam, θ_i, through the law of optical invariance expressed in equation 4.4.2.1.

$$r_i\theta_i = r_o\theta_o = \text{constant} \tag{4.4.2.1}$$

In a reciprocal manner, a diverging point source may be collimated by a lens placed a distance f away from it. It should be noted that no point source is infinitely small, and will have a radius r_i. This then limits the collimation of the output beam in accordance with equation 4.4.2.1.

Lenses may also used to create a real, magnified image at a distance s_o of a source of radius r_i, provided $s_i \neq f$. In this case the magnification, M, can be found as

$$M = -\frac{s_i}{s_o} = \frac{r_i}{r_o} \tag{4.4.2.2}$$

This relationship dictates that, for an optical system to provide a specific magnification, there is only one position along the optical axis at which a single lens can be placed.

It is possible to manipulate the radius of a collimated laser beam using two lenses. Expansion of a beam of radius r_i and divergence θ_i using a lens with a negative focal distance, $-f_1$, will create a virtual image of radius r_v at the distance $x = f_1$ on the source side of the lens (see figure 4.14). A second lens with a positive focal distance f_2 can then be placed $x = f_2$ from the virtual image, creating a propagating, collimated beam with a new radius $r_o = \theta_v f_2$. The law of lens reciprocity allows a beam to be both reduced in diameter or expanded by this technique.

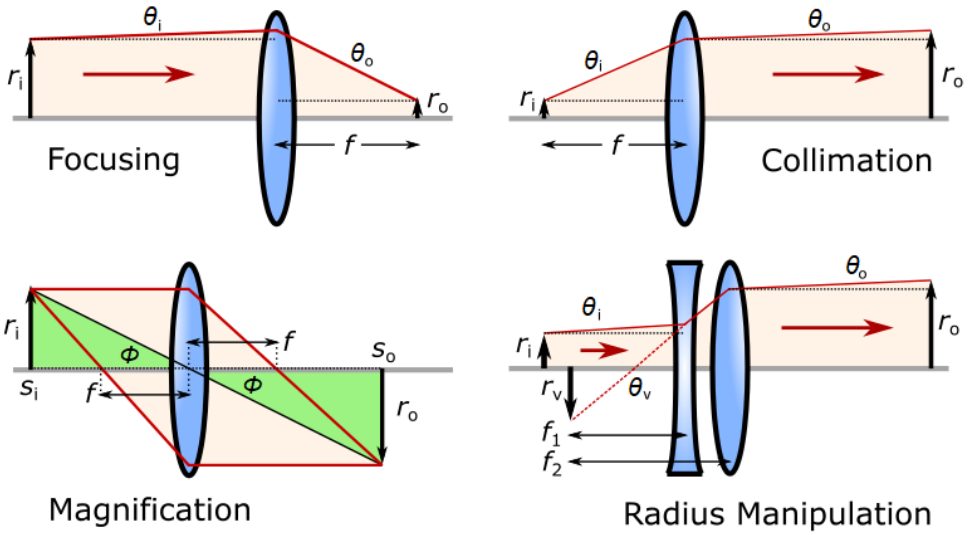

Figure 4.14: Schematic diagrams to illustrate the various ways in which lenses may be used to manipulate the characteristics of a beam of light.

Limitations of Lenses

In reality, optical components are limited in their ability to focus to a fine point by their manufacture, aberration (introduced as $\theta \neq \sin\theta$) and alignment (over long distances it becomes difficult to retain a precise optical axis). The lenses are also designed for use with flat wavefront radiation, whereas the laser used for this project has a Gaussian beam profile which creates a spherical wavefront as the beam propagates. While the radius of curvature of this wavefront tends to infinity at small distances of propagation, at longer lengths the effective focal characteristics of lenses could change, although these effects are minimal in the mid-IR regime.

4.4.3 Mid-IR Materials

Figure 4.15 shows a number of materials could be used to deliver Er:YAG laser radiation at 2.94 µm with minimal attenuation.[147–149]

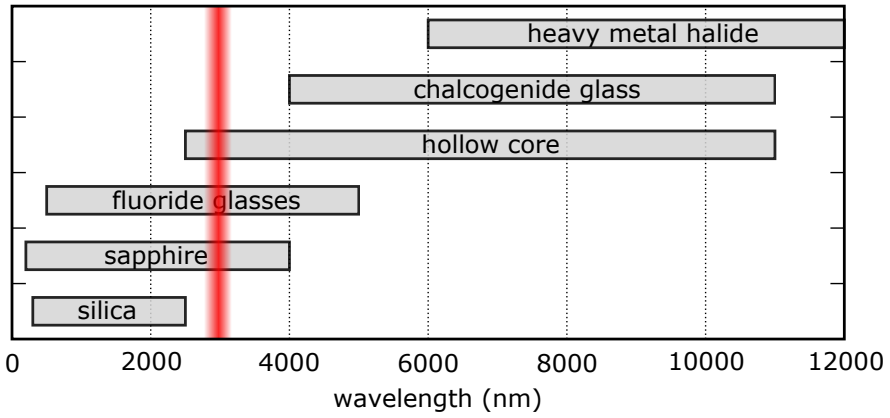

Figure 4.15: Suitable materials for the transmission of 2.94 µm radiation.[149] It can be seen that sapphire, fluoride glasses and hollow core transmission methods may be considered as materials for this application.

Fluoride glasses are able to transmit mid-IR radiation (∼0.4 - 5.0 µm), and are commonly used to make both lenses and optical fibres, capable of ∼95% transmission over a couple of metres. Although these standard fluoride glass optics are inexpensive, readily available and may be

anti-reflection coated to give better transmission, the materials, such as fluorozirconate and fluoroaluminate, are comparatively more fragile than other glasses, making fluoride glass fibre optics particularly fragile. An alternative medium for mid-IR transmission is sapphire, with a working wavelength range of ∼0.2 - 4.0 µm. Sapphire components are not only stronger than fluoride glass equivalents, but are also used in microwave applications due to their high microwave transmission.[115] However, sapphire is far more expensive and has a slightly lower transmission for mid-IR radiation than fluoride glass. This means that, although sapphire fibre optics may be stronger, the lower transmission make them less desirable for long path length applications. Finally, hollow core fibre optics and larger diamteter, mid-IR waveguides could be used, bearing in mind that a hermetic window will be required as the delivery is into a vacuum space. All optical components chosen for laser delivery must be able to cope with high powered mid-IR radiation. For this reason anti-reflection coated components are chosen where possible, capable of transmitting more than 95% of the beam (such as magnesium fluoride and barium fluoride). Where microwave irradiation is also expected, sapphire is used.

4.4.4 Sample Containment

A small sapphire cup was designed to hold the sample, capable of both mid-IR and microwave transmission. Sapphire was chosen for this cup because it is both microwave and mid-IR transparent,[115] allowing both DNP and mid-IR heating, and has a magnetic susceptibility close to that of the surrounding environment,[100] minimizing mismatches within the NMR space. The properties of sapphire are superior to quartz where mid-IR radiation is also used. Custom sample cups were then made (Impex GmbH, Germany) to allow two sample sizes, with cylindrical diameters

of 3 or 4 mm and lengths of 4 mm, to be used. Two designs were chosen for more control over heating. The cups were closed by a small, tightly fitting lid, and all surfaces normal to the laser and microwave radiation were polished to maximize transmission of radiation.

Figure 4.16: Both saphhire sample cup designs, shown next to a 2p coin for scale.

Although the sapphire lids are tightly fitting, they are not vacuum tight. This causes problems during the initial stage of the experiment in which the sample environment is evacuated, causing the sample to out-gas and overcome the tightly fitting lid, escaping into the VTI. To overcome this, initial out-gassing of the sample decreased the amount of gas dissolved therein, and the sample was frozen prior to loading. This freezing measure was only partially succesful, as the typical loading time of the NMR probe was of the order of minutes, meaning that any pre-frozen sample likely had time to melt before pumping could begin. The sapphire container was also wrapped using Teflon tape, holding the lid on during pumping. Teflon was chosen because it is NMR and microwave transparent, however no tape could block the laser path as it would absorb the radiation and burn. Practically speaking, wrapping the cup so as to substantially improve its vacuum characteristics, while not obstructing the laser path, was not possible. Accordingly, the experimental procedure includes an additional out-gassing and pre-cooling stage.

4.4.5 Laser Delivery Options

An optical path must be developed to deliver the high output power of the laser module across a moderate distance (∼2 m) to the sample within the VTI. This path needs to minimize losses associated with a long optical path length as well as allowing accurate alignment and direction of the beam such that it is incident on the small target at the end of the path. This path must also translate the horizontal output of the laser module into a vertical laser beam, as the sample is contained within the vertical bore of the spectrometer.

Optical Fibre

A fibre optic system may be used to deliver the radiation to the sample within the VTI, and could use a single fibre, focused onto the surface of the sample, or a number of fibres directed onto different points on the sample to achieve the temperature jump in a shorter time as shown in figure 4.17.

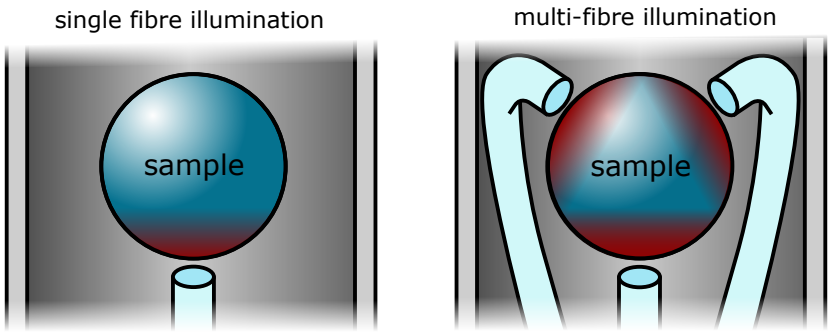

Figure 4.17: A schematic to show how multiple mid-IR transmissive fibres may be used to heat more of the surface of a sample and subsequently bring about a more rapid temperature raise.

Attenuation of the beam as it travels through the fibres can be minimized by choosing a high transmission material, and directing the beam becomes trivial. Furthermore, rare-earth doped fluoride fibres are being

developed to improve transmission of this radiation via optical amplification.[147,150] Although delivery using this method seems ideal, a number of considerations rule out the use of fibres for this experiment. To begin, focussing high powered laser radiation into narrow fluoride glass fibres causes plasma formation and damage to the entry interface itself,[148] subsequently hindering future transmission. Although composite optical steppers or hollow tapers can be used to minimize these entry effects,[151] sending high power laser radiation along long, fine fibres will still cause damage, as there will still be significant energy absorption along the length of the fibre.

Directing the beam from the horizontal output of the laser module up and along the vertical bore of the cryostat will require the fibre to bend through 90°. Although the space available underneath the magnet permits large radii of curvature outside the spectrometer, once inside the VTI any curvature allowing access to the top side of the sample will need to be on the order of millimetres. Not only is the transmission of mid-IR radiation through fibre optics degraded by lower radii of curvature,[152] but the low temperature mechanical properties of the materials may cause problems. Although fluoride glasses have low losses associated with radii of curvature in the centimetre regime[151] they becomes brittle at low temperatures and will fracture if curved.[148] The likelihood of this is lower for sapphire fibre optics, which may also bend to smaller radii of curvature,[153] but will still become brittle and break at the lowest temperatures used in this experiment. One solution to permit mid-IR transmitting fibres to bend at lower temperatures with less risk of breaking may be to reinforce the fibres using other materials.[152]

Free Space Transmission

Free space transmission of the beam, using readily available optics, may also be used to deliver the laser beam to the sample space. This method is cheap and relatively straight forward, but becomes more difficult the longer the path length. Firstly, uncontrolled divergence of the laser beam must be avoided, as this reduces the power per unit area of the beam as it propagates forward. Divergence can be limited using a single collimating lens, ideally creating a parallel beam that retains laser power and maximizes heating of the sample. This can be practically achieved with a lens with a focal length at the beam aperture, l_1, collecting the diverging laser radiation from the source and preserving it. This beam may then be reflected 90° using a mirror such that a perfectly vertical laser beam is incident on the sample inside the spectrometer. A gold-plated mirror with a high damage threshold may be chosen to reflect mid-IR radiation with low loss. If necessary, the damage threshold requirements of the mirror may be relaxed by choosing an initial collimating lens with a longer focal distance, allowing the laser to diverge in a controlled manner and lowering the power per unit area just enought to protect the optics.

To maximise energy transfer to the sample, the beam may be focused to a point using a focussing lens, l_2. An issue lies in the fact that the sample is located ∼500 mm up the bore of the spectrometer, and needs to be supported by a long tube inside the VTI. The length of this supporting tube, along with the focussing properties of the second lens, limit the power that can be delivered to the sample (see figure 4.18). If an additional lens, l_3, is placed between l_2 and the sample then a parallel, vertical beam may be created with a reduced diameter which depends on the focal distance of l_3. This reduction in diameter increases the power

per unit area of the beam, matching it to the dimensions of the sample and avoids losses associated with the tube supporting the sample, as shown in figure 4.18. A final aperture will be required to pass the beam into the evacuated space of the VTI.

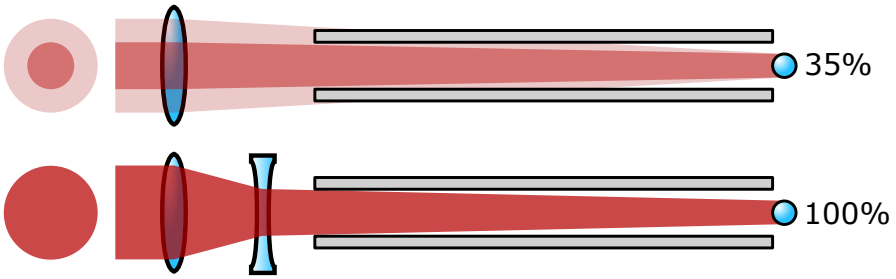

Figure 4.18: An illustration of how a long tube preceding the sample can drastically cut the light deliverable using a single lens. To overcome this a second lens may be used.

Any slight misalignment in this free space delivery introduces huge losses, amplified by the tiny target size at the end of the optical path. To improve alignment, high precision machining of the optics holders and beam path allow lenses, apertures and mirrors to be held exactly in place. Some lenses (such as l_3) need their positions along the beam axis finely adjustable to ensure the beam diameter is correctly matched to the sample. Furthermore, if the mirror is not correctly aligned then the beam will not be reflected by 90° and will subsequently miss the sample. Because misalignment is likely, due to the degrees of freedom associated with the reflection, the gold-plated mirror may be mounted on an adjustable plate, allowing fine control of tilt and yaw, as well as translational position.

Mid-IR Waveguide, Ø>5 mm

Mid-IR waveguides with macroscopic dimensions may also be used to direct high powered Er:YAG radiation with losses less than 0.2 dBm^{-1},[154] with transmisison increasing as the diameter of the waveguide is in-

creased.[155] Specifically, laser attenuation, L, is inversely proportional to the cube of the core diameter, d.

$$L \propto \frac{1}{d^3} \tag{4.4.5.1}$$

These waveguides comprise of a thin-walled glass or metallic tube, onto the inside of which is coated a highly reflective material,[156] such as gold and silver.[157] Furthermore, they have been shown to exhibit low losses even when bent to radii of curvature in the centimetre regime[158] and, accordingly, may be useful to direct the horizontal beam from the laser module into the VTI. Using a moderate waveguide diameter (~1 cm) also homogenizes the beam which may aid sample heating.[131] This method has been previously reported for mid-IR delivery for TJ-DNP.[39]

Free-space transmission may be used outside of the magnet, allowing the beam to reflect 90° up through a mid-IR transparent aperture and a hollow, plated waveguide may be used inside the VTI. The inclusion of this waveguide in this space may not introduce a large heat load, but must also not be damaged by exposure to low temperature. This method could be used alongside a single magnifying lens to project the laser aperture to the diameter of the waveguide opening (illustrated in figure 4.19). This allows divergence of the laser module to be neglected, providing the beam does not widen considerably prior to magnification.

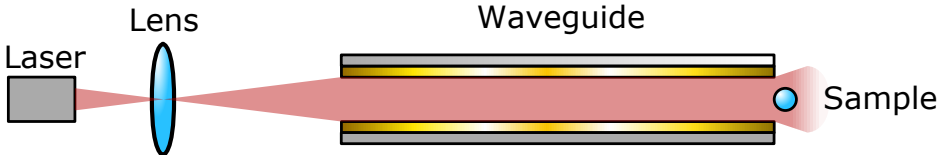

Figure 4.19: A magnifying lens may be used, alongside a coated waveguide, to allow low loss transmission of mid-IR radiation into the sample space.

4.5 The Heating Path Design

4.5.1 Delivery Schematics

Disregarding complete fibre optic transmission of the mid-IR radiation as unsuitable at low temperatures, a couple of delivery systems may be proposed. Figure 4.20 shows a free space laser delivery system that accounts for the divergence of the laser module by collimating the beam early on using a lens focussed onto the laser aperture, before refocussing and defining a beam diameter for sample irradiation using a lens pair after reflection into the VTI using a mirror. This method of delivery will be called the triple lens path, as it uses 3 lenses.

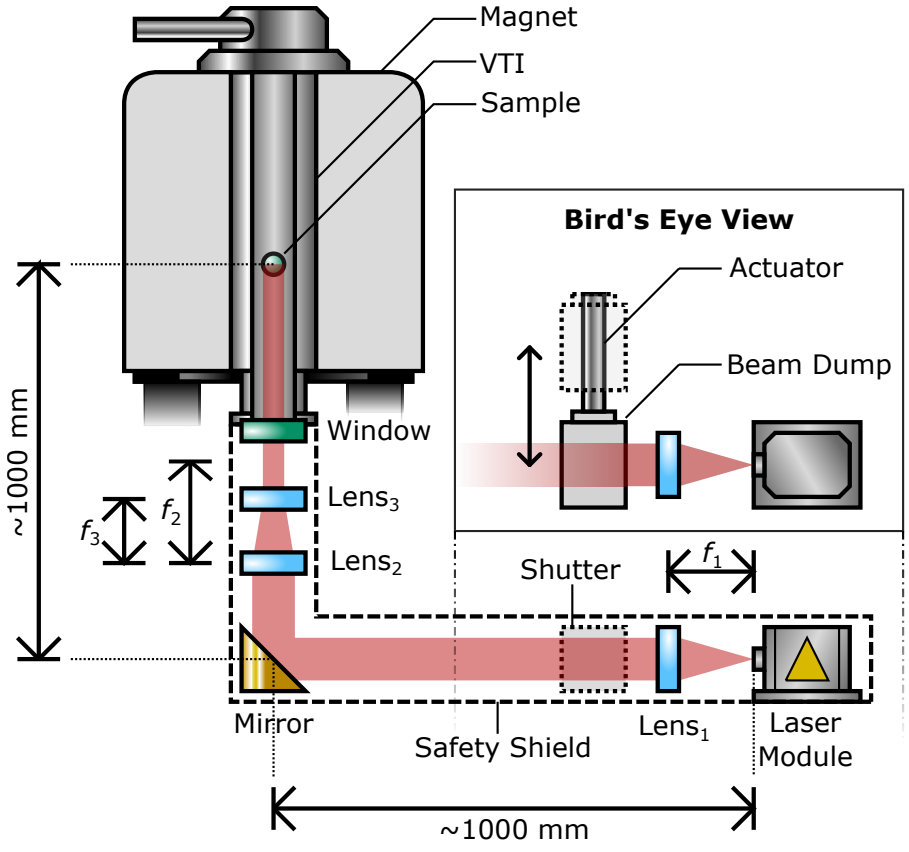

Figure 4.20: A schematic diagram to show the delivery of the laser beam from the source to the sample. Lens$_x$ has a focal length f_x. Path lengths are shown to be approximate due to the ability to adjust these values, and a bird's eye view of the shutter system has been included for clarity.

This triple lens system benefits from the fact that manipulation of the second lens pair allows the beam diameter to be matched to that of the sample, and collimation of the beam increases the cross sectional area of the radiation which reduces damage to the mirror. However, the high number of lenses increases transmission loss along the path and the likelihood of misalignment, and the divergence of the laser module needs to be known exactly for the laser to be precisely matched and delivered to the sample. The design will be such that triplets of lenses can be easily switched out for varying sample sizes. This method uses an anti-reflection coated, high transmission fluorinated glass window to form a vacuum seal between the VTI and laboratory space.

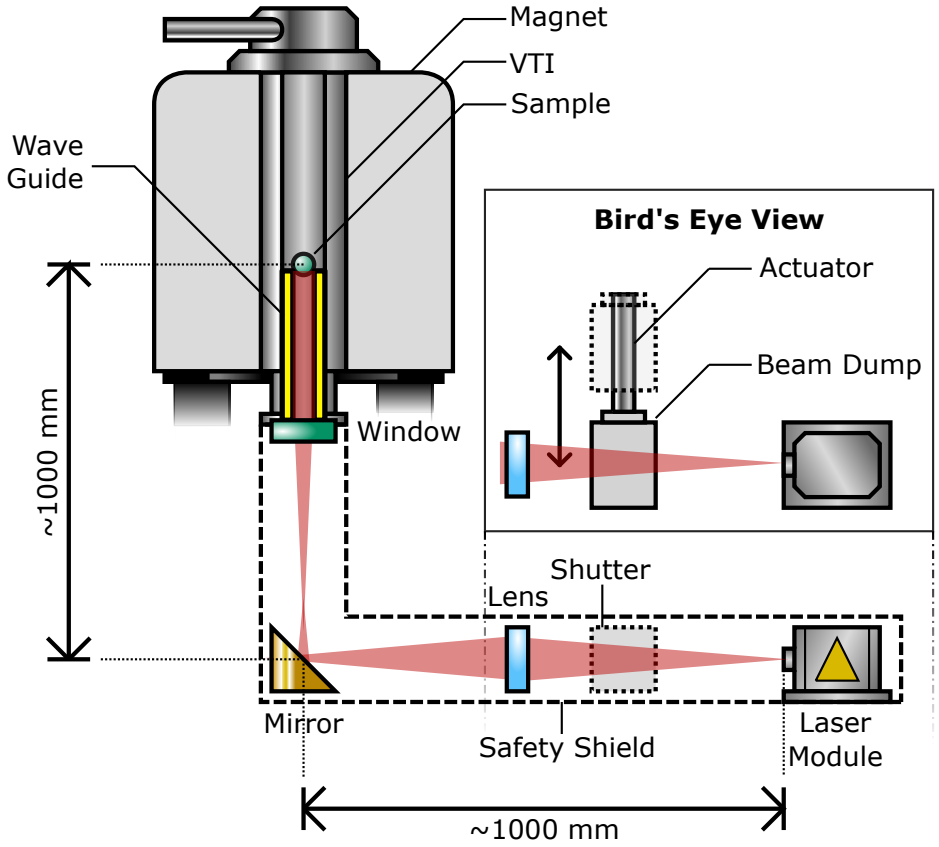

Figure 4.21: A schematic diagram to show the delivery of the laser beam from the source to the sample using an example magnifying lens. Path lengths are shown to be approximate due to the ability to adjust the set up and, again, a bird's eye view of the shutter system has been included for clarity.

Alternatively, a hybrid free space/hollow waveguide method may be used, as shown in figure 4.21. This method benefits from simplicity, with only one magnification lens to match the beam to the waveguide entrance, but the waveguide inside the VTI must not exhibit significant transmission loss or heating from the radiation. To maximize transmission an entirely separate waveguide that can be inserted into the sample support, with an internal diameter of about 4 mm, can be used. Again, this method uses a planar anti-reflection coated, high transmission fluorinated glass vacuum window.

4.5.2 The Laser Path

A system was designed such that both laser delivery systems (that using three lenses and that using a single magnifying lens) could be put together and tested with the VTI with little modification. The backbone for this design consisted of a non-magnetic, alluminium supporting beam which could be connected at variable height to the legs of the spectrometer. This support can be clearly seen in figure 4.22, which shows the hardware underneath the spectrometer to deliver mid-IR radiation. A spirit level could be used, alongside adjustable legs further along the support, to ensure that the laser beam was horizontal.

Onto this support was built, again using non-magnetic materials, an encolsure for the laser module featuring access for water cooling and a high current power supply, followed by the gas powered laser switch. A 45° prism with an external coating of gold is used as a mirror, as the precise angles of the prism ensure the beam is directed vertically up the bore of the VTI. This is attached to a small ThorLabs tilt and yaw table such that precise direction of the beam is achieved using micrometers.

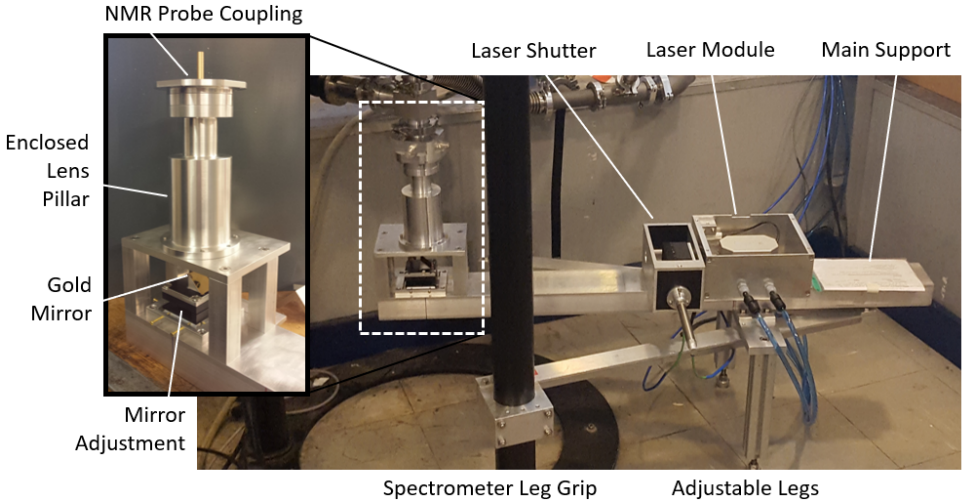

Figure 4.22: An image to show the hardware in place underneath the spectrometer for delivery of mid-IR radiation to the sample space inside the VTI.

Lenses are included into the design using ThorLabs lens holders. A space for the initial collimating lens is included within the narrow gap between the laser shutter and laser module box, and caging was included within the enclosed lens pillar after the mirror to precisely locate the final lenses that adjusted the beam diameter to that of the sample. These lens locations are highlighted in figure 4.23. For details of the laser waveguide once inside the VTI see chapter 5.

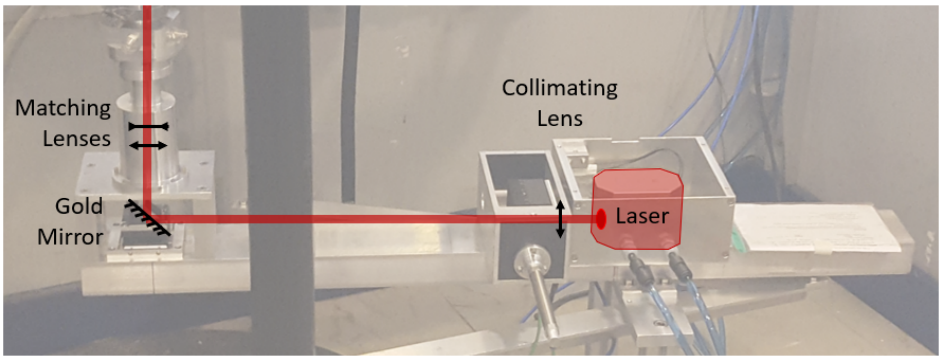

Figure 4.23: An indication of the lens locations and beam path through the hardware. To modify this path to allow single lens magnification the two matching lenses are removed and the collimating lens is swapped out for a magnification lens.

4.5.3 Laser Safety

Because the laser radiation used for the rapid heating mechanism is of such a high power, invisible to the naked eye and couples to vibrational bonds in water (and therefore the human body), careful containment of the beam is required to prevent injury. A custom enclosure is used to contain both the optical path at the base of the spectrometer (figure 4.24) and also to ensure no radiation escapes from the top of the instrument (indicated in figure 2.18 of section 2.2.3). This system is fully interlocked, such that removal of any of these enclosures stops laser exposure immediately.

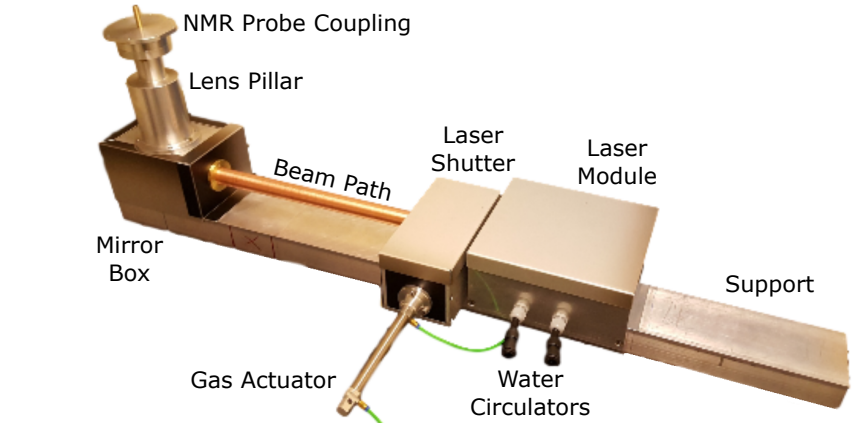

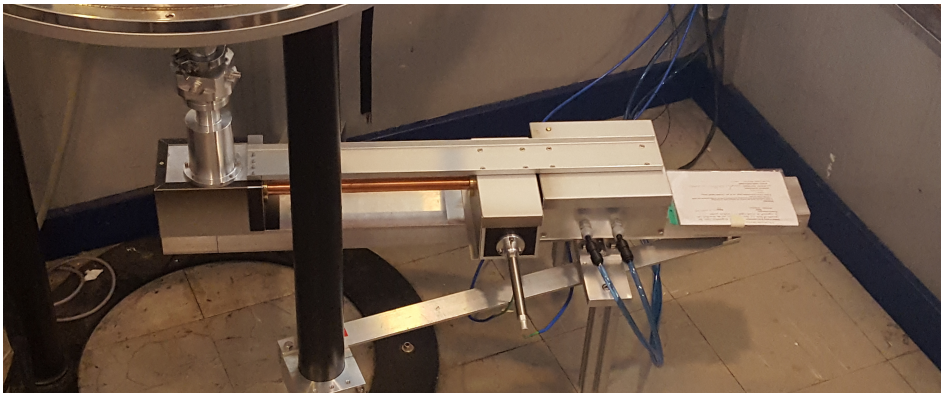

Figure 4.24: An image to show the interlock casing on the laser path. All casing is designed such that it cannot be removed without tripping an interlock switch, turning the beam off.

4.6 Infrared Path Results

Laser Power

Although the laser module was designed such that it was able to function under the effects of high field, the laser controller had to remain outside of the stray field. This increased the distance between the controller and the module which, in turn, reduced the current supply to the source to 160 A rather than the maximum 200 A used for initial experiments. Attempts to use higher capacity cable did not increase the current supplied to the module. This issue is not believed to be due to field effects under the magnet as the change in behaviour was first noted while testing the increased distance outside of the field, prior to installation. A power meter was placed immediately after laser output, and the effects of the reduction in current on the laser output was investigated, shown in figure 4.25. These investigations indicated a reduction in maximum radiation power from ∼30 W to ∼19 W due to the increased separation between the laser module and controller. Work continued into the optical path despite this issue.

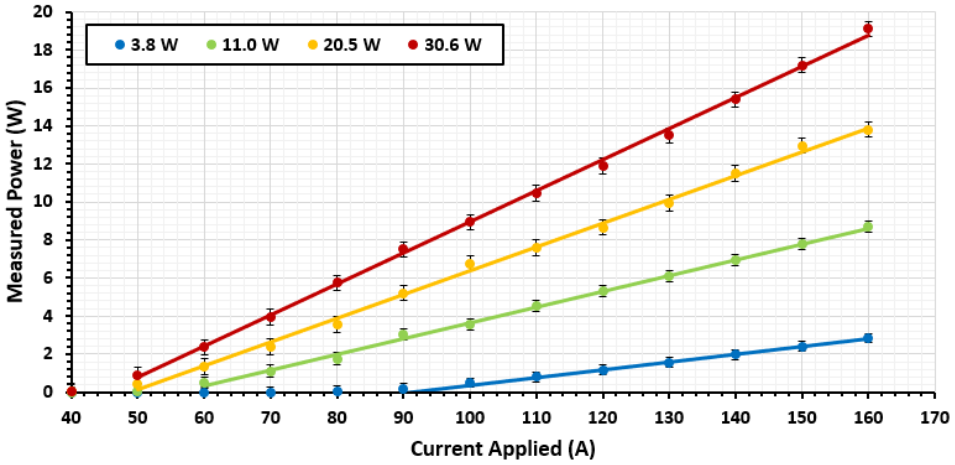

Figure 4.25: A figure to show the loss of laser power as the current supplied to the module is reduced. The inability to raise the current above 160 A is a direct consequence of increasing the distance between the controller and laser head. The legend shows the nominally quoted power at 200 A.

Beam Divergence

Measures of the laser divergence angle were performed to ensure that the beam was behaving as expected and to give full control over the beam. These measurements were performed by measuring the diameter of the laser spot using a high resolution thermal camera at varying distances from the laser aperture. When set to maximum output power, the divergence of the laser beam was measured as 1.26°, in agreement with specifications. Trigonometry could be used to calculate that, for optics with a diameter of 25 mm, any components further than ∼500 mm from the laser aperture would not collect all of the mid-IR radiation as the beam would have diverged too much. This was verified using a power meter with a diameter of 25 mm at different lengths along a beam of constant output as it propagated (figure 4.26). This result showed that all light could be collected if optics were placed in the first 500 mm of the beam path.

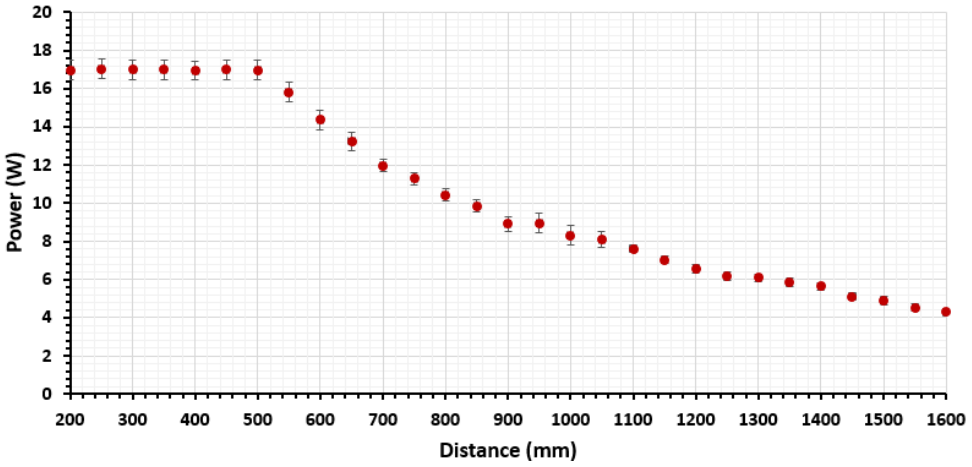

Figure 4.26: A graph to show how divergence of the laser beam decreases the power collected by 25 mm diameter lenses placed more than 500 mm down the optical path.

It could also be noted that divergence increased with power, suggesting that a free space transmission solution that worked across all output powers was not achievable.

Transmission Characteristics

All windows and lenses were placed in the laser beam to ensure that their transmission characteristics were as quoted and did not degrade the power delivery of the path. All showed transmission greater than 96%, suggesting the total maximum loss $L_{\max}$ through n windows and lenses, $L_{\max} = 0.96^n$, would not exceed 85% in any proposed system.

4.6.1 The Triple Lens Path

Work first began testing the triple lens optical system which collimated the diverging beam for free space transmission, before reducing the beam diameter to match the sample diameter.

Alignment

This method of delivery requires precise beam alignment along an optical path, performed using ThorLabs caging and tested using a number of high-capacity, in-house built targets (shown in figure 4.27). This testing was performed in a dedicated, interlocked dark room with a beam of radiation with a reduced power (1.9 W) for safety.

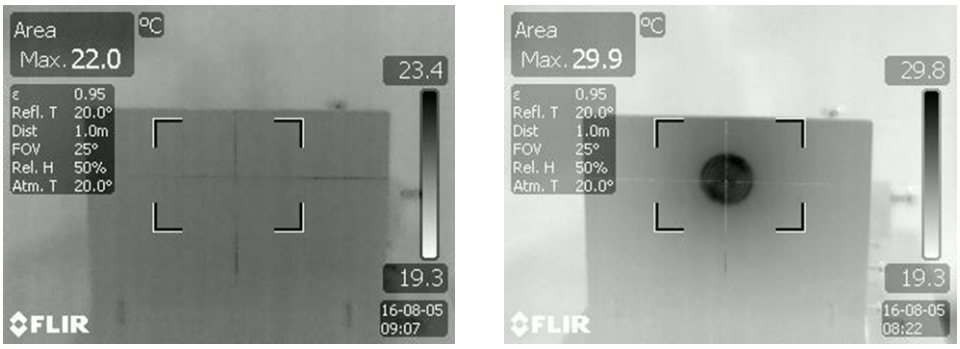

Figure 4.27: An image to show an optical alignment target used to ensure that the laser and any lenses were aligned correctly. The image on the *left* shows the target without beam exposure, while that on the *right* shows the laser exposure on. This spot size did not grow significantly with time as the target was an effective heat sink.

Provided the beam passes precisely along the optical axis of the horizontal arm of the optical path, the multiple degrees of freedom of the mirror may then be used to direct the beam vertically through any further optical components to the sample position. This is shown in figure 4.28 as a target is used with vertical ThorLabs caging after the mirror. The fact that the laser spot is located in the center of the cross as the target is moved up the vertical caging suggests good optical alignment. This figure also shows a small laser beam diameter as the target is moved to ∼2 m from the laser aperture. This is the effective sample location, and the three lenses have been used to match the diameter of the beam to the sample within the cryostat. The laser spot can be observed to heat the high-capacity target to a temperature ∼50 K higher than room temperature.

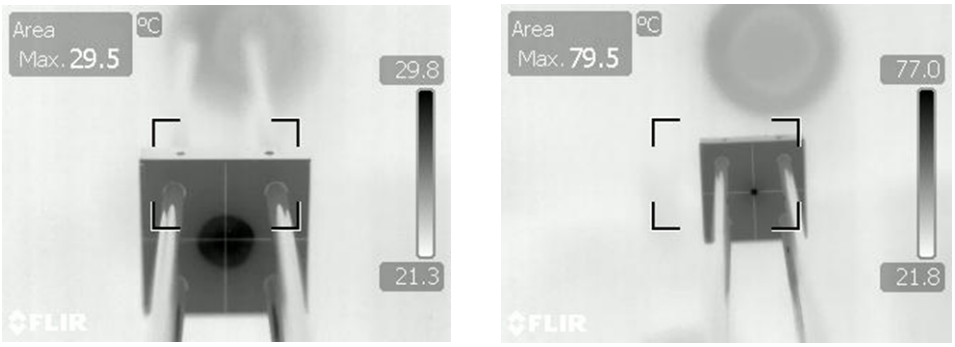

Figure 4.28: An image to show the optical alignment target which ensured that any lenses used on the vertical arm of the laser path were aligned correctly. The picture on the *left* shows the laser spot imaged without the second two lenses in place, while that on the *right* shows the beam matched to the sample size. This second spot is at the sample distance.

With the laser beam aligned to the sample space, and a promising rise in temperature of the target noted, the NMR probe could be attached to the path with a sample, and realistic heating could be investigated. This was also done in a dark room for safety.

Initial Sample Heating

Although heating was observed using the NMR tube and sample (figure 4.29), the effects were small. High resolution thermal imaging was used, along with pixel analysis, to measure the rise in temperature of the sapphire sample cup as a direct consequence of mid-IR laser irradiation of the sample.

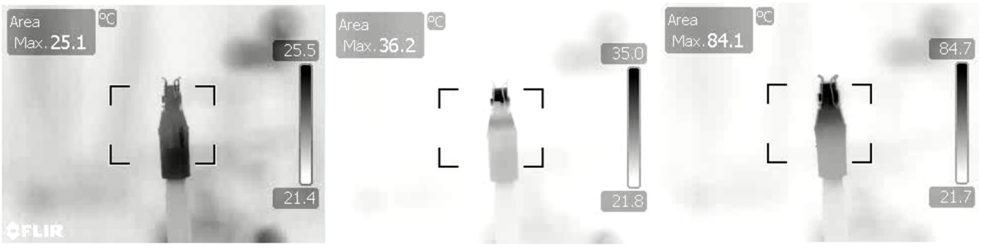

Figure 4.29: Three images of the sample held in the probe tip during heating. The image on the *left* is taken before heating begins, that in the *center* is immediately after irradiation is begun and the picture on the *right* shows the sample after 30 seconds of 1.9 W irradiation.

It is possible to observe the heating effect on the sapphire sample cup (figure 4.30), noting that these experiments use a limited power for safety (1.9 W) and a sample in an ambient environment at atmospheric pressure, meaning that far more heat sink processes are present than will be within the bore of the VTI.

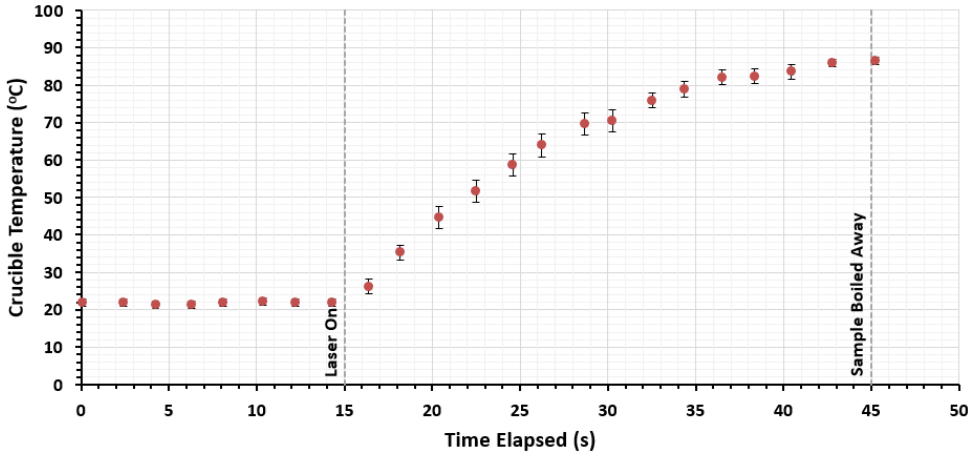

Figure 4.30: A graph to show the surface temperature of the sapphire sample cup as a function of exposure time. The sample was irradiated with a mid-IR laser at 1.9 W.

These experiments noted the sample began boiling away after a period of about 10 seconds, continuing until the sample was entirely absent from the cup, a point highlighted in figure 4.30. This suggests that thermal imagery is not suitable for measuring sample temperature, which is much higher than the external surface of the sample cup.

Optical Invariance

Despite the apparent success of initial experiments and low attenuation recorded through optical components, delivery onto the sample at the end of the laser path was noted to suffer from significant losses. One suspect for this low delivery is the law of optical invarience, quoted in equation 4.4.2.1. Using this expression, it can be inferred that the product of divergence, θ, and the cross-sectional area of the beam, A, is constant. Therefore the maximum power that can be delivered to a sample, P_{del}, from a laser with an output power P_{laser}, is given by

$$P_{\text{del}} = P_{\text{laser}} \cdot \kappa = P_{\text{laser}} \frac{A_{\text{del}} \cdot \theta_{\text{del}}}{A_{\text{laser}} \cdot \theta_{\text{laser}}} \tag{4.6.1.1}$$

where A_{del} and θ_{del} are the area and restricted delivery angle of the sample, respectively. Figure 4.31 shows how A_{del} and θ_{del} are restricted by the three lens experimental set-up (in this case by the long tube supporting the sample).

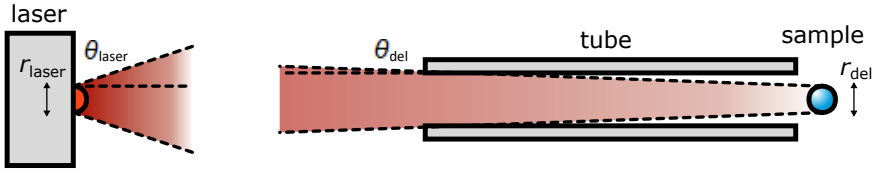

Figure 4.31: The ability to supply power to a divergence limited sample becomes drastically reduced if the angle at which the light can hit the sample is shallow.

Equation 4.6.1.1 effectively states that, if a laser output module with an aperture 1.6 mm in diameter and with a divergence of 1.26° is used to irradiate a sample which is sat at the end of a 500 mm tube of inner diameter 6 mm, a very low fraction of light will be delivered, as $\kappa \approx 2$ %.

4.6.2 Single Lens Magnification

With the possible limitations introduced by the law of optical invariance and the supporting shaft of the sample within the NMR probe, a simpler method of laser delivery using a single magnification lens was investigated, alongside a mid-IR waveguide.

Initial Results

A solution by which the laser beam aperture was simply magnified onto the entrance to the tube was tested, removing any limitations caused by the sample support within the VTI. A magnifying lens was placed within 500 mm of the laser aperture, as dictated by the results of early divergence experiments, and the beam diameter was matched to the inner diameter of the supporting tube within the probe. Although the magnified power at the entrance to the tube was measured to be practically the same as the output power, it was noted that transmission dropped dramatically at the end of the tube. This was believed to be both due to the structural breaks inside the supporting tube and the fact that this testing did not use a specifically coated waveguide, but rather an unpolished stainless steel tube. To investigate these reductions further, lengths of stainless steel tube, with an inner diameter of 6 mm, were cut and polished such that loss of mid-IR radiation down the guide could be measured. These tubes performed well as waveguides (figure 4.32), suggesting the breaks in the NMR probe shaft were the larger problem.

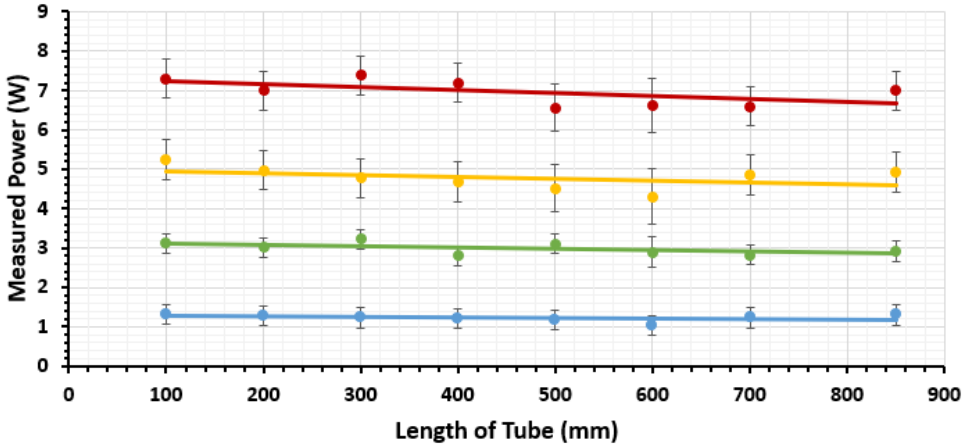

Figure 4.32: Measured power down a length of polished stainless steel tube, with an inner diameter of 6 mm. The laser beam was magnified onto the end of the tube as would be expected in an experiment.

The loss down these tubes was dependent on laser power, possibly due to local heating effects which were seen along the length of the tube using the thermal camera.

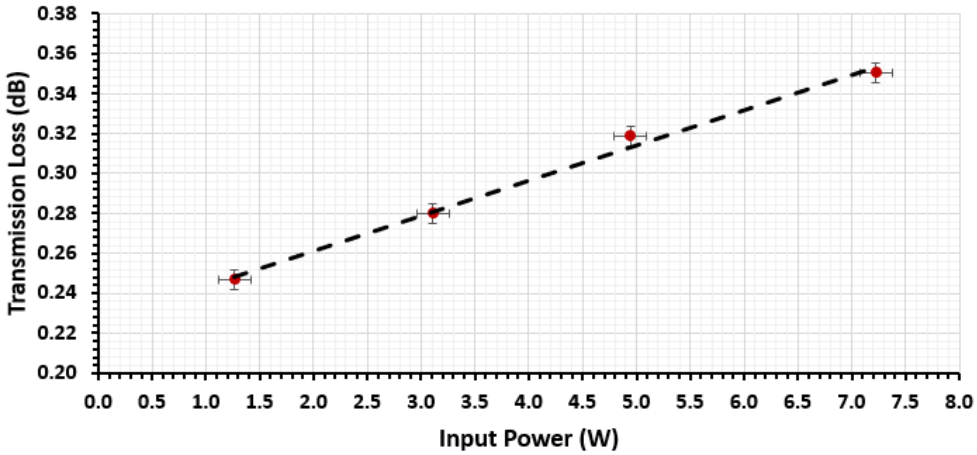

Figure 4.33: A plot to show the dependence of transmission loss along a stainless steel tube on the laser power that it accepts.

It is likely that these delivered powers will be further improved by a gold coating inside the waveguide, with local heating decreased within the waveguide and transmission improved. This waveguide could be slotted into the existing laser transmission pathway on the bespoke probe, circumventing the issues associated with the macroscopic breaks along the shaft.

4.7 Raman Thermometry

Documenting the rapid temperature-jump will allow the process to be optimized. However, most thermometry techniques introduce a thermal load to the sample and experience delays in readout time, making them unsuitable for use at low temperatures or with fast changes. A less-invasive, rapid method of Raman thermometry using laser radiation was developed for this experiment to document the temperature jump.

4.7.1 Raman Spectroscopy

Raman spectroscopy uses inelastic scattering of light, influenced by molecular vibrations, to deduce information about the underlying physical properties of a system. Local distortion of the molecular electromagnetic field caused by incident laser light creates unstable, virtual energy states from which photons are quickly re-radiated,[159] with any changes from the original laser energy giving an indication of molecular behaviour. If the scattering arises only from deformation of the electron cloud then the change in energy of the re-radiated photons will be tiny and the event can be described as elastic, Rayleigh scattering. However, if the interaction causes a large change in energy, due to molecular motion, the event is described as inelastic Raman scattering (see figure 4.34). The change in energy ΔE of the scattered light is shifted by a frequency ν_s from the original frequency, with Raman spectroscopy conventionally using units of wavenumbers, ϖ, an inverse wavelength (measured in cm^{-1}).

$$\varpi = \frac{1}{\lambda} = \frac{\nu_s}{c} = \frac{\Delta E}{hc} \tag{4.7.1.1}$$

It is possible to identify specific chemical groups responsible for Raman shifted photons as the energy change corresponds to characteristic

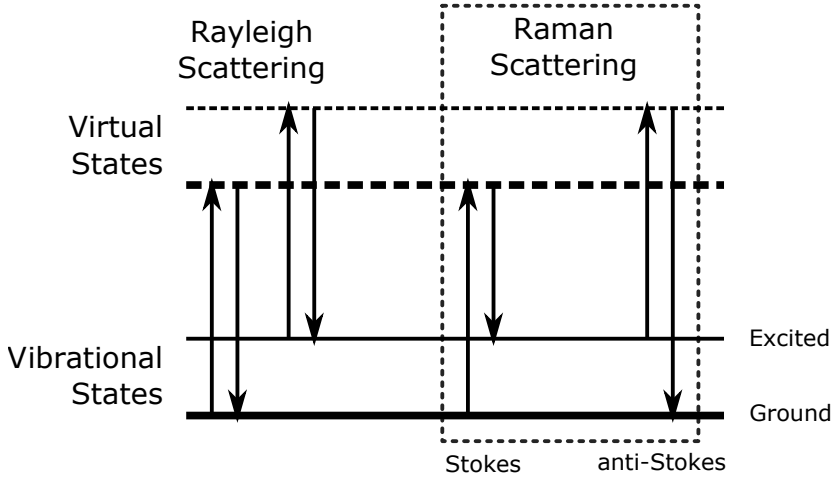

Figure 4.34: A diagram showing the basic Rayleigh and Raman scattering transitions between vibrational levels and virtual states caused by local electromagnetic field distortions. Further labelling has been given to events that lose or gain energy, as Stokes and anti-Stokes events respectively.

dynamics displayed by certain molecular environments. As an example, the vibrational mode of a hydroxyl bond (O−H) is identified by the presence of scattered photons within the range of 2850 - 3550 cm^{-1} manifesting as a broad peak in a Raman spectrum.

4.7.2 The In-House Raman Spectrometer

To build a Raman spectrometer, the sample needs to be irradiated with an excitation laser before allowing weak intensities of frequency shifted light to be collected. The physical properties of the excitation source directly affect the scattering of light, with the scattered power of light per molecule, P, represented by looking at the oscillating dipole moment induced by the incident radiation.[160]

$$P = \frac{8\pi^3\alpha^2 I}{3\varepsilon_0^2\lambda^4} = \frac{8\pi^3\alpha^2 I\nu^4}{3\varepsilon_0^2 c^4} \tag{4.7.2.1}$$

In this expression, ε_0 is the permittivity of free space, α is the molecule polarizability and all other constants have their usual meanings. The

dependence of this scattering power on the intensity, I, wavelength, λ, and frequency, ν, of the exciting laser are important, as these can be instrumentally manipulated to enhance the Raman signal.

The scattered power scales linearly with incident laser intensity, suggesting higher laser powers will produce stronger Raman scattered signals. This stated, the price of laser modules increases dramatically as the power increases, and the high power may cause heating effects on a low temperature sample. The intrinsically linked wavelength and frequency dependence follows a fourth power relationship, indicating a necessity for the wavelength of the exciting laser be kept as low as possible. In reality this value is dictated by the availability of optics, placing a limitation on the minimum excitation wavelength. Most systems for Raman spectroscopy use 532 nm as an excitation wavelength, as optical components are readily available and the scattered power is substantial.[159]

Design Specifics

A monochromatic laser source is used for spectroscopy, as any variation in excitation frequency causes broadening of the Raman peaks. The addition of a laser line filter after the laser source ensures the excitation frequency is as narrow as possible. Lenses are then used to focus the light onto the sample and to collect the light scattered by the sample onto the spectrometer, increasing the strength of the Raman signal. After the light has scattered from the sample a number of filters are used. To begin, the intensity of the Rayleigh scattered light at room temperature is $\sim 10^8$ times greater than Raman scattered light,[160] so the far stronger Rayleigh signal needs to be suppressed. This is done using band-stop filters, or notch filters, reducing the excitation frequency of the laser

and ensuring that both the anti-Stokes and Stokes regions of interest are passed. A number of additional notch filters are used along the optical path to repeatedly suppress the Rayleigh scattered signal such that Raman scattering can be observed. A dichroic mirror, at 45° to the beam, is used to direct the Raman scattered light into the spectrometer, further isolating the signals and suppressing Rayleigh scattered light. The addition of a beam dump in conjunction with the dichroic mirrors ensures that any laser light that passes through the component is extinguished rather than reflected back into the detection equipment. A complete schematic for this Raman technique is shown in figure 4.35.

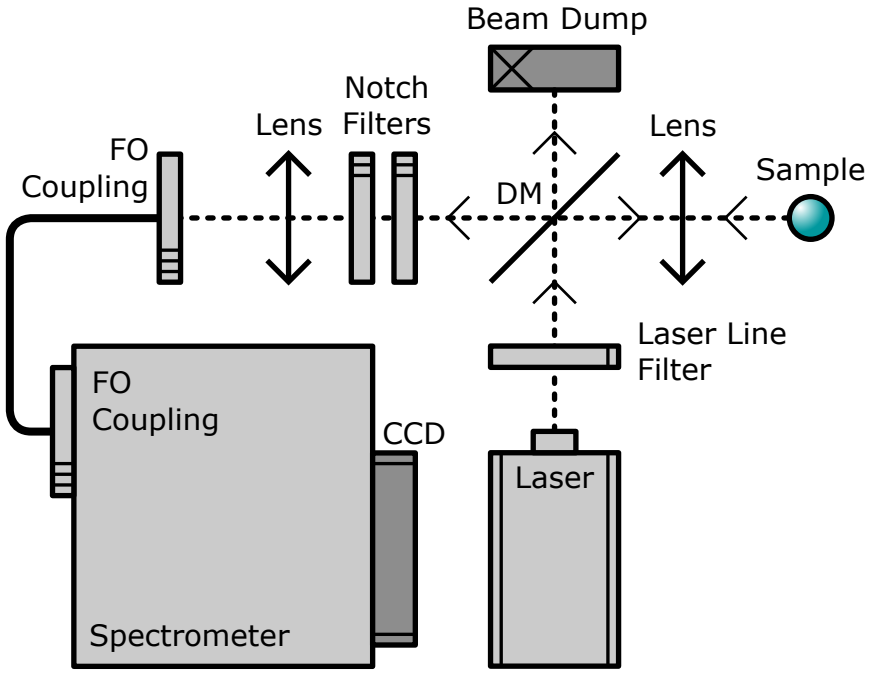

Figure 4.35: A schematic representation of a Raman spectrometer for Stokes scattered light collection.

The sample is irradiated with a 532 nm, 5 mW laser (MGL-F-532-5mW, CNI, China) with Raman scattered light collected by a diffraction spectrometer (iDus and Solis, ANDOR, UK) using an optical fibre. All optics were purchased from ThorLabs, except for the dichroic mirror and laser line filter, which were from Laser 2000. These components were

fixed to an optical table and aligned using ThorLabs optical scaffold. This instrument was built in an interlocked dark room to reduce background light, and is shown in figure 4.36.

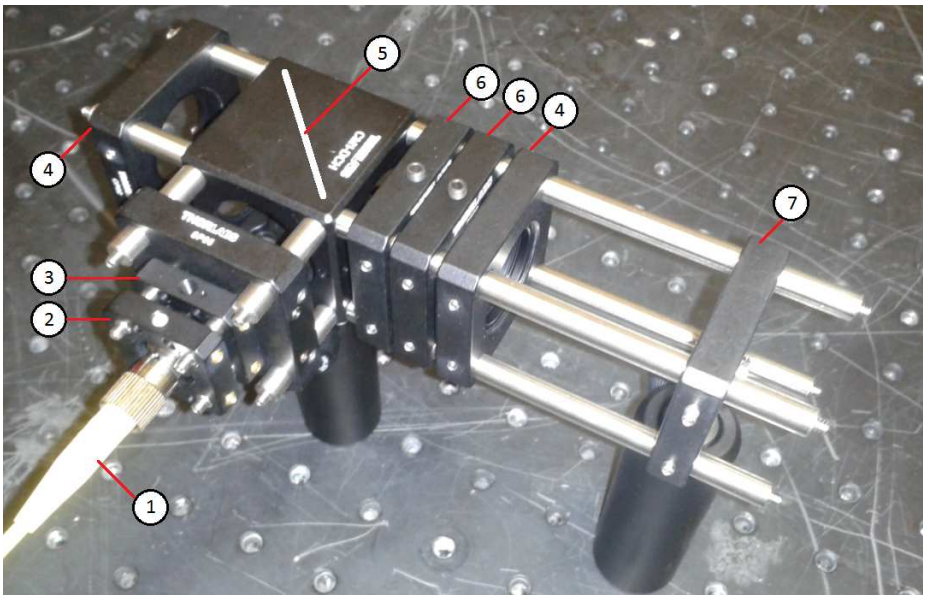

Figure 4.36: The in-house built Raman spectrometer, stripped of light-shielding (1 - Laser Coupling, 2 - Fibre Optic Coupling, 3 - Laser Line Filter, 4 - Lens, 5 - Dichroic Mirror, 6 - Notch Filter, 7 - Coupling to Spectrometer itself).

System Validation

The in-house model was tested alongside a commercial instrument with a sample of a 50:50 water-glycerol. The results, presented in figure 4.37 show that, although the signal strength is far lower in the in-house spectrometer, the characteristic Raman peaks of the sample can be identified. A number of different samples were tested, continuing to validate the in-house Raman spectrometer, but the spectra were averaged over 1000 seconds, providing good analytical information from the instrument but not showing potential for rapid experiments. The absorption peak visible when using the in-house spectrometer is believed to be from the sample holding cuvette and, because it does not interfere with the O−H stretching signal, is ignored.

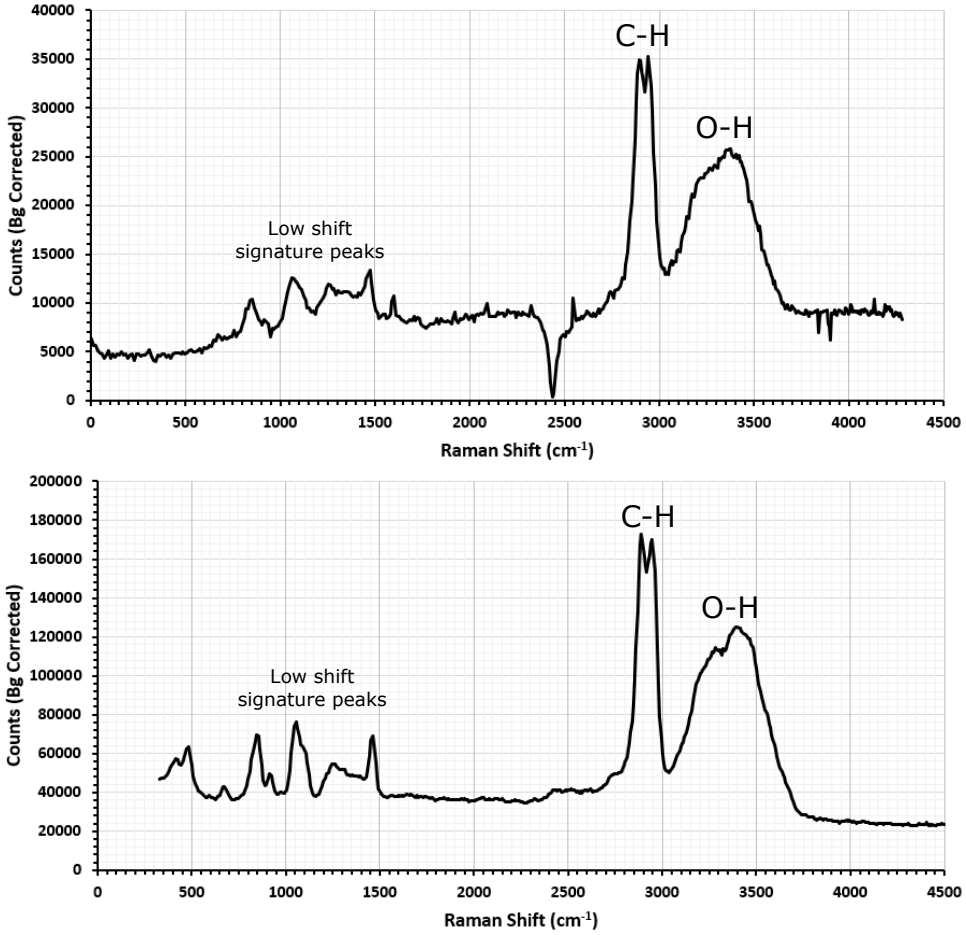

Figure 4.37: Comparison between in-house (*above*) and commercial (*below*) Raman spectrometers. Both scans used a 50:50 water-glycerol sample and comprise 1000 averaged 1 second scans. Peaks of interest have been labelled.

Sub-Second Exposures

Exposure time was investigated to evaluate how quickly the instrument could acquire useful spectra, with a linear decrease in signal intensity as this time decreased. This may render the technique unusable, as exposure times in the millisecond regime are desired to investigate the sub-second jumps of the experiment. The spectra shown in figure 4.38 show the signature shape of the O−H stretching peak present in the 50:50 water-glycerol sample as the exposure time of the instrument is reduced, with noise making the peaks difficult to resolve. The broader peak from 3000 cm^{-1} to 3500 cm^{-1} is that expected to shift as a function

of temperature and therefore needs to be tracked clearly. The stronger C−H bond signal on the left is not expected to shift.

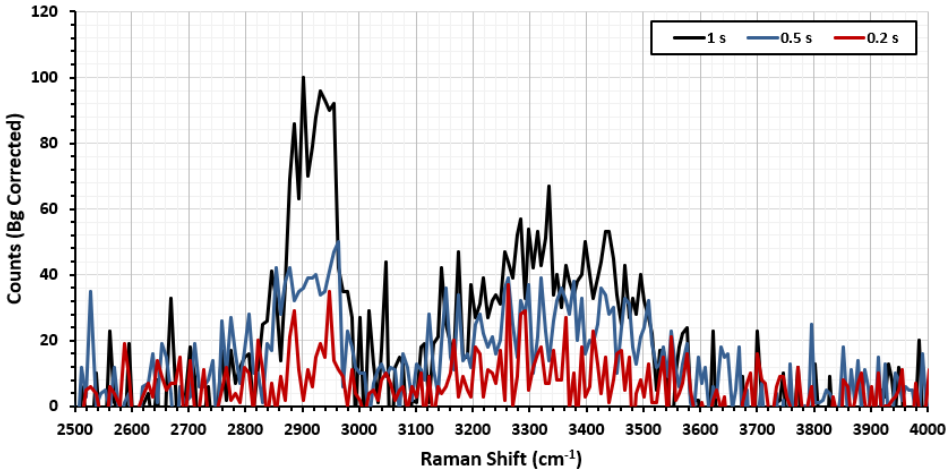

Figure 4.38: 50:50 water-glycerol Raman spectra focussing on the Stokes region between 2500 cm^{-1} and 4000 cm^{-1}, varying short exposure times. The C−H signal is the narrower peak on the left and the O−H signal is the broad peak on the right.

To overcome the decrease in the signal-to-noise of the spectra, curve fitting using MATLAB was used to process the Raman data, allowing the characteristic shifts of the Raman peaks to be identified. This invloved an initial baseline correction (figure 4.39), isolation of the region of interest and then removal of background signal, prior to fitting a Gaussian curve to the characteristic peaks (figure 4.40). This process allows sub-second exposure times to be used to evaluate sample temperature.

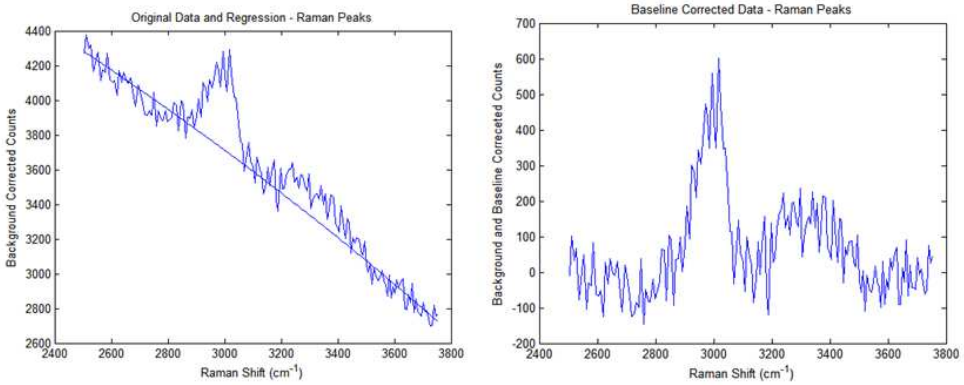

Figure 4.39: The baseline correction for the characteristic 50:50 water-glycerol peaks.

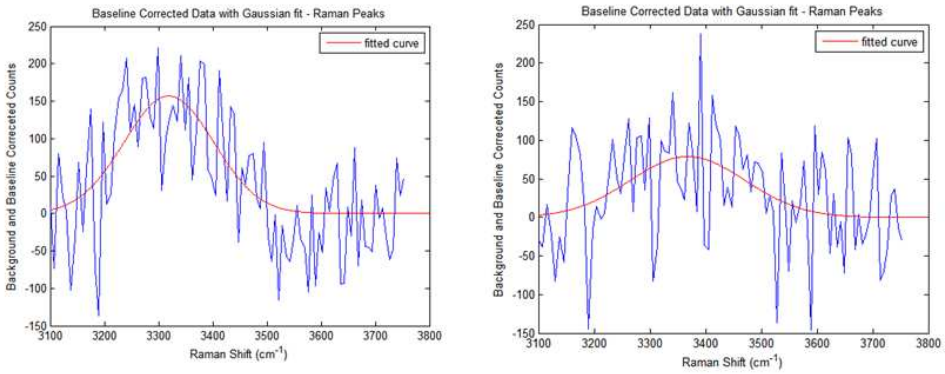

Figure 4.40: MATLAB fitted Gaussian curves, from which peak position can be evaluated. The corrections and fitting shown is for actual data.

4.7.3 Thermometry using Raman Spectroscopy

It is possible to investigate temperature dependent shifts in the spectrum brought about by changes in bond properties.[144] For example, the signal received from the O−H group is a superposition of the separate signals received from various types of hydroxyl bonds, such as those further bonded to different parts of the molecule and those that are not (see figure 4.41).

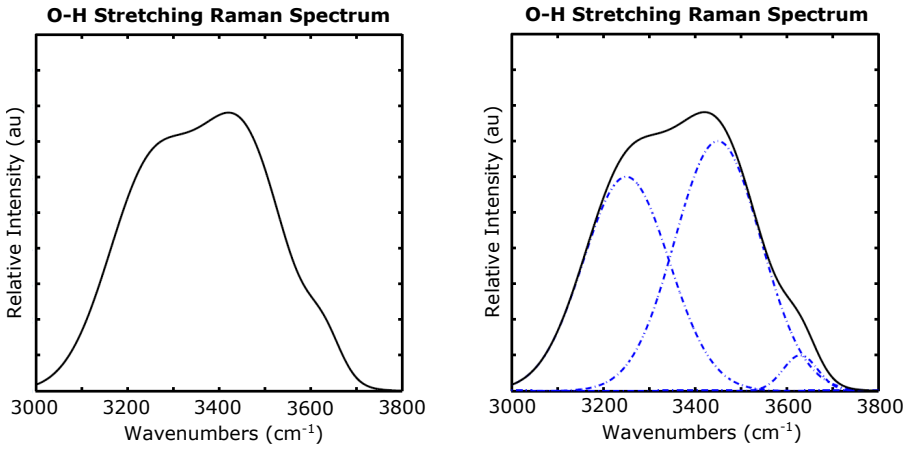

Figure 4.41: A synthetic Raman spectrum representing the Stokes O−H stretching region for water. Gaussian curves have been fitted (*right*), representing different bond types within the molecular environment.

The amplitude of these separate components will be proportional to the concentration of contributing bond types, which depend on the tem-

perature of the sample. Measuring certain parameters of the Raman data, such as the ratio between peak intensities and overall signal shape evolution, provides a method for calculating sample temperature.

A sample of 50:50 water-glycerol was prepared and placed in a small cryostat (TK1813, Thomas Keating Ltd., UK), cooled to liquid nitrogen temperature and subsequently allowed to warm to ambient temperature, while taking 20 second long exposures (to initially establish proof-of-principle) with the in-house built spectrometer. This exposure time was chosen to significantly reduce noise in these early testing stages and was not problematically long as the cryostat was slow to warm up ($\sim$ 6 hours). Temperature calibration was performed using an external sensor in the cryostat space. The O$-$H stretching peak travels from $\sim$ 3325 cm^{-1} at the lower temperature limit to $\sim$ 3380 cm^{-1} at ambient temperature (shown in figure 4.42). This could then be used to calibrate temperature. This shift is not observed for the C$-$H stretching band, as expected (see figure 4.43).

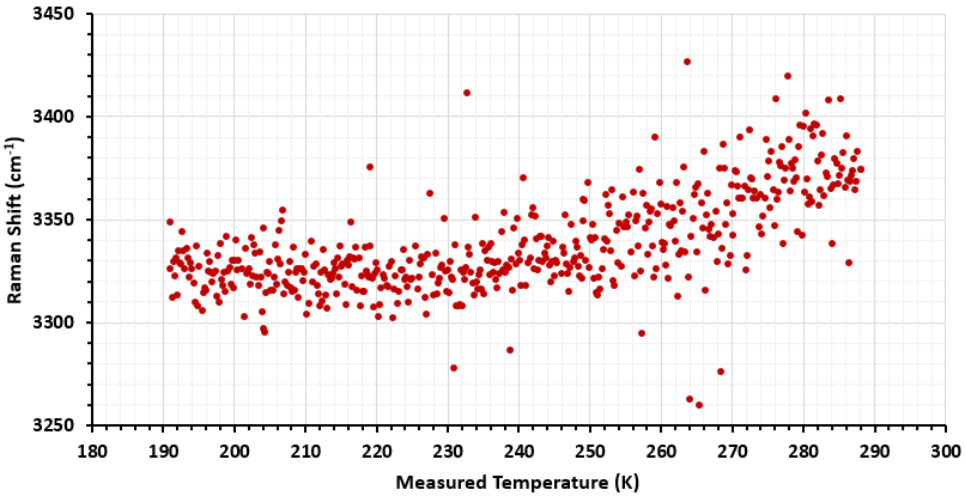

Figure 4.42: Characteristic Raman peak shifting as the sample warmed up to ambient temperature for the O$-$H stretching peaks. This shows that the peak does not shift as a function of temperature below $\sim$230 K.

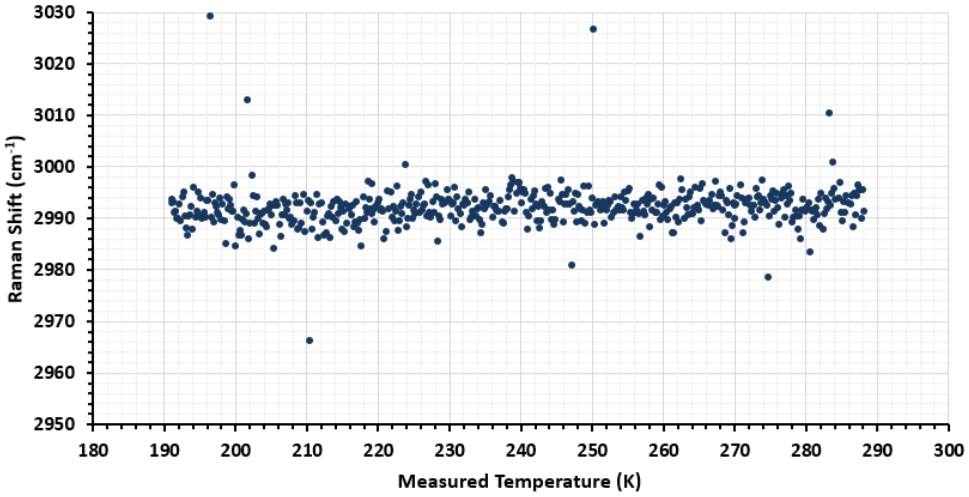

Figure 4.43: The C−H stretching peaks showing no change in Raman shift as a function of temperature. This data set is from the same experiment as that used to obtain the O−H data.

Although the peak shift is clear in figure 4.42, an exposure time of 20 seconds does not permit this technique to be used to measure the rapid temperature-jumps associated with this project. What is more, the characteristic shifting stops below ∼230 K, possibly due to O−H bonding becoming uniform and transient bonding being frozen out. While the signal-to-noise could be improved by improving optics and increasing the excitation power (although this may then begin to effect the sample itself), thus allowing smaller acquisition times, the lack of shifting below ∼230 K renders this method inappropriate for the lower temperature ranges used in this project.

4.7.4 Alternative Raman Thermometry

An alternative method for Raman thermometry was developed to use the temperature dependent population of the system energy levels, as described by Boltzmann statistics[159]

$$\frac{N_{\mathrm{n}}}{N_{\mathrm{m}}} = \exp\left(\frac{-\Delta E}{kT}\right), \tag{4.7.4.1}$$

where N_{n} and N_{m} are the number of molecules in the excited and ground states, respectively. Using equation 4.7.1.1 it is possible to rewrite this to include Raman shift ν_{s},

$$\frac{N_{\mathrm{as}}}{N_{\mathrm{s}}} = \exp\left(\frac{-h\nu_{\mathrm{s}}}{kT}\right). \tag{4.7.4.2}$$

The intensity of a specific Raman peak, I, can be related to the number of molecules responsible for that shift[161] by the proportionality factor expressed in equation 4.7.2.1, P, where $P \propto \nu^4$.

$$I_{\mathrm{x}} = N_{\mathrm{x}}P \tag{4.7.4.3}$$

$$I_{\mathrm{x}} = AN_{\mathrm{x}}\nu^4 \tag{4.7.4.4}$$

with A a constant relating frequency to P. If Stokes scattering is represented by $(\nu_{\mathrm{l}} - \nu_{\mathrm{s}})$ and anti-Stokes scattering represented by $(\nu_{\mathrm{l}} + \nu_{\mathrm{s}})$, where ν_{l} is the frequency of the excitation laser and ν_{s} is the frequency of Raman shift, we can substitute this for each case into equation 4.7.4.4

$$I_{\mathrm{s}} = AN_{\mathrm{s}}(\nu_{\mathrm{l}} - \nu_{\mathrm{s}})^4 \tag{4.7.4.5}$$

$$I_{\mathrm{as}} = AN_{\mathrm{as}}(\nu_{\mathrm{l}} + \nu_{\mathrm{s}})^4 \tag{4.7.4.6}$$

It follows that

$$\frac{I_{\mathrm{as}}}{I_{\mathrm{s}}} = \left(\frac{\nu_{\mathrm{l}} + \nu_{\mathrm{s}}}{\nu_{\mathrm{l}} - \nu_{\mathrm{s}}}\right)^4 \exp\left(\frac{-h\nu_{\mathrm{s}}}{kT}\right) \tag{4.7.4.7}$$

This equation links the intensities of the Stokes and anti-Stokes Raman shifts to temperature. It should be noted that the anti-Stokes signal is minuscule compared to the Stokes, making this method more difficult to implement as a thermometry technique.

Design Alterations

To implement this method of Raman thermometry the in-house built spectrometer was reconfigured such that the Stokes and anti-Stokes signals were seperated and fed to individual photon detectors using an additional dichroic mirror, shown in figure 4.44. To increase the anti-Stokes signal the laser power was increased to 1.5 W (in accordance with equation 4.7.2.1).

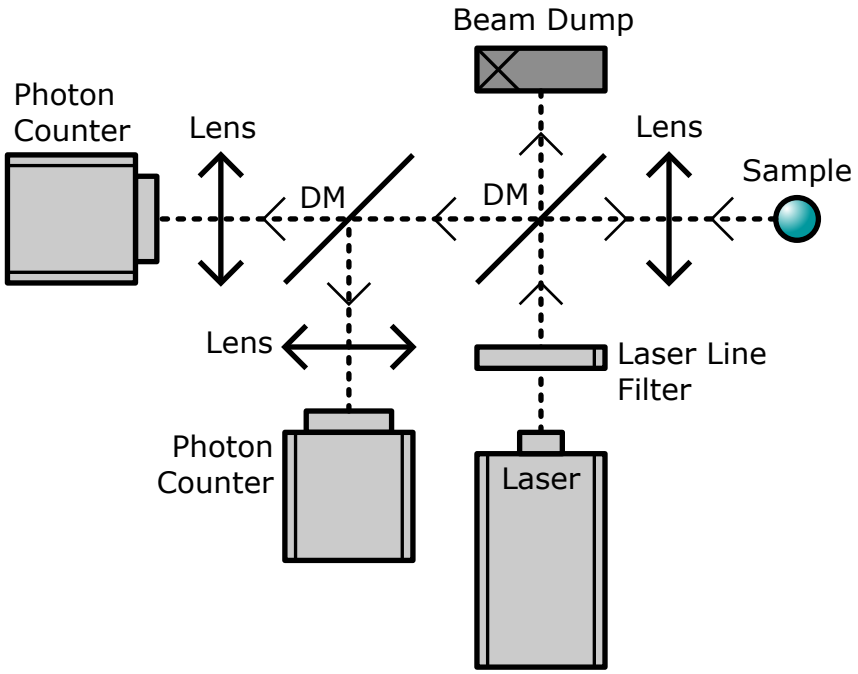

Figure 4.44: A schematic representation of an instrument to measure the ratio between anti-Stokes and Stokes peaks using photon counting. Dichroic mirrors have been marked DM. The dichroic mirror splitting the Stokes and anti-Stokes scattered light could be replaced with an equivalent combination of high and low pass filters to give the same results.

The signals from these photon detectors were then sent to a DAQ card and a LabVIEW program was developed to process the information. The second instrument, shown in figure 4.45, isolates Raman scattered light from an excitation line before splitting it into Stokes and anti-Stokes components, measuring the photon counts from each region. This overcomes problems with the weak signals associated with anti-Stokes

scattered light by integrating across the entire spectral region. An optical attenuator (Laser 2000) is used along the Stokes path, such that the counts are not saturated during a scan of the same time period and the two are comparable. Although spectroscopic function of the instrument is lost by using photon counters (PD-050-C0E, Laser 2000, UK), a far more sensitive tool is constructed for measuring the intensity of anti-Stokes scattered light. This instrument is again used in a dark room, and an additional photon counter is used to give a background reading, as the low counts associated with the anti-Stokes region of the spectrum render this method particularly sensitive.

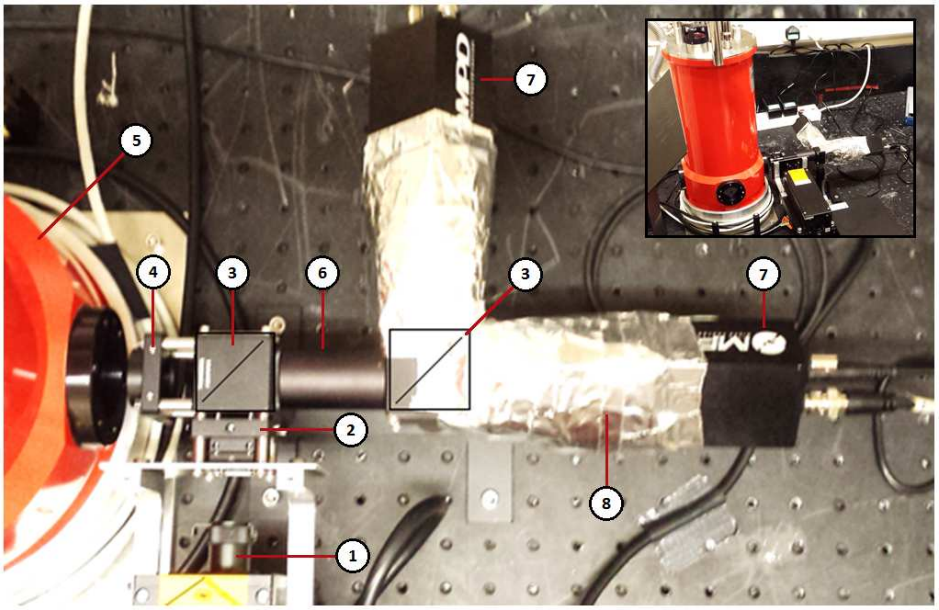

Figure 4.45: The in-house built Raman integrator (1 - Laser Module, 2 - Laser Line Filter, 3 - Dichroic Mirror, 4 - Lens, 5 - Cryostat with Sample, 6 - Bridge containing Notch Filters, 7 - Photon Counters, 8 - Enclosure).

Rapid Anti-Stokes Thermometry

Simulations and experiments were first performed to establish whether the anti-Stokes Raman peaks would be too weak to detect using the spectrometer at low exposure times. Simulations of ideal anti-Stokes spectra were generated from in-house Stokes spectra, using equation 4.7.4.7 in

the form of equation 4.7.4.8. This suggested that methods relying on the resolution of individual anti-Stokes peaks for temperature analysis, certainly using the in-house built spectrometer and short acquisition times, was not an option. Even with lengthy scan times, the anti-Stokes scattered light would be buried in the instrumental noise and manifest as too weak to detect, which was readily backed up by experimental results in which the spectra were not observed.

$$I_{\mathrm{as}} = I_{\mathrm{s}} \left(\left(\frac{\nu_{\mathrm{l}} + \nu_{\mathrm{s}}}{\nu_{\mathrm{l}} - \nu_{\mathrm{s}}} \right)^{4} \exp\left(\frac{-h\nu_{\mathrm{s}}}{kT} \right) \right) \tag{4.7.4.8}$$

Following these calculation a method to rapidly deduce sample temperature using spectral integration of both the Raman scattering regions was developed. The ratio between the Stokes and anti-Stokes signals was calculated post experiment using raw data collected using the DAQ. The program collected and saved the photons counted over the Stokes and anti-Stokes regions, along with calibration temperature readings from a Cernox sensor and a time signature. Sample temperature was then directly calculated from measurements of the anti-Stokes and Stokes Raman intensities,[162] using

$$\log \frac{I_{\mathrm{as}}}{I_{\mathrm{s}}} = A - \frac{B}{T} \tag{4.7.4.9}$$

where A and B are constants. The time resolution of the instrument was tested by lowering the exposure time for an experimental scan and testing the limits of the photon detectors and DAQ card. Figure 4.46 shows that the counts fall linearly as the exposure time is lowered, until they reach a value that does not change. This point gives us the smallest time resolution of the in-house built instrument, at ∼64 ms.

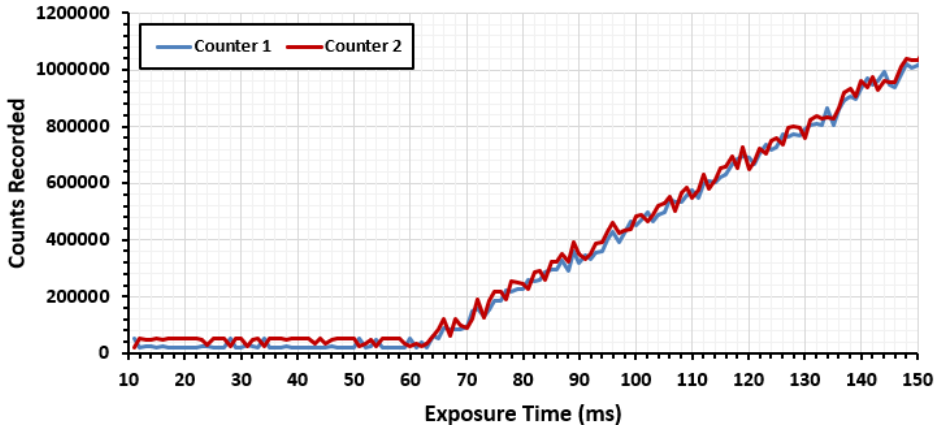

Figure 4.46: A graph to show the minimum exposure time of the in-house Raman photon counter.

Photons scattered in the Stokes and anti-Stokes regions of the Raman spectrum were counted as a sample was slowly cooled and subsequently warmed up again (shown in figure 4.47), allowing their dependance on temperature to be investigated. This used a small cryostat (TK1813, Thomas Keating Ltd, UK) holding a small bead of water in a brass mount. The slow nature of the temperature change allowed temperature to be calibrated using a Cernox sensor mounted on the brass.

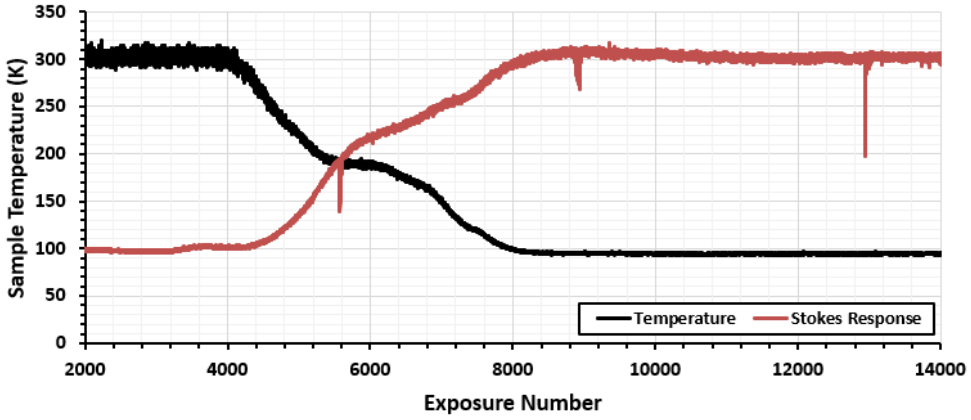

Figure 4.47: Experimental data taken during a cool down. The Stokes trace is normalized to the temperature data and also displayed, showing the increased response of this scattered light as temperature decreased.

Equation 4.7.4.9 was then used to plot the ratio between the Stokes and anti-Stokes data as a function of temperature. This is shown in

figure 4.48, displaying 4 data sets for a temperature range between ∼77 K and room temperature (this temperature limit of 77 K is simply imposed by liquid nitrogen use, and could be tested further with liquid helium). Although the plots are not linear, as expected, it can be noted that the data sets follow the same curve. This is made more noteworthy by the fact that the original Stokes and anti-Stokes counts differed significantly between experiments, possibly due to sample changes, showing that the ratio between the two is independent of fluctuations in signal intensity.

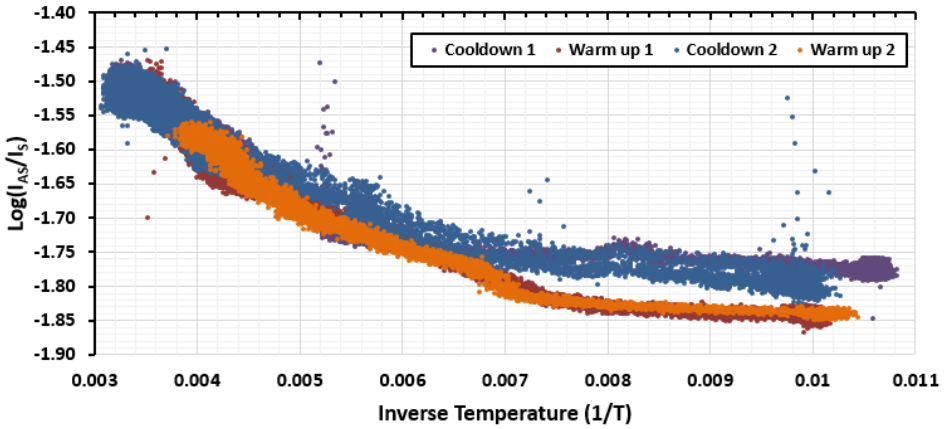

Figure 4.48: 4 independent experimental data sets, showing the relationship between $\log(I_{as}/I_s)$ and $1/T$.

This characteristic curve can then be used to calibrate temperature data taken during rapid experiments, where conventional reading methods would not give true values for the temperature at the sample. This is done by averaging the 4 curves shown in figure 4.48 and isolating the two linear sections in the low temperature region ($0.005 < x < 0.007$ and $0.007 < x < 0.01$ corresponding to the ranges between 200 K and ∼150 K and ∼150 K and 100 K respectively) and using the regression equation as a look-up-table (LUT) for the experimental data. Although the noise on the readings is significant and data is only present down to liquid nitrogen temperature, this technique gives a rapid reading of temperature with little effect on the sample.

Chapter 5

Liquid-State NMR

5.1 Resonant Circuit

A system to generate a room temperature, liquid-state sample with a highly polarized nuclear spin ensemble has thus far been described. In order to realize a high-resolution NMR spectrum, capable of delivering mid-IR radiation into the VTI, an NMR probe is required.

5.1.1 Coil Geometry

A resonant coil is required to produce a magnetic field B_1 normal to the B_0 field produced by the spectrometer, thus manipulating the highly polarized spin system and investigating the nuclear spin ensemble. The B_0 field is axial to the spectrometer bore and, accordingly, the B_1 field needs to act normal to this (in the x-y plane). A couple of geometries are available, presented in figure 5.1, with which this field may be realized.

A solenoid coil is a helical, conductive wind that behaves as an inductor when an electrical current is passed through it, with the movement of the electrons creating a uniform magnetic field within the coil volume. [163]

While solenoid coils are used for a wide variety of NMR experiments, the geometry of the system used for this project would mean that the coil would need to sit horizontally in the spectrometer bore. This would make irradiation with microwaves and mid-IR frequencies difficult, as well as causing problems during the cooling stage of the experiment, as the sample would be obstructed by the coil.

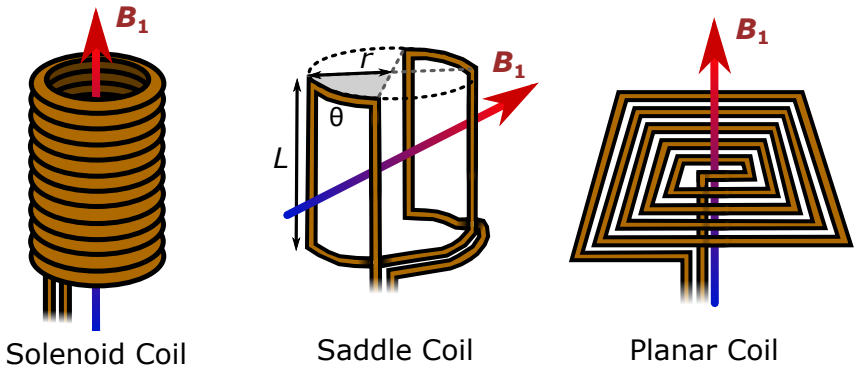

Figure 5.1: The three commonly used coil geometries for NMR.

To overcome these issues a saddle coil was used. Saddle coils use a single closed wire in a specific configuration, whereby $\theta = 120°$ and $L/r = 4$[164,165] (see figure 5.1), to create 2 separate loops which induce a uniform magnetic field in the space between them. This permits a more exposed sample to be used, with mid-IR and microwave access available from above or below the sample. The exposure of the sample also lends itself to cooling processes going on within the VTI bore, while remaining isolated from the thermal mass of the coil and probe. A final consideration was that of a planar coil,[166,167] although the suitability of this coil type for this project is limited by containment of the sample and sample size restrictions. This open nature of the coil may aid cooling, but the coil will block heating pathways, and the coil only generates a small slice in which the magnetic field is homogeneous, an issue for the high-resolution, liquid-state NMR experiment.

5.1.2 Response

A number of capacitors in series and parallel are used to tune and match the response of the coil to the resonance of the nuclei of interest at 9.4 T.[29] A rough value for this response is achieved using a static and permanent capacitor attached about 1 cm from the coil itself, situated inside the VTI. This capacitor is chosen to be a surface mount component, soldered end on to the coil such that any thermal contraction introduces the least stress to the system. This small inclusion does not introduce too high a thermal load to the sample space and ensures that the resonance is coarsely tuned prior to a cooldown.

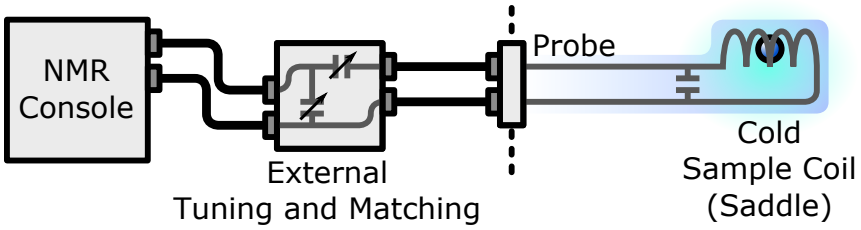

Figure 5.2: A circuit diagram to show the basic electronics of the NMR probe. In reality, low-temperature, non-magnetic semi-rigid coaxial cable is used inside the probe.

The saddle coil is then connected to a length of low temperature, non-magnetic semi-rigid coaxial cable (SS 304) running down the laser shaft sample support. This semi-rigid path is then connected to a hermetic BNC connector and passed from the VTI to the lab space where a tuning and matching board, containing two variable capacitors (see figure 5.2), is used to fine tune the resonant frequency of the coil to the sample. This board ensures that the resonant frequency of the circuit corresponds to the nucleus under test and that the circuit is impedence matched to any connecting lines,[29] usually at 50 Ω. This reduces reflected power and subsequently boosts the signal strength that can be recieved from the nuclear species. By including this board outside of the probe it is easy

to swap out capacitors, adjust the values in real time and protect the moving parts of the small components from cryogenic damage.

5.1.3 Further Considerations

Equation 1.3.2.2 from section 1.3.2 includes a proportionally factor, α, by which the measured signal relates to spin magnetization of the sample. This factor is dependent on a number of contributions such as coil temperature T_c, coil volume V_c, the resonant frequency of the spins ω_{LC}, the quality factor of the detection circuit Q and a filling factor η_c.[29]

$$\alpha \propto \sqrt{\frac{V_c Q \omega_{LC}}{T_c}} \eta_c \tag{5.1.3.1}$$

An increase in the value of α will bring about an increase in measurable NMR signal, suggesting that the system can be optimized using parameters of the coil to further improve the sensitivity of the TJ-DNP experiment. In reality, the resonant frequency, ω_{LC}, is predetermined by the magnetic field of the spectrometer and the sample under test, and the volume of the sample (and thus the volume of the coil V_c) has been chosen to be suitably small (discussed in section 2.2.1) so as to benefit the experiment during the rapid heating and cooling stages.

The increase in measurable NMR signal brought about by a reduction in probe temperature has driven the development of commercially available CryoProbes^{TM} (Bruker).[168–170] These use cryogens to reduce both Johnson-Nyquist noise and the noise associated with the resistance of conductive electronics. The probes are capable of increasing the sensitivity of the experiment by a factor of five using liquid helium[171] and any in-house built DNP probe not cooled using cryogens would need

to use the results obtainable with this state of the art technology as a benchmark. This stated, although the coil will be wrapped as closely to the sample cup as possible, ensuring the value for η_c remains as high as possible, the circular cross section of the wire will ensure that it remains somewhat thermally isolated from the sample, allowing it to benefit from a low T_c value caused by the sample cooling process. Low-temperature, non-magnetic materials are used for the coil and transmission line (silver copper and SS 304 semi-rigid coax). The low temperature mechanical properties of these materials allow them to withstand the low extremes of the experiment without breakage or dramatic thermal contraction, while a reduced thermal conductivity reduces heat flow into the space.[100] Non-magnetic materials that have a magnetic susceptibility matched to the surrounding environment are desirable and used so as to reduce field inhomogeneities.

5.2 Practical Considerations

Although NMR probes are readily available for a number of applications, this project requires a bespoke probe body to couple to the hardware developed specifically for use in Nottingham and overcome a number of complications imposed by the TJ-DNP experiment design.

5.2.1 Heating Path

As well as detecting the NMR signal from the sample, the probe needs to deliver the mid-IR radiation detailed in Chapter 4 to the sample while keeping heat flow into the VTI at a minimum. The simplest solution to satisfy these requirements is to use a long, hollow tube made of thermally insulating, reflective material. This tube is made from SS-316L for its superior low temperature characteristics and magnetic susceptibility, and has an inner diameter of 6 mm and and outer diameter of 8 mm. This supports the sample in the homogeneous region of the magnet, while creating a free space path for the laser to be delivered. This shaft may also allow a gold plated hollow waveguide to be inserted, improving laser transmission to the sample. An anti-reflection coated barium fluoride vacuum window, with a transmission quoted to be ∼98% for mid-IR radiation at 2.94 µm, is used to pass the mid-IR radiation into the evacuated sample environment.

5.2.2 Pumping Access

High throughput pumping is required via the NMR probe, as coupling for pumping lines is unavailable on the VTI itself (see section 3.2.4). This means the NMR probe needs to couple to a large diameter pumping line and exhibit low flow path resistance between this connection and

the sample space. This is achieved by both integrating a custom high-throughput vacuum T-junction (shown in figure 5.3) and by minimizing the bulk probe design, removing all material other than a central laser shaft and necessary NMR electronics. This shaft supports the sample such that it is at the right distance within the magnet, but does not obstruct the flow path. Although this fixes the sample within the homogeneous region of the magnetic field, the reduction of the probe to a central shaft increases the likelihood of lateral sample movement, meaning that it could sit off-axis to the magnet bore. Thin baffles are used periodically along the shaft, 150 mm apart, with a diameter of 22 mm to match the inside of the VTI and keep the sample centralized. These are drilled so as to minimize flow path resistance and allow NMR electronics to run alongside the shaft.

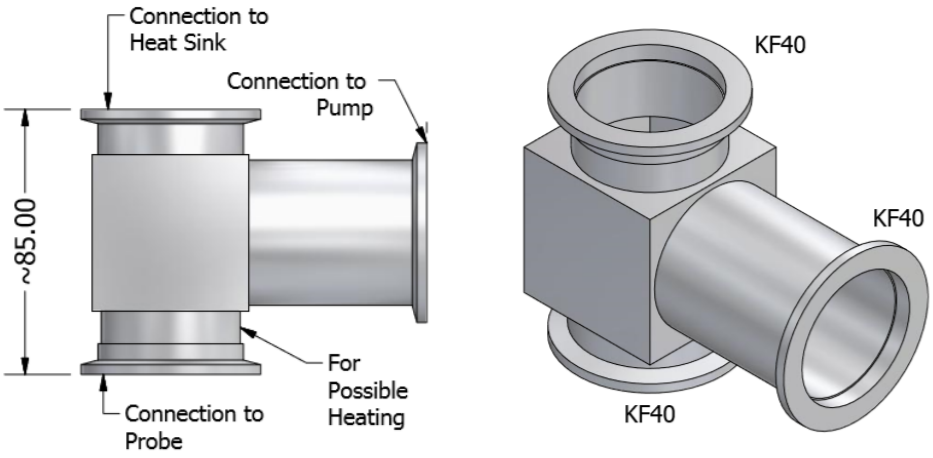

Figure 5.3: A CAD representation of the custom T-junction designed for use with the bespoke NMR probe to allow high-throughput pumping. This junction features KF40 connectors, a thinner walled region around which wire can be wrapped for protective heating and is shorter than stocked components to ease size contraints (section 5.2.3). Dimensions are given in millimeters.

It is also important that any vacuum seals used in this design are not compromised by any cooling caused by low temperature helium flow. Where possible, practical and necessary, knife edge seals with superior low temperature capabilities[100] are used instead of rubber O-ring seals.

Indium knife edge seals are used where hardware is joined permanently, and copper seals are used where components are expected to come apart on rare occasion. In locations where knife edge seals are not practical, such as couplings that are connected and disconnected frequently, additional measures are used alongside the O-ring seals to reduce the risk of cooling damage. These are realized both in an active and passive manner, introducing the ability to heat the region or by including heat sinks between the vulnerable connections and the cryogenic space, respectively. These methods are illustrated in figure 5.4. These methods can offer variable amounts of relief by either altering the physical dimensions and materials of the heat sink or by increasing active heating. Care must be taken to ensure that the temperature inside the VTI is not raised by these protective methods.

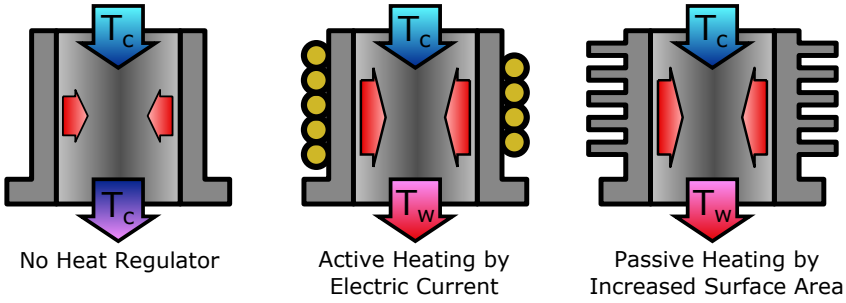

Figure 5.4: Heat sinks are used, alongside resistive heating, to decrease the chance of damage to vacuum seals along the helium flow path.

5.2.3 Size Constraints

The length from the base of the magnet to the homogeneous region of the spectrometer is 485 mm, as listed in figure 2.11, with the shim hardware increasing the length that the NMR probe needs to be to locate the sample in the right place by an additional 134 mm. This already requires a shaft of length 619 mm to be used, but it is from below this

height that all pumping, heating, NMR and thermometric hardware must be implimented. Seeing as the height avaiable underneath the spectrometer is 1050 mm, minus the 134 mm protrusion of the shim hardware, no probe longer than 916 mm will be loadable into the VTI. This upper limit means that all hardware introduced by the NMR probe must be included within the remaining 297 mm, a restriction that requires considerable design work to satisfy.

To begin, sheathing components such as the heat sink over the probe body during loading effectively increases the clearance below the spectrometer by removing their length from the base of the cryostat and adding no extra length to the probe. To further increase this clearance the probe has been designed such that it breaks apart, with the sections rejoining after the top has been partially inserted into the VTI bore (see figure 5.5). Not only does this ease problems associated with clearance, but also introduces macroscopic thermal breaks to the probe and increases the ability to modify the hardware at a later date. This break is introduced towards the top of the probe, with a removable probe extension and probe tip designed to hold the sample cup and NMR coil. This extension was initially made out of stainless steel, but was updated to Macor^{TM} for reasons described in section 5.4. A Cernox sensor is fixed on this tip so as to provide an idea of sample temperature, close enough to give an accurate indication of the sample temperature while ensuring the NMR signal and thermal behaviour of the sample are unchanged by the inclusion. The NMR electronics include a break along their length in order to allow the probe and tip to be separated. These breaks are facilitated using small SMA connectors which fit in the cryostat bore alongside the laser path.

5.3 The Probe Design

5.3.1 Overview

A 400 MHz proton saddle coil with a diameter of 6 mm and a length of 24 mm was initially created to fit around the sapphire sample cup, featuring a 2.4 pF coarse tuning capacitor ∼10 mm below the coil and external tuning and matching via variable capacitors on a board outside of the instrument. This was chosen to allow easy testing of the hardware and as a step towards construction of ^{13}C hardware, which requires another coil to perform cross polarization and probe the species. The coil and sample are supported in the homogeneous magnetic field of the spectrometer by a tube with an inner diameter of 6 mm and an outer diameter of 8 mm which features periodic baffles to keep the sample axially centered within the VTI. A removable extension tube and probe tip allow precise positioning of the sample, easy modification of the hardware and insertion under the conditions of limited space. Fine adjustment of the sample height can be performed by altering the dimensions of the probe extension. A schematic of the NMR probe is presented in figure 5.5. The probe base facilitates NMR, thermometry and mid-IR heating, as well as allowing high throughput vacuum access. A passive heat sink is included to protect any rubber vacuum seals on the base of the probe from the flow of cold helium. This sits above a custom built T-junction which features a thinner walled section for active heating of the column with resistive wire. To overcome problems associated with the limited space below the spectrometer, both the heat sink and the custom T-junction are attached to the probe prior to insertion, rather than to the base of the VTI. A laser window at the very base of the probe allows delivery of the mid-IR radiation without compromising the vacuum.

5.3.2 Probe Schematic

A fully labelled schematic of the NMR probe is presented in figure 5.5 such that all aspects of the design can be clearly identified. Reference images and technical drawings of the probe can be found in section 5.3.3, along with dimensions.

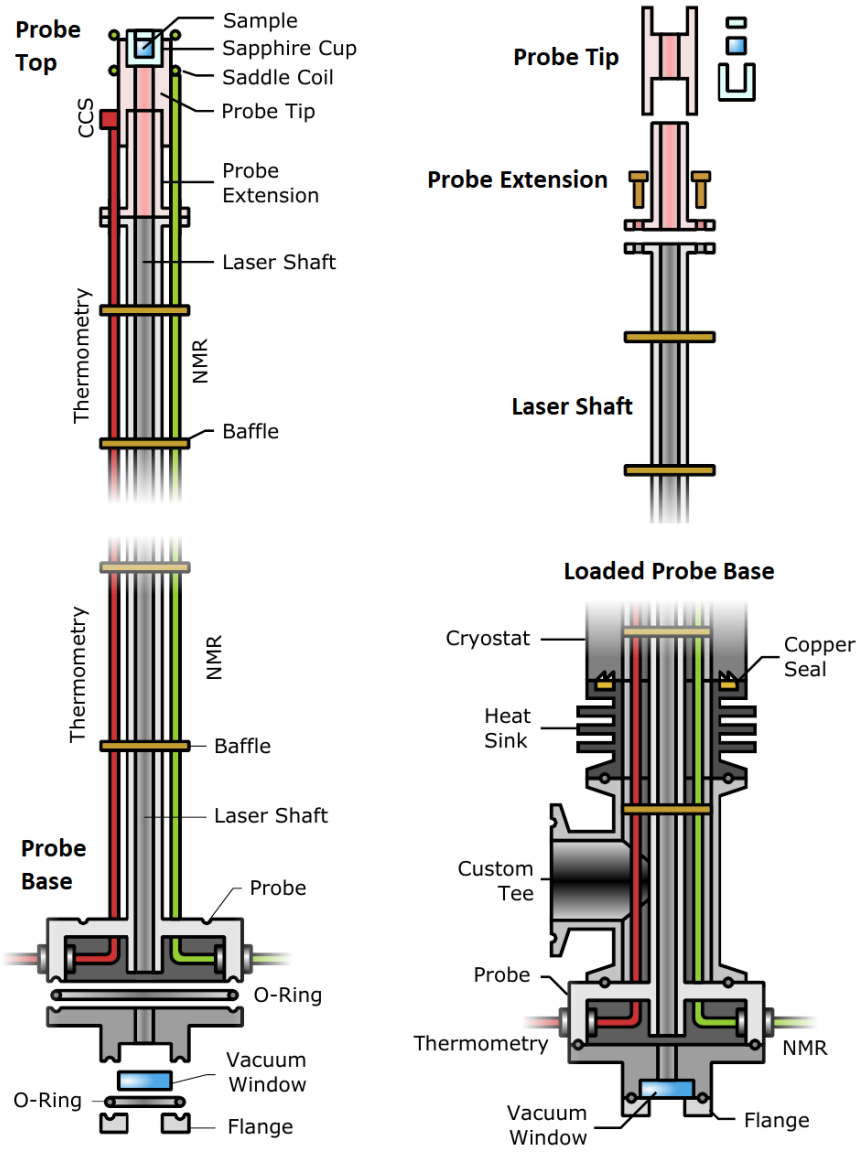

Figure 5.5: A schematic of the NMR probe, showing both the top and bottom sections of the design. The sapphire sample cup sits in a separate probe tip, which in turn sits on top of a probe extension. This is to ease probe entry, reduce heat flow into the sample space and to allow for easy iterative alteration of the design. The base of the NMR probe supports a custom vacuum T-junction and a heat sink. The heat sink is connected to the cryostat via a knife's edge seal.

5.3.3 The NMR Probe

The backbone of the NMR probe itself is a hollow, stainless steel tube with an inner diameter of 6 mm and an outer diameter of 8 mm. This tube supports the sample in the homogeneous magnetic region of the spectrometer and forms a free space optical path for mid-IR radiaition. At the top of the tube is an extension shaft (figure 5.6), reducing heat flow into the sample space and allowing careful positioning of the sample, and an NMR probe tip with a coil and temperature sensor (figure 5.7).

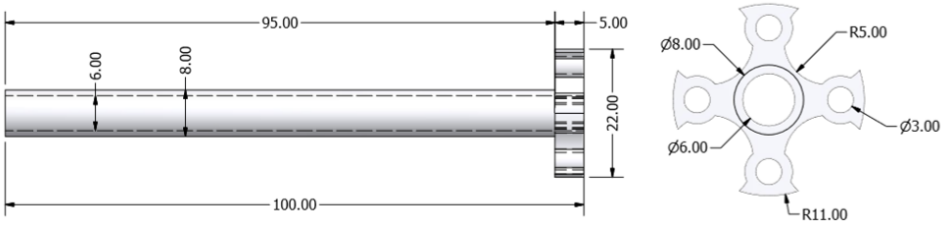

Figure 5.6: An example of an extension shaft for the NMR probe, with all measurements in millimeters. This particular design was made out of Macor to reduce the linewidths associated with hardware made using stainless steel, an issue that is documented in section 5.4. The footprint of the extension is shown on the *right*.

Both of these are removable and adjustable, with the extension screwing into a connector at the top of the shaft and the probe tip being fixed to the extension in turn by a grub screw.

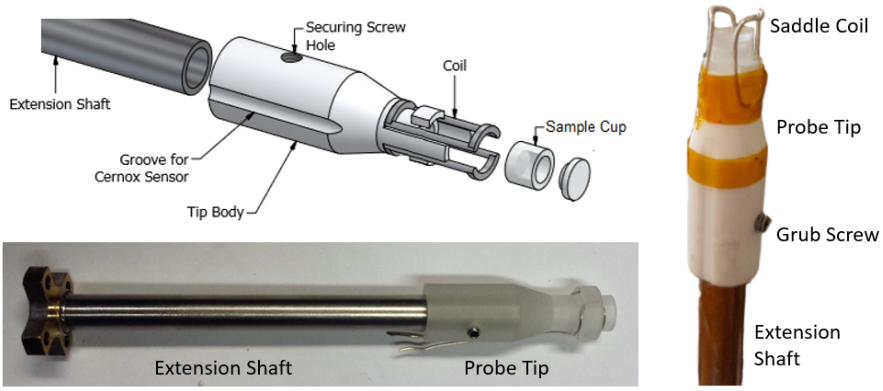

Figure 5.7: The probe tip, holding the sample cup and NMR coil, is screwed onto the extension shaft. The image at the *bottom* shows an older design of the tip, whilst the updated image on the *right* shows the final design. The Cernox sensor is attached using cryogenic tape.

The coil is then connected to a semi-rigid coaxial NMR transmission line running along the length of the probe using an SMA connector to the base of the ensemble, shown in figure 5.8. This base features a heat sink, 90 mm in length, for passive thermal protection of the rubber O-rings on the NMR probe, and a custom T-junction which has been described in section 5.2.2. The main probe body features an electronic Fischer port for thermometry and two possible ports for NMR electronics (for ^{1}H and ^{13}C NMR). A mid-IR transparent window is included in the very base of the ensemble, kept in place using a flange which couples to both the free space optical path underneath the spectrometer and the laser safety interlock electronics.

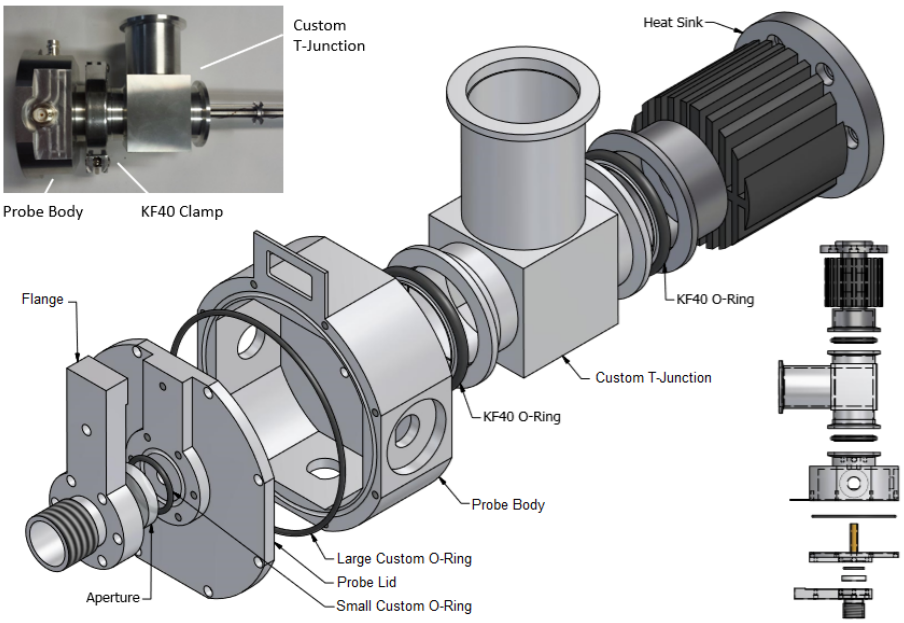

Figure 5.8: The bottom of the NMR probe, showing the heat sink, custom T-junction and main probe body. The base of the NMR laser shaft is screwed into the top of the probe body, such that the T-junction and heat sink do not contribute to the overall length of the probe.

Because of the inclusion of the extension tip into the modular probe design, the total length of the NMR probe and the shaft itself does not need to be precisely matched to locate the sample in the homogeneous magnetic region of the spectrometer, and simply needs to be loaded into

the base of the VTI. Figure 5.9 shows the NMR probe base with the support shaft attached, giving an indication of length. To load the probe, the NMR probe tip is attached to the extension shaft and lifted temporarily into the VTI, after which the probe base and shaft can be placed underneath them within the bore. The extension shaft can then be lowered and screwed onto the laser shaft, and the SMA couplings connected to link the NMR coil to the external electronics. Following this the entire probe can be inserted into the VTI and the 6 screws connecting the heat sink to the base of the VTI can be tightened securely. At this stage the NMR probe is loaded and can be coupled to the optical path, further NMR electronics and the high throughout vacuum line.

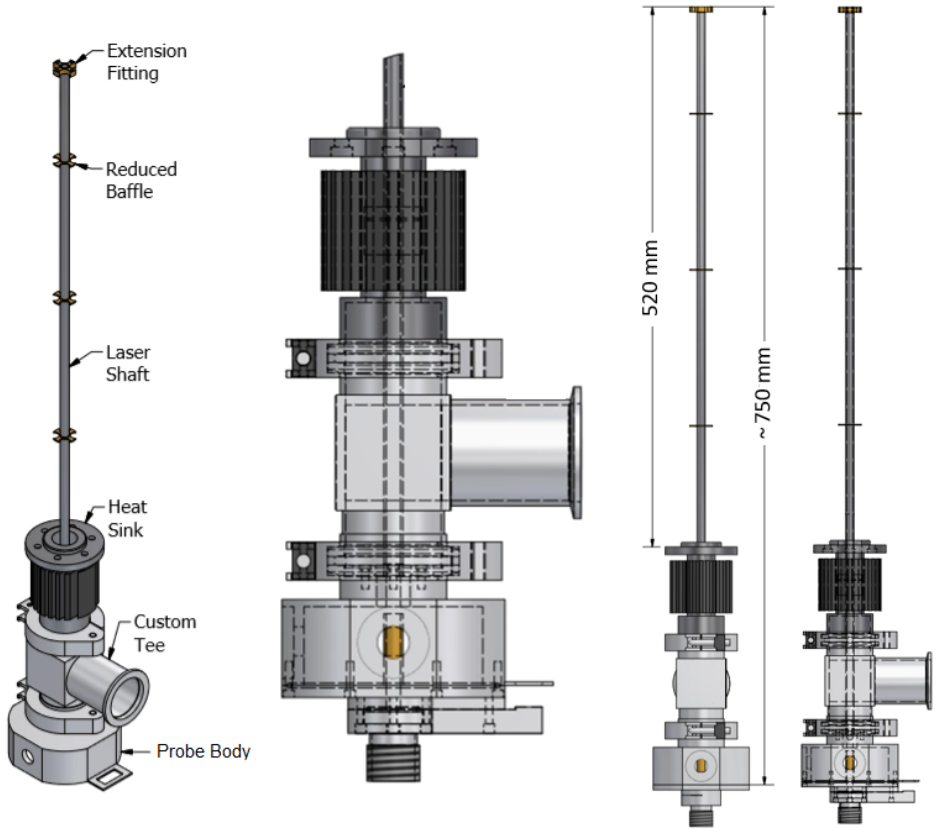

Figure 5.9: The NMR probe assembly showing overall length and appearance. This diagram shows the assembly without the probe extension and tip attached, as the probe would be loaded into the VTI.

5.4 Initial Tests and Validation

Basic Function

The NMR capability of the bespoke probe could be tested once the VTI had been constructed and installed in the spectrometer, and initial tests proved the basic function of the probe by comparing the proton signal received from an empty sample cup and that containing distilled water. Although a clear water peak could be seen, verifying the basic function of the probe, the signal experienced broadening and had a FWHM linewidth of the order of thousands of Hertz. It should be noted that the preliminary nature of this investigation with a pure H_2O sample will feature excessive broadening through radiation damping. In reality a H_2O/D_2O mix could be used to suppress these effects and realize linewidths ~ 50 times narrower.

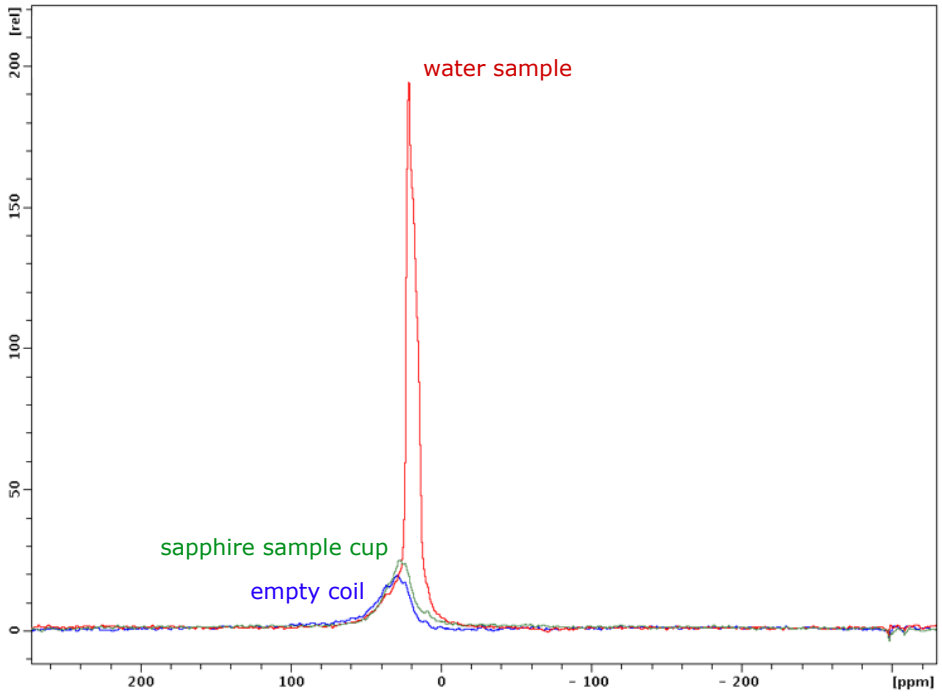

Figure 5.10: The first NMR spectra collected using the novel probe. The blue signal is from an empty coil, the green is from an empty sapphire sample cup and the larger, red signal is from the cup filled with water. The background signal is believed to be from cryogenic tape on the probe head at the time, which was later removed. This investigation into function and NMR linewidth uses an arbitrary reference scale.

Following this simple test, the current supplied to the external shim coils was increased in order to compensate for any effects on the field homogeneity within the bore brought about by the probe, in an effort to improve the linewidth. This method improved the linewidth of the pure water peak to ∼150 Hz (∼0.35 ppm), shown in figure 5.11, however the currents required for this were suspiciously large and other stratagies to decrease the linewidth of the spectra by directly improving the design of the probe were explored. The strong response of the linewidth to the external shims suggested that the magnetic properties, such as susceptibility matching, could be improved in the sample space.

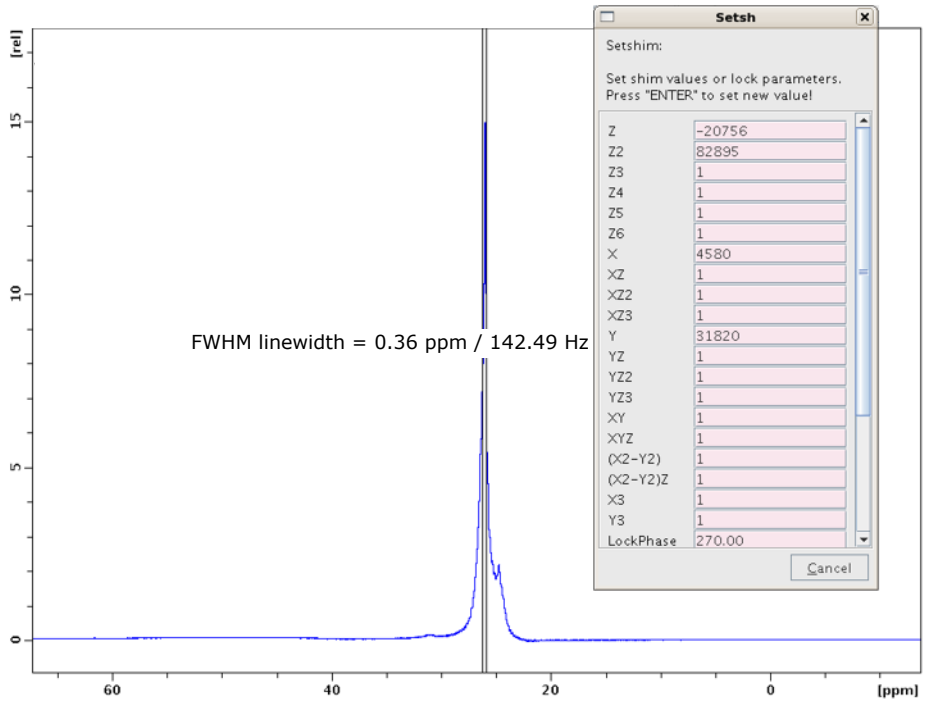

Figure 5.11: A figure to show how the linewidth of the water signal from early tests could be decreased by over an order of magnitude (from ∼8000 Hz to ∼140 Hz) by applying large shim currents. The large shim currents are also indicated in this figure.

Probe Development

As detailed in section 3.2.3, materials with poorly matched magnetic susceptibilities degrade magnetic field homogeneity within the spectrom-

eter bore and broaden NMR spectra. Although efforts were made to reduce susceptibility mismatching when designing the NMR probe, a compromise was initially made over the the probe tip extension, which was made from low χ value stainless steel to behave as a continuation of the mid-IR waveguide. Replacement of this tip with a ceramic, Macor^{TM} tip, gave rise to a drastic decrease in NMR linewidth from ~150 Hz to ~60 Hz. Furthermore, although this material does not dramatically influence the illumination of the sample, it does decreases heat flow into the space, as the thermal conductivity through Macor^{TM} is far lower than that through the steel. Further investigation found that the semi-rigid coaxial cable used on the probe was ordered in error and was magnetic. This meant that field distortions existed close to the coil and, once this was swapped for non-magnetic cable, a linewidth of ~8 Hz (~0.02 ppm) was achieved.

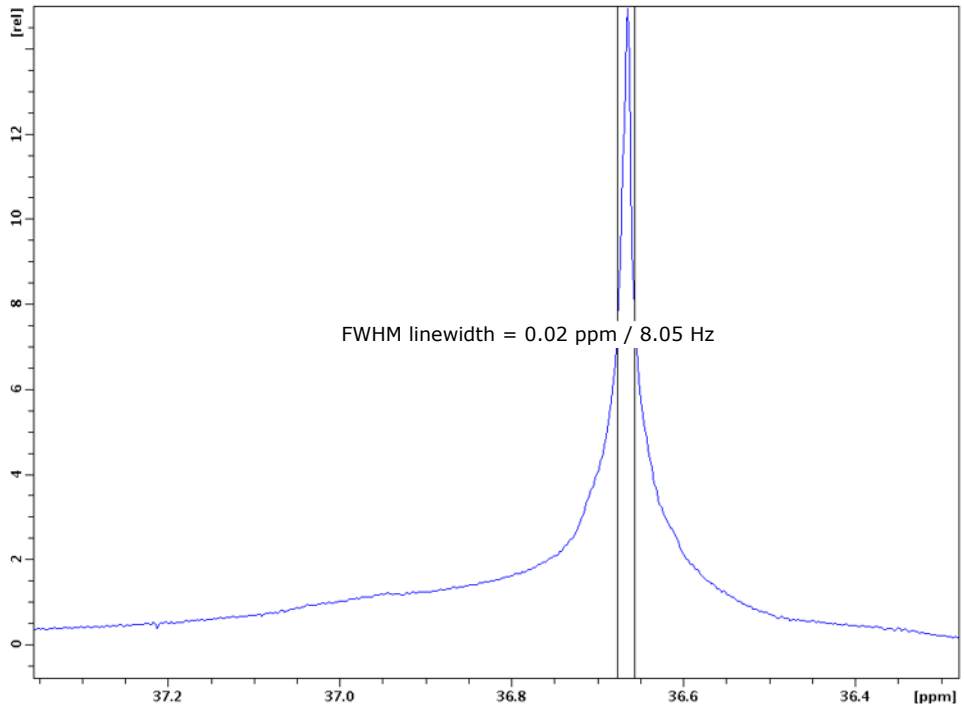

Figure 5.12: After the stainless steel probe extension was swapped out for Macor^{TM} and the erroneous transmission line was changed an NMR signal with a linewidth of ~8 Hz was seen.

While this linewidth may be decreased further by making a larger fraction of the the probe shaft from Macor^{TM} instead of stainless steel, the effects will decrease as distance increases. This experiment may suffer from unavoidable linewidth broadening from the increased hardware presence within the bore, for which the existing shim coils would not have been designed. The metallic microwave guide comes close to the sample from above and the annulus of helium apertures which spray helium into the VTI is designed to be at a different height than the sample. These factors create asymmetry around the sample, increasing the spread of nuclear Larmor frequencies within it and broadening the spectra. As a result, a peak of $\sim$8 Hz is a fair linewidth to achieve for this project.

Chapter 6

Discussion

As this thesis draws to a close, the work will be summarized and put into context of the original aims and objectives of the project and immediate avenues for further work will be proposed.

6.1 Overview of the Project

A number of large scale hardware solutions have been designed, developed and tested so as to meet the criteria to successfully facilitate the TJ-DNP experiment, including a bespoke VTI to reach temperatures down to 1.75 K, a mid-IR laser path to deliver heat energy to a low temperature sample within the VTI and a NMR probe such that enhanced liquid-state spectra can be received from the set-up. Along with a high-field spectrometer and microwave bridge, these instruments have been designed to fit together in a manner shown in figure 6.1. All elements of the experiment were designed with a modular focus, allowing instruments to be easily improved at a later date or other design elements to be included with little disruption to the system as a whole. The design allows the helium flow that cools the sample to be stopped during the rapid heating stage of the experiment.

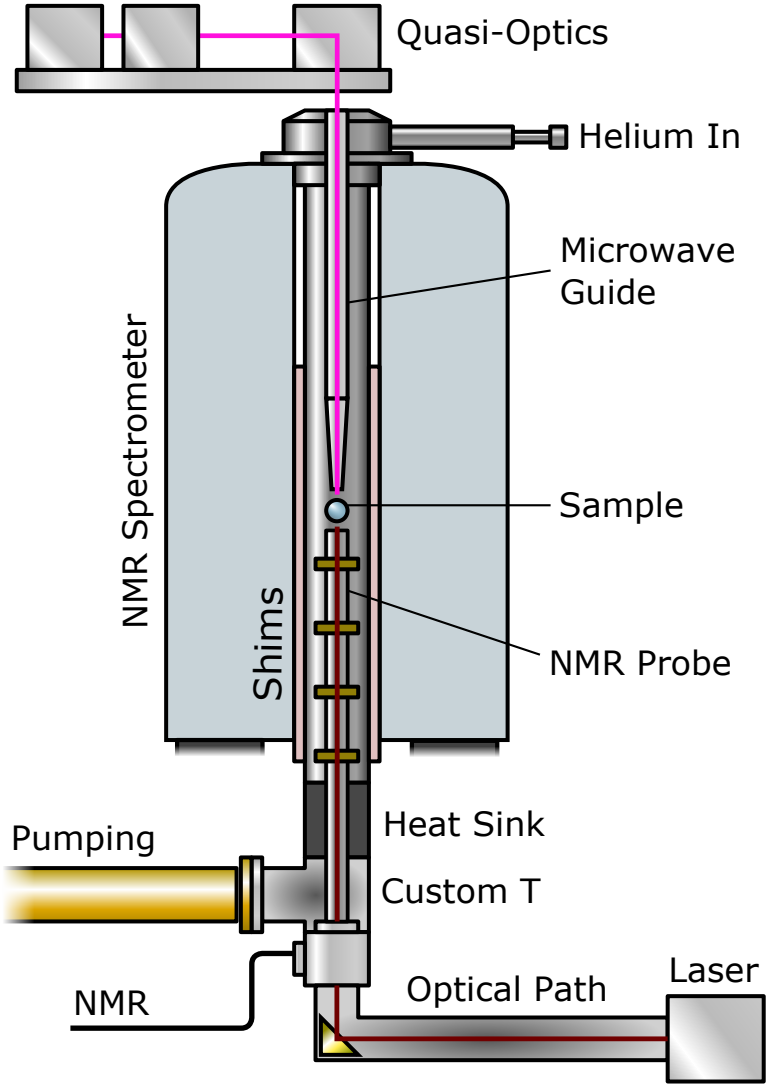

Figure 6.1: A diagram to show how all of the hardware aspects of this project come together.

6.1.1 Summary of System Tests

Low Temperature Environment

A large scale, bespoke cryostat has been designed, called the VTI. Furthermore, the experimental procedure to reach low temperature has been improved, bringing initial cooling times down by a factor of ∼4, achieving lower base temperatures with less liquid helium and ensuring the VTI is protected against cryogenic leaks. The instrument is capable of reaching a stable base temperature of 1.75 K in ∼2.5 hours with a

bespoke NMR probe loaded, and can be held at this temperature for a time period of at least 15 minutes. This stable low temperature allows polarization build up for the experiment and the overall timescale for this cooldown is promising for a TJ-DNP experiment between T_{DNP} of 1.75 K and a T_{NMR} of ∼300 K.

Microwave Irradiation

A microwave bridge has been designed and built by Thomas Keating Ltd. and installed above the magnet, with the ability to move in and out of the experimental space and align precisely with the custom microwave hardware within the VTI. The height and position of the microwave bridge above the magnet has been measured and fixed to give repeatable irradiation. Microwave generation and delivery has been tested and documented, delivering ∼25 mW of stable, circularly polarized microwave irradiation at 263 GHz to the sample space. This value accounts for the losses through the system, which were measured to total ∼3 dB (through both the bridge and the waveguide).

Rapid Heating

Calculations have been performed, considering appropriate sink processes within the experimental space, which show that a 30 W, Er:YAG laser can provide the heat energy required to bring the sample used for this TJ-DNP experiment from ∼1 to 300 K in just under 2.5 seconds, a timescale suitable for molecules with moderate relaxation times. This rapid heating mechanism has been implemented, tested and, although further work is required to increase power delivery, an optical system to deliver this energy into the VTI has been established. Initial research ruled out fibre optics as a suitable method of transmitting such high pow-

ered radiation into a low temperature cryostat, as mechanical properties, size constraints and damage thresholds forbid this. Instead, two free space optical paths have been tested, with overall losses through lenses and appertures characterized at ∼5% in the best case. A transmission solution involving three lenses was devised, collimating the diverging beam and directing it up the bore of the VTI using a gold mirror. A further lens pair could then focus and manipulate the beam diameter such that it was matched to the sample size. Although some sample heating was achieved, this method suffered from heavy degradation of the beam with any slight misalignment and the law of optical invariance suppressed power delivery along the sample support. Alternatively, a magnifying lens was used to project an enlarged image of the laser aperture into the VTI, in which a waveguide could be used to homogenize and direct the beam to the sample space with low losses. This method was easier to align due to the reduced optics and shows promise for the rapid heating stage, but was still being investigated and developed as this project came to a close (see section 6.2.2 for further work).

NMR Capability

An NMR probe and ^{1}H saddle coil have been developed and tested to allow mid-IR radiation into the VTI bore, whilst providing high throughput pumping access, sample thermometry and introducing minimal heat load into the sample space. This probe has been shown to collect the NMR signal associated with distilled water, and improvements in material choice and probe design have improved the linewidth of the signal by 3 orders of magnitude to ∼8 Hz. This process has been accelerated by the modular nature of the design, with the separate probe tip, probe extension and probe body all offering easy modification.

6.1.2 Additional Investigations

Raman Thermometry

A couple of Raman thermometry techniques were developed, capable of remotely measuring sample temperature with little effect on the temperature itself. The results from a home-built spectrometer gave similar results, albeit with a lower signal intensity, to a commercially available system, and temperature dependent shifting of the signal associated with the O−H stretching bond was observed. Although this allowed temperature to be monitored, the shift was noted to stop at the glass phase transition temperature of the mixture (∼220 K) as the hydroxyl bonds became frozen in place. To monitor lower temperatures an alternative thermometry method was devised and built, comparing the minuscule anti-Stokes signal to the Stokes signal. This allowed rapid (∼65 ms exposure time), remote thermometry between ambient temperature and that of liquid nitrogen, using a calibration table.

Nanoparticle Heating

Gold nanoparticles, 5, 12 and 30 nm in diameter, were added to water at a fixed concentration of 10^{16} particles ml^{-1} to investigate their effects on the relaxation characteristics of the NMR experiment. Differences in the spin relaxation times between samples were minimal when compared to a control sample of pure water, indicating that they may be included into the sample without drastically affecting the NMR signal. However, the ability of these nanoparticles to heat a macroscopic sample using localized surface plasmon resonance (LSPR) showed any heating effects caused by the particles to be insufficient for the TJ-DNP experiment at Nottingham.

6.2 Areas for Further Work

Due to the vast scale of this project and a number of unexpected practical challenges and delays during the design and development work, a full TJ-DNP experiment has not yet been performed. Despite this, considerable progression towards the experiment at Nottingham has been made and, aside from this central objective, a number of additional investigations have opened up exciting avenues for further work.

6.2.1 The Temperature-Jump DNP Experiment

The most exciting candidate for further work is completion of the TJ-DNP experiment itself. At this stage, with the VTI able to reach 1.75 K, the microwaves working, the heating path able to deliver mid-IR radiation (albeit at a reduced power) and the NMR probe responsive to the sample, it should be possible to piece all of the hardware together and perform a TJ-DNP experiment. Ideally this should be put together in stages, allowing for easier diagnostics when connecting particular aspects of the hardware. To begin, the ^{1}H probe could be upgraded to a ^{13}C probe and it should be possible to use the VTI and microwave bridge to observe solid-state DNP effects and microwave irradiation of the sample. This would allow polarization build-up times and transition characteristics to be investigated, validating this initial stages of the system. Once this experiment has been completed the sample may be irradiated using the mid-IR laser and a TJ-DNP experiment can be performed. Although the heating stage of the experiment may be slower than originally desired, due to issues connected with laser output power, these investigations should still offer an increase in signal intensity when using molecules with longer polarization lifetimes.

6.2.2 Optical Optimization

A succesful design for an optical path was developed, delivering a mid-IR laser beam into the VTI to couple heat energy into a sample and cause a notable rise in sample temperature. This stated, the overall temperature rise was smaller than expected due to a number of experimental complications identified as work progressed, resulting in lower power delivery to the sample. The first notable issue is associated with a limited current supplied to the laser head, causing a subsequent drop in laser output. This was not a problem in the earlier stages of the project when the laser module was next to the control unit, and was first observed when the two were separated. Although efforts were made to contact suppliers and implement high-capacity cables, neither solved the reduction in maximum current supply from 200 A to 160 A. In order to continue with the project this reduction was accepted, but noted to limit laser output power by about a third, a factor needing improvement.

A further improvement to the system would be to use a gold plated mid-IR waveguide inserted into the NMR sample support. Developments in this area occurred within the closing stages of the project, leaving little time to investigate the benefits of using these components. Testing was performed externally using polished stainless steel tubes which, although showing promising transmission characteristics themselves, are suggested to have inferior transmission to gold coated waveguides.[157] It is believed that this inclusion should introduce an improvement in transmission by both bridging the macroscopic breaks along the NMR shaft and through the superior reflective properties of gold, translating to a more rapid temperature rise for the sample and a greater attainable TJ-DNP enhancement.

6.2.3 Temperature-Jump Documentation

The Raman thermometry work that occurred in the first year or so of the project, although culminating in a rapid thermometry technique capable of reading temperatures down to 77 K, was not fully tested as the decision was made to move on to crucial TJ-DNP hardware design and building stages. Despite this, it would be desirable to observe dynamics that would allow the heating process to be better controlled at a later stage. Further work could develop the second thermometry technique created during this project, using the ratio between Stokes and anti-Stokes scattered light, by generating a calibration curve down to 1.75 K and increasing the experimental data set to quantitatively assess and reduce reading error.

Although nanoparticle LSPR could not offer any significant heating for the TJ-DNP experiment, the ability for nanoparticles to act as sensors may allow them to be used for thermometry.[172] Doping a sample with a moderate concentration of gold nanoparticles could allow signals to be received back with characteristics dependent on temperature. A possible drawback to this method may be that, while temperature-jumps on pure water samples could be investigated this way, the particles may still have a detramental effect on the DNP experiment. This stated, a dummy sample of water doped with nanoparticles could be used to develop a heating stage that could then be implemented for undoped DNP samples. It has also been shown that a characteristic, temperature dependent shift may be measured using NMR.[173] This method provides an additional technique for thermometry that is already in place and easy to observe. This was not used in the early stages of the project as the instrumentation with which to perform NMR had not yet been designed or built.

6.3 Outlook

It has been speculated that, even now, the field of Rapid-ΔT DNP is in its infancy.[44] Experiments that provide such enhancements in liquid-state NMR may have a great impact in the vast fields of chemistry, biology and medicine. Likewise, the limitations of the technique are not yet fully understood, with DNP theory still evolving and hardware being constantly developed to improve various aspects of the method. As it stands, implementing these new hardware solutions is not inexpensive or quick, making it a high-risk, high-reward venture.

Although the full TJ-DNP experiment at Nottingham has not been performed, this project forms a sturdy platform upon which a little further work should yield results within half a year or so. All aspects of the experimental hardware have been designed, developed and built, with each separate element tested and documented to function as required. Results from the tests so far allow quantification of the maximum possible enhancements achievable using this system over conventional, 300 K NMR experiments and two characteristics, initial cooldown time and sample heating time, are primarily responsible for the success of the experiment. The maximum enhancement from the DNP process itself, $\varepsilon_{\mathrm{DNP}}$, given by equation 1.3.4.1 can be calculated as 660 for the proton and 2600 for carbon-13. This enhancement is further boosted by performing DNP at low temperature and NMR acquisition at $\sim$300 K. Taking the reasonable base temperature of $\sim$2 K achieved by the VTI designed for this experiment and using equation 1.3.4.2 allows an updated enhancement of nearly $\varepsilon^{\dagger} = 100,000$ for the proton and $\varepsilon^{\dagger} = 390,000$ for ^{13}C to be calculated. Bearing in mind that a conventional, 300 K NMR experiment would benefit from signal averaging over the course of the

TJ-DNP experiment, and that the VTI at Nottingham takes 2.5 hours to reach base temperature (which is by far the dominating time factor), a conventional experiment could benefit from boosts in signal of around 100 times during this period. As a result it is fair to divide these $\varepsilon^{\dagger}$ values by this factor to make the two methods comparable, giving our novel experiment a comparitive enhancement of 1000 for ^{1}H and 3900 for ^{13}C over conventional experiments before heating. It should be noted that this enhancement will never be realized, as it is that theoretically obtainable with an infinitely short temperature jump. The fastest temperature rise estimated for the hardware used in this experiment was ∼2.5 s and, with less than 5% total losses through the best optical system adding only a fraction of a second more, the total melt time can be assumed to be around 2.6 s. Accounting for spin relaxation and using a molecule with a T_1 on the order of seconds, it would be fair to suggest that ∼40% of the total enhancement $\varepsilon^{\dagger}$ could be preserved, provided NMR acquisition occured immediately as the sample reached 300 K. This then gives an overall, substantial and measurable enhancement from our novel system, comparable to a conventional 300 K NMR experiment running for the same period of time, of ∼400 for the proton and ∼1500 for carbon-13.

The intrument developed thus far suggests that, using molecules with moderate to long relaxation lifetimes, TJ-DNP should be possible using the system in Nottingham and should improve considerably on the enhancement values reported to date. Furthermore, performing this TJ-DNP on a sample *in situ* should open the technique up to multidimensional spectroscopic techniques. I look forward to the work that has gone into this project being built upon to realize an enhanced liquid-state NMR experiment via TJ-DNP.

References

[1] Becker, E. D. A Brief History of Nuclear Magnetic Resonance. *Analytical chemistry* **65**, 295A–302A (1993).

[2] Walker, J. *Fundamentals of Physics* (John Wiley & Sons, 2008).

[3] *Nobel Lectures - Physics 1942-1962* (Elsevier Publishing Company, 1964).

[4] Breit, G. & Rabi, I. Measurement of Nuclear Spin. *Physical Review* **38**, 2082 (1931).

[5] Fox, M. & Rabi, I. I. On the Nuclear Moments of Lithium, Potassium, and Sodium. *Physical Review* **48**, 746 (1935).

[6] Rabi, I. I., Millman, S., Kusch, P. & Zacharias, J. R. The Molecular Beam Resonance Method for Measuring Nuclear Magnetic Moments. The Magnetic Moments of $_3Li^6$, $_3Li^7$ and $_9F^{19}$. *Physical Review* **55**, 526 (1939).

[7] Purcell, E. M., Torrey, H. & Pound, R. V. Resonance Absorption by Nuclear Magnetic Moments in a Solid. *Physical Review* **69**, 37 (1946).

[8] Bloch, F. Nuclear Induction. *Physical Review* **70**, 460 (1946).

[9] Arnold, J. & Packard, M. Variations in Absolute Chemical Shift of Nuclear Induction Signals of Hydroxyl Groups of Methyl and Ethyl Alcohol. *The Journal of Chemical Physics* **19**, 1608–1609 (1951).

[10] Carr, H. Y. & Purcell, E. M. Effects of Diffusion on Free Precession in Nuclear Magnetic Resonance Experiments. *Physical Review* **94**, 630 (1954).

[11] Overhauser, A. W. Polarization of Nuclei in Metals. *Physical Review* **92**, 411 (1953).

[12] Prisner, T. & Köckenberger, W. Dynamic Nuclear Polarization: New Experimental and Methodology Approaches and Applications

in Physics, Chemistry, Biology and Medicine. *Applied Magnetic Resonance* **34**, 213–218 (2008).

[13] Carver, T. & Slichter, C. Polarization of Nuclear Spins in Metals. *Physical Review* **92**, 212 (1953).

[14] Lauterbur, P. C. ^{13}C Nuclear Magnetic Resonance Spectra. *The Journal of Chemical Physics* **26**, 217–218 (1957).

[15] Holm, C. Observation of Chemical Shielding and Spin Coupling of ^{13}C Nuclei in Various Chemical Compounds by Nuclear Magnetic Resonance. *The Journal of Chemical Physics* **26**, 707–708 (1957).

[16] Damadian, R., Zaner, K., Hor, D. & DiMaio, T. Human Tumors Detected by Nuclear Magnetic Resonance. *Proceedings of the National Academy of Sciences* **71**, 1471–1473 (1974).

[17] Damadian, R. Apparatus and Method for Detecting Cancer in Tissue (1974). US Patent 3,789,832.

[18] Lauterbur, P. C. Medical Imaging by Nuclear Magnetic Resonance Zeugmatography. *IEEE Transactions on Nuclear Science* **26**, 2807–2811 (1979).

[19] Aue, W., Bartholdi, E. & Ernst, R. R. Two-Dimensional Spectroscopy. Application to Nuclear Magnetic Resonance. *The Journal of Chemical Physics* **64**, 2229–2246 (1976).

[20] Damadian, R., Minkoff, L., Goldsmith, M., Stanford, M. & Koutcher, J. Field Focusing Nuclear Magnetic Resonance (FONAR): Visualization of a Tumor in a Live Animal. *Science* **194**, 1430–1432 (1976).

[21] Garroway, A. N., Grannell, P. K. & Mansfield, P. Image Formation in NMR by a Selective Irradiative Process. *Journal of Physics C: Solid State Physics* **7**, L457 (1974).

[22] Mansfield, P. Multi-Planar Image Formation using NMR Spin Echoes. *Journal of Physics C: Solid State Physics* **10**, L55 (1977).

[23] Levitt, M. H. *Spin Dynamics: Basics of Nuclear Magnetic Resonance* (John Wiley & Sons, 2001).

[24] Bryan, R. N. *Introduction to the Science of Medical Imaging* (Cambridge University Press, 2009).

[25] Gibson, R. *Essential Medical Imaging* (Cambridge University Press, 2009).

[26] Mansfield, P. & Maudsley, A. A. Medical Imaging by NMR. *The British journal of radiology* **50**, 188–194 (1977).

[27] Edelstein, W., Glover, G., Hardy, C. & Redington, R. The Intrinsic Signal-to-Noise Ratio in NMR Imaging. *Magnetic Resonance in medicine* **3**, 604–618 (1986).

[28] Kuhn, W. NMR Microscopy—Fundamentals, Limits and Possible Applications. *Angewandte Chemie International Edition in English* **29**, 1–19 (1990).

[29] Fukushima, E. & Roeder, S. B. *Experimental Pulse NMR: A Nuts and Bolts Approach* (Addison-Wesley Reading, MA, 1981).

[30] Goodson, B. M. Nuclear Magnetic Resonance of Laser-Polarized Noble Gases in Molecules, Materials, and Organisms. *Journal of Magnetic Resonance* **155**, 157–216 (2002).

[31] Ward, H. R. Chemically Induced Dynamic Nuclear Polarization (CIDNP). I. Phenomenon, Examples and Applications. *Accounts of Chemical Research* **5**, 18–24 (1972).

[32] Natterer, J. & Bargon, J. Parahydrogen Induced Polarization. *Progress in Nuclear Magnetic Resonance Spectroscopy* **31**, 293–315 (1997).

[33] Adams, R. W. *et al.* Reversible Interactions with Para-Hydrogen Enhance NMR Sensitivity by Polarization Transfer. *Science* **323**, 1708–1711 (2009).

[34] Owers-Bradley, J. R., Horsewill, A. J., Peat, D. T., Goh, K. S. & Gadian, D. G. High Polarization of Nuclear Spins Mediated by Nanoparticles at millikelvin Temperatures. *Physical Chemistry Chemical Physics* **15**, 10413–10417 (2013).

[35] Hirsch, M. L., Kalechofsky, N., Belzer, A., Rosay, M. & Kempf, J. G. Brute-Force Hyperpolarization for NMR and MRI. *Journal of the American Chemical Society* **137**, 8428–8434 (2015).

[36] Hirsch, M. L. *et al.* Transport and Imaging of Brute-Force ^{13}C Hyperpolarization. *Journal of Magnetic Resonance* **261**, 87–94 (2015).

[37] Gadian, D. G. *et al.* Preparation of Highly Polarized Nuclear Spin Systems using Brute-Force and Low-Field Thermal Mixing. *Physical Chemistry Chemical Physics* **14**, 5397–5402 (2012).

[38] Krjukov, E., O'Neill, J. & Owers-Bradley, J. Brute Force Polarization of ^{129}Xe. *Journal of low temperature physics* **140**, 397–408 (2005).

[39] Joo, C.-G., Hu, K.-N., Bryant, J. A. & Griffin, R. G. In Situ Temperature Jump High-Frequency Dynamic Nuclear Polarization

Experiments: Enhanced Sensitivity in Liquid-State NMR Spectroscopy. *Journal of the American Chemical Society* **128**, 9428–9432 (2006).

[40] Frydman, L. & Blazina, D. Ultrafast Two-Dimensional Nuclear Magnetic Resonance Spectroscopy of Hyperpolarized Solutions. *Nature Physics* **3**, 415–419 (2007).

[41] Krishna, M. C. *et al.* Overhauser Enhanced Magnetic Resonance Imaging for Tumor Oximetry: Coregistration of Tumor Anatomy and Tissue Oxygen Concentration. *Proceedings of the National Academy of Sciences* **99**, 2216–2221 (2002).

[42] Ardenkjær-Larsen, J. H. *et al.* Increase in Signal-to-Noise Ratio of $>$ 10,000 times in liquid-state NMR. *Proceedings of the National Academy of Sciences* **100**, 10158–10163 (2003).

[43] Leggett, J. *et al.* A Dedicated Spectrometer for Dissolution DNP NMR Spectroscopy. *Physical Chemistry Chemical Physics* **12**, 5883–5892 (2010).

[44] Ardenkjaer-Larsen, J. H. On the Present and Future of Dissolution-DNP. *Journal of Magnetic Resonance* **264**, 3–12 (2016).

[45] Granwehr, J., Leggett, J. & Köckenberger, W. A Low-Cost Implementation of EPR Detection in a Dissolution DNP Setup. *Journal of Magnetic Resonance* **187**, 266–276 (2007).

[46] Comment, A. *et al.* Producing over 100ml of Highly Concentrated Hyperpolarized Solution by means of Dissolution DNP. *Journal of Magnetic Resonance* **194**, 152–155 (2008).

[47] Jähnig, F., Kwiatkowski, G. & Ernst, M. Conceptual and Instrumental Progress in Dissolution DNP. *Journal of Magnetic Resonance* **264**, 22–29 (2016).

[48] Bowen, S. & Hilty, C. Rapid Sample Injection for Hyperpolarized NMR Spectroscopy. *Physical Chemistry Chemical Physics* **12**, 5766–5770 (2010).

[49] Frydman, L., Scherf, T. & Lupulescu, A. The Acquisition of Multidimensional NMR Spectra Within a Single Scan. *Proceedings of the National Academy of Sciences* **99**, 15858–15862 (2002).

[50] Krummenacker, J. G., Denysenkov, V. P., Terekhov, M., Schreiber, L. M. & Prisner, T. F. DNP in MRI: An In-Bore Approach at 1.5 T. *Journal of Magnetic Resonance* **215**, 94–99 (2012).

[51] Comment, A. Dissolution DNP for in vivo Preclinical Studies. *Journal of Magnetic Resonance* **264**, 39–48 (2016).

[52] Harris, T., Bretschneider, C. & Frydman, L. Dissolution DNP NMR with Solvent Mixtures: Substrate Concentration and Radical Extraction. *Journal of Magnetic Resonance* **211**, 96–100 (2011).

[53] Gallagher, F., Kettunen, M. & KM, B. Biomedical Applications of Hyperpolarized ^{13}C Magnetic Resonance Imaging. *Progress in Nuclear Magnetic Resonance Spectroscopy* **55**, 285–295 (2009).

[54] Brindle, K. M., Bohndiek, S. E., Gallagher, F. A. & Kettunen, M. I. Tumor Imaging using Hyperpolarized ^{13}C Magnetic Resonance Spectroscopy. *Magnetic Resonance in Medicine* **66**, 505–519 (2011).

[55] Münnemann, K. *et al.* A Mobile DNP Polarizer for Clinical Applications. *Applied Magnetic Resonance* **34**, 321–330 (2008).

[56] Ardenkjaer-Larsen, J. H. *et al.* Dynamic Nuclear Polarization Polarizer for Sterile use Intent. *NMR in biomedicine* **24**, 927–932 (2011).

[57] Hu, S. *et al.* Rapid Sequential Injections of Hyperpolarized [1-^{13}C] Pyruvate *in vivo* using a Sub-Kelvin, Multi-Sample DNP Polarizer. *Magnetic resonance imaging* **31**, 490–496 (2013).

[58] Mishkovsky, M. & Comment, A. Hyperpolarized MRS: New Tool to Study Real-Time Brain Function and Metabolism. *Analytical biochemistry* **529**, 270–277 (2017).

[59] Yoshihara, H. A. *et al.* High-Field Dissolution Dynamic Nuclear Polarization of [1-^{13}C] Pyruvic Acid. *Physical Chemistry Chemical Physics* **18**, 12409–12413 (2016).

[60] Nelson, S. J. *et al.* Metabolic Imaging of Patients with Prostate Cancer using Hyperpolarized [1-^{13}C] Pyruvate. *Science translational medicine* **5**, 198ra108–198ra108 (2013).

[61] Joo, C.-G., Casey, A., Turner, C. J. & Griffin, R. G. In Situ Temperature-Jump Dynamic Nuclear Polarization: Enhanced Sensitivity in Two Dimensional ^{13}C-^{13}C Correlation Spectroscopy in Solution. *Journal of the American Chemical Society* **131**, 12–13 (2008).

[62] Yoon, D. *et al.* Dynamic Nuclear Polarization by Frequency Modulation of a Tunable Gyrotron of 260 GHz. *Journal of Magnetic Resonance* **262**, 62–67 (2016).

[63] Yoon, D. *et al.* 500-Fold Enhancement of in situ ^{13}C Liquid State NMR using Gyrotron-Driven Temperature-Jump DNP. *Journal of Magnetic Resonance* **270**, 142–146 (2016).

[64] Sharma, M., Janssen, G., Leggett, J., Kentgens, A. & van Bentum, P. Rapid-Melt Dynamic Nuclear Polarization. *Journal of Magnetic Resonance* **258**, 40–48 (2015).

[65] van Bentum, P., Sharma, M., van Meerten, S. & Kentgens, A. Solid Effect DNP in a Rapid-Melt Stup. *Journal of Magnetic Resonance* **263**, 126–135 (2016).

[66] van Bentum, J., van Meerten, B., Sharma, M. & Kentgens, A. Perspectives on DNP-Enhanced NMR Spectroscopy in Solutions. *Journal of Magnetic Resonance* **264**, 59–67 (2016).

[67] Neuhaus, D. Nuclear Overhauser Effect. *eMagRes* (2000).

[68] Rosay, M., Weis, V., Kreischer, K. E., Temkin, R. J. & Griffin, R. G. Two-Dimensional $^{13}C-^{13}C$ Correlation Spectroscopy with Magic Angle Spinning and Dynamic Nuclear Polarization. *Journal of the American Chemical Society* **124**, 3214–3215 (2002).

[69] McDermott, A. Structure and Dynamics of Membrane Proteins by Magic Angle Spinning Solid-State NMR. *Annual Review of Biophysics* **38**, 385–403 (2009).

[70] McDermott, A. E. & Polenova, T. *Solid State NMR Studies of Biopolymers* (John Wiley & Sons, 2012).

[71] Bloembergen, N., Purcell, E. M. & Pound, R. V. Relaxation Effects in Nuclear Magnetic Resonance Absorption. *Phys. Rev.* **73**, 679–712 (1948).

[72] Can, T. *et al.* Overhauser Effects in Insulating Solids. *The Journal of Chemical Physics* **141**, 064202 (2014).

[73] Abragam, A. & Goldman, M. Principles of Dynamic Nuclear Polarisation. *Reports on Progress in Physics* **41**, 395 (1978).

[74] Hovav, Y., Feintuch, A. & Vega, S. Theoretical Aspects of Dynamic Nuclear Polarization in the Solid State - The Solid Effect. *Journal of Magnetic Resonance* **207**, 176–189 (2010).

[75] Wenckebach, W. T. The Solid Effect. *Applied Magnetic Resonance* **34**, 227–235 (2008).

[76] Hu, K.-N., Yu, H.-h., Swager, T. M. & Griffin, R. G. Dynamic Nuclear Polarization with Biradicals. *Journal of the American Chemical Society* **126**, 10844–10845 (2004).

[77] Hovav, Y., Feintuch, A. & Vega, S. Theoretical Aspects of Dynamic Nuclear Polarization in the Solid State - The Cross Effect. *Journal of Magnetic Resonance* **214**, 29–41 (2012).

[78] Goldman, M. Overview of Spin Temperature, Thermal Mixing and Dynamic Nuclear Polarization. *Applied Magnetic Resonance* **34**, 219–226 (2008).

[79] Hovav, Y., Feintuch, A. & Vega, S. Theoretical Aspects of Dynamic Nuclear Polarization in the Solid State - Spin Temperature and Thermal Mixing. *Physical Chemistry Chemical Physics* **15**, 188–203 (2013).

[80] Maly, T. *et al.* Dynamic Nuclear Polarization at High Magnetic Fields. *The Journal of chemical physics* **128**, 052211 (2008).

[81] Thankamony, A. S. L., Wittmann, J. J., Kaushik, M. & Corzilius, B. Dynamic Nuclear Polarization for Sensitivity Enhancement in Modern Solid-State NMR. *Progress in Nuclear Magnetic Resonance Spectroscopy* **102**, 120–195 (2017).

[82] Kubicki, D. J. *et al.* Rational Design of Dinitroxide Biradicals for Efficient Cross-Effect Dynamic Nuclear Polarization. *Chemical Science* **7**, 550–558 (2016).

[83] Lumata, L. *et al.* Electron Spin Resonance Studies of Trityl OX063 at a Concentration Optimal for DNP. *Physical Chemistry Chemical Physics* **15**, 9800–9807 (2013).

[84] Ysacco, C. *et al.* Properties of Dinitroxides for use in Dynamic Nuclear Polarization (DNP). *Physical Chemistry Chemical Physics* **12**, 5841–5845 (2010).

[85] Hu, K.-N., Bajaj, V. S., Rosay, M. & Griffin, R. G. High-Frequency Dynamic Nuclear Polarization using Mixtures of TEMPO and Trityl Radicals. *The Journal of chemical physics* **126**, 044512 (2007).

[86] Michaelis, V. K. *et al.* High-Field ^{13}C Dynamic Nuclear Polarization with a Radical Mixture. *Journal of the American Chemical Society* **135**, 2935–2938 (2013).

[87] Song, C., Hu, K.-N., Joo, C.-G., Swager, T. M. & Griffin, R. G. TOTAPOL: a Biradical Polarizing Agent for Dynamic Nuclear Polarization Experiments in Aqueous Media. *Journal of the American Chemical Society* **128**, 11385–11390 (2006).

[88] Lumata, L., Kovacs, Z., Malloy, C., Sherry, A. D. & Merritt, M. The Effect of ^{13}C Enrichment in the Glassing Matrix on Dynamic Nuclear Polarization of [1-^{13}C] Pyruvate. *Physics in Medicine and Biology* **56**, N85 (2011).

[89] Magazù, S., Migliardo, F. & Telling, M. Dynamics of Glass-Forming Bioprotectant Systems. *Journal of Non-Crystalline Solids* **357**, 691–694 (2011).

[90] Perras, F. A., Reinig, R. R., Slowing, I. I., Sadow, A. D. & Pruski, M. Effects of Biradical Deuteration on the Performance of DNP: Towards Better Performing Polarizing Agents. *Physical Chemistry Chemical Physics* **18**, 65–69 (2016).

[91] Gajan, D. *et al.* Hybrid Polarizing Solids for Pure Hyperpolarized Liquids through Dissolution Dynamic Nuclear Polarization. *Proceedings of the National Academy of Sciences* **111**, 14693–14697 (2014).

[92] Nanni, E. A., Barnes, A. B., Griffin, R. G. & Temkin, R. J. THz Dynamic Nuclear Polarization NMR. *IEEE transactions on terahertz science and technology* **1**, 145–163 (2011).

[93] Earle, K. & Freed, J. Quasioptical Hardware for a Flexible FIR-EPR Spectrometer. *Applied Magnetic Resonance* **16**, 247–272 (1999).

[94] Lax, B., Weiss, J. A., Harris, N. W. & Diomne, G. Quasi-Optical Ferrite Reflection Circulator. *IEEE Transactions on Microwave Theory and Techniques* **41**, 2190–2197 (1993).

[95] Vinoy, K. & Jha, R. Trends in Radar Absorbing Materials Technology. *Sadhana* **20**, 815–850 (1995).

[96] Smith, G., Lesurf, J., Mitchell, R. & Riedi, P. Quasi-Optical CW mm-Wave Electron Spin Resonance Spectrometer. *Review of scientific instruments* **69**, 3924–3937 (1998).

[97] Mrózek, M., Mlynarczyk, J., Rudnicki, D. S. & Gawlik, W. Circularly Polarized Microwaves for Magnetic Resonance Study in the GHz range: Application to Nitrogen-Vacancy in Diamonds. *Applied Physics Letters* **107**, 013505 (2015).

[98] Martin, D. & Puplett, E. Polarized Interferometric Spectrometry for the Millimeter and Submillimeter Spectrum. *Infrared Physics* **10**, 105–109 (1970).

[99] Lambert, D. & Richards, P. Martin-Puplett Interferometer: An Analysis. *Applied Optics* **17**, 1595–1602 (1978).

[100] Lide, D. R. *CRC Handbook of Chemistry and Physics*, vol. 85 (CRC press, 2004).

[101] Kent, T. *Experimental Low Temperature Physics* (Springer Science & Business Media, 1992).

[102] Maytal, B.-Z. & Pfotenhauer, J. M. *Miniature Joule-Thompson Cryocooling: Principles and Practice* (Springer Science & Business Media, 2012).

[103] Hohenberg, P. & Martin, P. Microscopic Theory of Superfluid Helium. *Annals of Physics* **34**, 291–359 (1965).

[104] Zettili, N. *Quantum Mechanics: Concepts and Applications* (John Wiley & Sons, 2009).

[105] Anderson, P. W. Considerations on the Flow of Superfluid Helium. *Review of Modern Physics* **38**, 298 (1966).

[106] Kim, C. S. Thermophysical Properties of Stainless Steels. Tech. Rep., Argonne National Lab., Ill.(USA) (1975).

[107] Smallman, R. E. & Bishop, R. J. *Modern Physical Metallurgy and Materials Engineering* (Butterworth-Heinemann, 1999).

[108] Higgins, R. A. *Materials for Engineers and Technicians* (Routledge, 2010).

[109] White, G. K. Experimental Techniques in Low-Temperature Physics (1987).

[110] Sauer, J. & Kline, D. Dynamic Mechanical Properties of Polystyrene, Polyethylene and Polytetrafluoroethylene at Low Temperatures. *Journal of Polymer Science* **18**, 491–495 (1955).

[111] Bejan, A. & Kraus, A. D. *Heat Transfer Handbook*, vol. 1 (John Wiley & Sons, 2003).

[112] Bejan, A. *Convection Heat Transfer* (John Wiley & Sons, 2013).

[113] Davis, J. R. & Others. *Stainless Steels* (ASM International, 1994).

[114] Maris, H. *Phonon Scattering in Condensed Matter* (Springer Science & Business Media, 2012).

[115] Dobrovinskaya, E. R., Lytvynov, L. A. & Pishchik, V. Properties of Sapphire. In *Sapphire*, 55–176 (Springer, 2009).

[116] Bowley, R. & Sanchez, M. *Introductory Statistical Mechanics* (Clarendon Press Oxford, 1999).

[117] Roth, A. *Vacuum Technology* (Elsevier, 2012).

[118] O'Hanlon, J. F. *A User's Guide to Vacuum Technology* (John Wiley & Sons, 2005).

[119] Pfeiffer. *The Vacuum Technology Book* (Pfeiffer Vacuum, 2008).

[120] Umrath, W. *Fundamentals of Vacuum Technology* (Oerlikon Leybold Vacuum, 2007).

[121] Morgan, G. & Jensen, J. Counter-Flow Cooling of a Transmission Line by Supercritical Helium. *Cryogenics* **17**, 259–267 (1977).

[122] Woskov, P. P., Bajaj, V. S., Hornstein, M. K., Temkin, R. J. & Griffin, R. G. Corrugated Waveguide and Directional Coupler for CW 250-GHz Gyrotron DNP Experiments. *IEEE transactions on microwave theory and techniques* **53**, 1863–1869 (2005).

[123] Plaum, B., Holzhauer, E., Grünert, M. & Kumric, H. Optimum Corrugations for Low-Loss Square and Cylindrical Waveguides. In *Proceedings of the Digest of the 4th IAEA workshop on ECRH for ITER, Vienna, Austria* (2007).

[124] Clarricoats, P. & Olver, A. Low Attenuation in Corrugated Circular Waveguides. *Electronics Letters* **16**, 376–377 (1973).

[125] Kowalski, E. J. *et al.* Linearly Polarized Modes of a Corrugated Metallic Waveguide. *IEEE Transactions on Microwave Theory and Techniques* **58**, 2772–2780 (2010).

[126] Afsar, M. Dielectric Measurements of Common Polymers at Millimeter Wavelength. In *Microwave Symposium Digest, 1985 IEEE MTT-S International*, 439–442 (IEEE, 1985).

[127] Wunderlich, B. Study of the Change in Specific Heat of Monomeric and Polymeric Glasses during the Glass Transition. *The Journal of Physical Chemistry* **64**, 1052–1056 (1960).

[128] Marcus, Y. Some Thermodynamic and Structural Aspects of Mixtures of Glycerol with Water. *Physical Chemistry Chemical Physics* **2**, 4891–4896 (2000).

[129] Tan, I., Wee, C. C., Sopade, P. A. & Halley, P. J. Estimating the Specific Heat Capacity of Starch-Water-Glycerol Systems as a function of Temperature and Compositions. *Starch-Stärke* **56**, 6–12 (2004).

[130] Birge, N. O. Specific-Heat Spectroscopy of Glycerol and Propylene Glycol near the Glass Transition. *Physical Review B* **34**, 1631 (1986).

[131] Grigoropoulos, C. P. *Transport in Laser Microfabrication: Fundamentals and Applications* (Cambridge University Press, 2009).

[132] Townes, C. H. & Schawlow, A. L. *Microwave Spectroscopy* (Courier Corporation, 2013).

[133] Harrison, J. Cryostat for the Measurement of Thermal Conductivity and Specific Heat between 0.05 and 2 K. *Review of Scientific Instruments* **39**, 145–152 (1968).

[134] Willets, K. A. & Van Duyne, R. P. Localized Surface Plasmon Resonance Spectroscopy and Sensing. *Annu. Rev. Phys. Chem.* **58**, 267–297 (2007).

[135] Zeng, S. *et al.* A Review on Functionalized Gold Nanoparticles for Biosensing Applications. *Plasmonics* **6**, 491–506 (2011).

[136] Petryayeva, E. & Krull, U. J. Localized Surface Plasmon Resonance: Nanostructures, Bioassays and Biosensing — A Review. *Analytica chimica acta* **706**, 8–24 (2011).

[137] Khlebtsov, N. G. & Dykman, L. A. Optical Properties and Biomedical Applications of Plasmonic Nanoparticles. *Journal of Quantitative Spectroscopy and Radiative Transfer* **111**, 1–35 (2010).

[138] Richardson, H. H., Carlson, M. T., Tandler, P. J., Hernandez, P. & Govorov, A. O. Experimental and Theoretical Studies of Light-to-Heat Conversion and Collective Heating Effects in Metal Nanoparticle Solutions. *Nano letters* **9**, 1139–1146 (2009).

[139] Govorov, A. O. *et al.* Gold Nanoparticle Ensembles as Heaters and Actuators: Melting and Collective Plasmon Resonances. *Nanoscale Research Letters* **1**, 84–90 (2006).

[140] Callaghan, P. T. *Principles of Nuclear Magnetic Resonance Microscopy* (Oxford University Press on Demand, 1993).

[141] Etchegoin, P. G., Le Ru, E. & Meyer, M. An Analytic Model for the Optical Properties of Gold. *The Journal of chemical physics* **125**, 164705 (2006).

[142] Allmen, M. v. & Blatter, A. *Laser-Beam Interactions with Materials: Physical Principles and Applications*, vol. 2 (Springer Science & Business Media, 2013).

[143] Stuart, B. *Infrared Spectroscopy* (Wiley Online Library, 2005).

[144] Breschi, B. *et al.* Measurement of Water Column Temperature by Raman Scattering. *EARSeL Advances in Remote Sensing* **1**, 131 (1992).

[145] Zelent, B., Nucci, N. V. & Vanderkooi, J. M. Liquid and Ice Water and Glycerol/Water Glasses Compared by Infrared Spectroscopy from 295 to 12 K. *The Journal of Physical Chemistry A* **108**, 11141–11150 (2004).

[146] Dashnau, J. L., Nucci, N. V., Sharp, K. A. & Vanderkooi, J. M. Hydrogen Bonding and the Cryoprotective Properties of Glycerol/Water Mixtures. *The Journal of Physical Chemistry B* **110**, 13670–13677 (2006).

[147] Lucas, J. Fluoride Glasses for Modern Optics. *Journal of fluorine chemistry* **72**, 177–181 (1995).

[148] Kotsifaki, D. & Serafetinides, A. Mid-Infrared Radiation Transmission through Fluoride Glass Multimode Optical Fibers. *Optics & Laser Technology* **43**, 1448–1452 (2011).

[149] Verdaasdonk, R. M. & van Swol, C. F. Laser Light Delivery Systems for Medical Applications. *Physics in medicine and biology* **42**, 869 (1997).

[150] Harrington, J. A. Infrared Fibers and their Applications (SPIE-International Society for Optical Engineering, 2003).

[151] Wayant, R. W., Ilev, I. K. & Gannot, I. Mid-Infrared Laser Applications in Medicine and Biology. *Philosophical Transactions of the Royal Society of London A: Mathematical, Physical and Engineering Sciences* **359**, 635–644 (2001).

[152] Davis, C. C. *Lasers and Electro-Optics: Fundamentals and Engineering* (Cambridge University Press, 2014).

[153] Jundt, D., Fejer, M. & Bye, R. Characterization of Single-Crystal Sapphire Fibres for Optical Power Delivery Systems. *Applied Physics Letters* **55**, 2170–2172 (1989).

[154] Abel, T., Hirsch, J. & Harrington, J. A. Hollow Glass Waveguides for Broadband Infrared Transmission. *Optics letters* **19**, 1034–1036 (1994).

[155] Kato, Y. & Miyagi, M. Modes and Attenuation Constants in Circular Hollow Waveguides with Small Core Diameters for the Infrared. *IEEE transactions on microwave theory and techniques* **40**, 679–685 (1992).

[156] Harrington, J. A. Co-Axial Hollow Core Waveguide (1998). US Patent 5,815,627.

[157] George, R. & Harrington, J. A. Infrared Transmissive, Hollow Plastic Waveguides with Inner Ag-AgI Coatings. *Applied optics* **44**, 6449–6455 (2005).

[158] Harrington, J. A. A Review of IR Transmitting, Hollow Waveguides. *Fiber & Integrated Optics* **19**, 211–227 (2000).

[159] Smith, E. & Dent, G. *Modern Raman Spectroscopy: A Practical Approach* (John Wiley & Sons, 2013).

[160] Bernath, P. F. *Spectra of Atoms and Molecules* (Oxford University Press, 2015).

[161] Nikitin, S., Manka, C., Grun, J. & Bowles, J. A Technique for Contactless Measurement of Water Temperature using Stokes and anti-Stokes Comparative Raman Spectroscopy. *Review of Scientific Instruments* **83**, 033105 (2012).

[162] Laserna, J. J. Modern Techniques in Raman Spectroscopy (1996).

[163] Zinn, S. & Semiatin, S. Coil Design and Fabrication: Basic Design and Modifications. *Heat Treating* **12**, 32–36 (1988).

[164] Ginsberg, D. & Melchner, M. J. Optimum Geometry of Saddle Shaped Coild for Generating a Uniform Magnetic Field. *Review of Scientific Instruments* **41**, 122–123 (1970).

[165] Zens, A. P. NMR Probe Coil System (1983). US Patent 4,398,149.

[166] Massin, C. *et al.* High-Q factor RF planar microcoils for micro-scale NMR spectroscopy. *Sensors and Actuators A: Physical* **97**, 280–288 (2002).

[167] Bendall, M. R. & Gordon, R. E. Depth and refocusing pulses designed for multipulse NMR with surface coils. *Journal of Magnetic Resonance (1969)* **53**, 365–385 (1983).

[168] Styles, P. *et al.* A High-Resolution NMR Probe in which the Coil and Preamplifier are Cooled with Liquid Helium. *Journal of Magnetic Resonance (1969)* **60**, 397–404 (1984).

[169] Pease, J. *et al.* 40th Experimental Nuclear Magnetic Resonance Conference, Orlando, FL, February 28-March 5, 1999. *Abstracts W&Th P* **202**.

[170] Hajduk, P. J. *et al.* High-Throughput Nuclear Magnetic Resonance-Based Screening. *Journal of Medicinal Chemistry* **42**, 2315–2317 (1999).

[171] Serber, Z. *et al.* New Carbon-Detected Protein NMR Experiments using CryoProbes. *Journal of the American Chemical Society* **122**, 3554–3555 (2000).

[172] Setoura, K., Werner, D. & Hashimoto, S. Optical Scattering Spectral Thermometry and Refractometry of a Single Gold Nanoparticle under CW Laser Excitation. *The Journal of Physical Chemistry C* **116**, 15458–15466 (2012).

[173] Ishihara, Y. *et al.* A Precise and Fast Temperature Mapping using Water Proton Chemical Shift. *Magnetic Resonance in Medicine* **34**, 814–823 (1995).